

**ALMA MATER STUDIORUM - UNIVERSITÀ DI BOLOGNA**  
**CONSEIL EUROPÉEN POUR LA RECHERCHE NUCLÉAIRE - CERN (CH)**

---

**SCUOLA DI INGEGNERIA E ARCHITETTURA**

*DIPARTIMENTO DI INGEGNERIA DELL'ENERGIA ELETTRICA E DELL'INFORMAZIONE*  
*"GUGLIELMO MARCONI" - DEI*

*CORSO DI LAUREA MAGISTRALE IN INGEGNERIA ENERGETICA*

**MASTER THESIS**

in

Engineering of Superconducting Systems

*Analysis of impregnated Niobium-Tin coils for the*  
*High-Luminosity LHC magnets*

*Candidate:*  
Giovanni Succi

Coordinator:  
Prof. Ing. Marco Breschi

Advisors:  
Dr. Arnaud Devred  
Dr. Luca Bottura  
Prof. Ing. Sandro Manservigi  
Ing. Enrico Felcini

Anno Accademico [2017/18]

Sessione III



A Graziella Sarti  
e  
A mia nonna



“Success is not final, Failure is not fatal: it is the courage to continue that counts”  
Sir Winston S. Churchill



## Sommario

Il progetto ad alta luminosità dell'LHC prevede l'utilizzo di una nuova tecnologia di magneti superconduttivi, che faranno affidamento su un materiale mai utilizzato in precedenza, il Nb<sub>3</sub>Sn. Alcuni magneti dipolari verranno sostituiti all'interno dell'acceleratore per migliorare il sistema di collimazione dei fasci e saranno in grado di produrre campi magnetici nell'ordine dei 12 T, contro gli 8 T della macchina attuale.

La fragilità del Nb<sub>3</sub>Sn richiede una fase di impregnazione con resina epossidica durante il processo produttivo degli avvolgimenti, per evitare che si verifichi lo spostamento relativo dei fili causato dalle forze di Lorentz, che provocherebbe uno sforzo eccessivo su di essi, degradandone le proprietà superconduttive. Allo stesso tempo, l'impregnazione impedisce all'elio superfluido, il liquido refrigerante, di filtrare all'interno degli avvolgimenti, causando una sostanziale differenza nel comportamento termico delle bobine rispetto a quelle realizzate in Nb-Ti.

Alcune prove sperimentali sono state condotte presso il laboratorio di criogenia del CERN per studiare il comportamento termico di un campione del dipolo dell'11 T sottoposto a perdite AC, con valori tipici di densità di potenza nell'ordine del  $mW/cm^3$ . Il campione veniva inserito all'interno di un contenitore isolante, in cui solamente la superficie dello strato interno di conduttori rimaneva esposta all'ambiente esterno. Il tutto veniva poi immerso in elio superfluido, per rappresentare al meglio la situazione reale.

Questa tesi, che è stata svolta presso il gruppo MSC (Magnets, Superconductors and Cryostats) del CERN, è incentrata sullo sviluppo di un modello 1-D di una linea radiale giacente sul piano di mezzeria di un quadrante del magnete. Esso è anche rappresentativo dei materiali della sezione ed è stato utilizzato allo scopo di studiare l'evoluzione di temperatura e i profili stazionari in risposta a introduzioni di calore nei conduttori, simili a quelle dell'esperimento citato.

Lo stesso modello è stato poi adattato al caso di prove di quench eseguite presso la SM-18 facility su modelli corti del dipolo dell'11 T. In tali test, riscaldatori induttivi venivano energizzati per rilasciare calore nel magnete, in modo che il quench venisse innescato a partire da certe condizioni operative di corrente e campo.

Partendo dalle mappe di campo e dalla parametrizzazione per il materiale superconduttivo, è stato possibile ricavare i valori di  $T_{cs}$ , usando di fatto il magnete come un sensore di temperatura.

Il lavoro presenta una descrizione dettagliata del modello e delle ipotesi fatte per condurre le simulazioni, insieme ad una sua validazione tramite il confronto con le suddette prove sperimentali.

## Abstract

The High-luminosity project of the LHC calls for the employment of a new technology of superconducting magnets, which will make use of a material never used before, Nb<sub>3</sub>Sn. Some of the dipole magnets will be replaced inside the accelerator to enhance the collimating system of the beams and will be capable of producing magnetic fields in the order of 12 T, against the 8 T of the present machine.

The fragility of Nb<sub>3</sub>Sn requires an impregnation stage with epoxy resin during coil manufacturing, to avoid that relative movement between strands takes place due to Lorentz forces, which would be the source of excessive stress on strands themselves, degrading their superconducting properties.

At the same time, the impregnation prevents superfluid helium, the liquid coolant, from filtering inside the coils, thus causing a substantial difference in the thermal behavior with respect to Nb-Ti.

Experimental tests were conducted at the cryogenic laboratory at CERN to study the thermal behavior of a sample of the 11 T dipole under AC losses, with typical values of the input power density in the order of the  $mW/cm^3$ . The sample was inserted into an open box of insulator, with the surface corresponding to the inner layer of conductors being the only one exposed to the exterior, and was then immersed in superfluid helium, to get closer to real operation.

This thesis, which was carried out at the MSC (Magnets, Superconductors and Cryostats) Group at CERN, regards the development of a 1-D model of a radial line crossing the middle plane of a quadrant of the magnet. It is also representative of the materials in the section and it was used with the aim to study the temperature evolution and steady-state profiles in response to heat injections in the conductors, similar to those provided in the experiment.

The same model was adapted to reproduce results of quench tests carried out at the SM-18 facility on short models of the 11 T dipole. In such tests, inductive heaters were energized to release heat in the magnet, in order to trigger the quench phenomenon, starting from given operating conditions of current and field. Using magnetic field maps together with the parametrization of the superconducting material, it was possible to derive local values of the  $T_{CS}$ , thus employing the magnet as a temperature probe.

This work presents a detailed description of the model and of the hypothesis made to run the simulations, together with its validation obtained through the comparison with experimental tests cited above.

## Introduction

The mission of CERN (European Council for Nuclear Research) is aimed at fundamental research, with a special focus on particle physics. Here, between the years 2001 and 2008 the biggest and most powerful particle accelerator in the world, the Large Hadron Collider (LHC), was built. This accelerator is capable of colliding hadron beams (protons or lead ions) at an energy never reached before, namely 14 TeV in the center of mass, which enables to study the moments immediately following the Big Bang.

The employment of this machine and of its four big detectors has brought, at the present day, to important achievements, as the discovery of the Higgs boson and the demonstration of the existence of penta-quarks. Despite accomplishments in particle physics are of major relevance for the outside world, it is important to consider that a machine so complex as the LHC requires considerable efforts from an engineering point of view. Many systems are involved to obtain proper operation of the machine, from superconducting magnets to cryogenics, from radiofrequency cavities up to kicker magnets, used for injection and extraction of the beams from the machine. Furthermore, the LHC is only the final stage of an entire complex of accelerators, some of them dating back to the establishment of the center.

An upgrading project of the machine, called High-Luminosity LHC, is planned to be completed by the year 2025, which will bring the luminosity, a key parameter for particle physics, a factor ten higher with respect to the present value. This will enable to gather much more data on particle collisions, increasing the potential of discovery of new fundamental phenomena. The fulfillment of such project requires the substitution of some dipoles and of 16 quadrupoles inside the machine, with new versions that will make use of Nb<sub>3</sub>Sn coils, a superconducting material never used before to build accelerator magnets, which will enable to increase magnetic fields to 12 T, a considerable advance with respect to the 8 T provided by the present material, Nb-Ti.

Nb<sub>3</sub>Sn requires a special process of fabrication, at the end of which a very fragile composite is obtained, due to the crystalline structure which characterizes this intermetallic compound. Coils are then impregnated using epoxy resin in a way that displacements between adjacent strands are blocked, thus avoiding excessive degradation by mechanical stresses. Determining the thermal behavior of this new technology of magnets is fundamental for their future employment in the machine, since they are significantly different from the past.

The aim of this work is to present a thermal study on the dipole magnet for the High-luminosity project (also named “11 T”), where a 1-D model was developed in order to reproduce the features of the magnet under examination. The HEATER software was used for this purpose [40]. This is able to solve the heat conduction equation in complex geometries and under the application of external sources, initial and boundary conditions. The complexity of the model was gradually increased to finally reproduce the proper geometry and material composition along a line radially crossing the middle plane of a quadrant of the magnet.

The model was used to reconstruct the temperature profile inside the magnet, both in transient and steady-state regime, in response to heat depositions in conductor layers. Such depositions were modeled as provided from the experiments carried out both at the cryogenic laboratory (Cryolab) [37] and at the SM-18 facility at CERN. Comparison with measurement results is reported.

The work opens with an introductory chapter about CERN and its purposes, where an explanation of the operation principles of accelerators is given. The accelerator complex which brings to the final stage, namely the LHC, is shown, and an outline of the features of the high-luminosity project is also displayed. A second chapter offers an overview on superconductivity, with a special focus on the technologies involved in magnets production.

The third chapter is dedicated to a presentation of the state-of-the-art concerning the mechanisms of heat exchange between the liquid coolant, helium, and superconducting cables made of Nb-Ti. The study begins from a first article [7] and then extends to a bibliographic research about heat exchange problems in a more general sense.

The main chapters present the activity which saw me involved at CERN, and which concerns subjects linked to heat exchange. The Cryolab experiment is firstly illustrated, to then pass at the 1-D simulation in HEATER. Care is adopted for the description of the approach to the problem, with a special focus in explaining all the details of the model, as the choice of the mesh, initial conditions and boundary conditions, as well. Discussion

of the results is very important for the purpose of this text, since the first simulations were significantly different from experimental ones. Consequently, a serious process of revision was undertaken, making assumptions that let us obtain a much better match with the measurements. These assumptions regard the role played by materials in the system from a thermal perspective and will be adequately justified.

The same model was then used to simulate quench tests carried out on short samples of the 11 T dipole. Quench is a major problem for superconducting magnet operation, since it is linked to the stability of magnets themselves. This phenomenon is typically produced by localized heat releases, which cause the transition of a small portion of material to the normal state, with the subsequent propagation to the entire magnet by Joule effect. Inductive heaters, called quench heaters, are normally instrumented on the external radius of the magnets, to ensure a uniform heating in the case a quench is detected, and to avoid excessive extra-heating in localized points. Two kinds of tests were conducted using quench heaters. In some of them, heaters were placed as in real operation, like the one already described. In others, they were inserted in the space between the two conductor layers, substituting the interlayer. Heat deposition in the magnet caused a temperature rise in both cases, with the following trigger of a quench. An interesting aspect is that the knowledge of operating conditions of the magnet and of the critical curve makes, to a certain extent, the magnet as a temperature probe.

The 1-D model was adapted to the respective geometries cited above, to understand if it was able to reproduce, firstly, quench detection in the same blocks identified in the measurements and, secondly, in the inner layer of the coil, which sees the higher values of magnetic fields. We started from field maps computed using the ROXIE software, to derive the field profiles on radial lines considered the most critical ones. Next, the Nb<sub>3</sub>Sn parametrization for ITER [38] was used, conveniently modified for the cables of the 11 T dipole, and to derive the current sharing temperature profiles,  $T_{CS}$ , along the same lines. The criterion defined to determine quench initiation was the overtaking of the temperature profile coming from the simulation with respect to the one coming from the  $T_{CS}$ , as in the computations above. A comparison with experimental results is presented, together with their interpretation.

In parallel with these two main studies, another one was performed, which is reported in Appendix I, aiming at determining the effective thermal conductivity of impregnated Rutherford cables made of Nb<sub>3</sub>Sn. Computations were made along all the three dimensions of the cable, and it was shown how the strand twisting plays a significant role in rising the conductivity along the major direction of the cable cross-section. In fact, strands behave as tubes for heat transmission, being made of more than 50% of copper. In this last case, results were compared again with experimental measurements on coil samples [34], performed along the radial and azimuthal direction of the coils. Explanation for discrepancies between analytical computations and experimental results is given.

# Contents

<b>1. CERN and the Large Hadron Collider</b>	<b>1</b>
1.1 CERN and its aim.....	1
1.2 The synchro-cyclotron and accelerators operation.....	1
1.3 The CERN accelerator complex.....	2
1.4 The High luminosity LHC.....	4
<b>2. Superconductivity</b>	<b>6</b>
2.1 Introduction and historical background.....	6
2.2 Perfect diamagnetism (Meissner effect).....	8
2.3 Critical parameters of superconductors.....	10
2.4 Type I superconductors.....	11
2.5 Type II superconductors.....	11
2.6 Theories of superconductivity.....	12
2.7 High Temperature Superconductors (HTS).....	13
2.8 Technologies for superconducting materials.....	15
2.8.1 Niobium-Titanium.....	15
2.8.2 Niobium-Tin.....	15
2.8.3 Fabrication methodologies of Nb <sub>3</sub> Sn strands.....	16
2.8.4 Cables and coils for accelerator magnets.....	17
2.9 Comparison with Nb-Ti cables.....	19
<b>3. Heat exchange properties of Helium in Nb-Ti superconducting cables</b>	<b>21</b>
3.1 Heat loads during machine operation.....	21
3.2 The quench phenomenon.....	21
3.3 Introduction to the model.....	22
3.4. Heat transfer to helium.....	24
3.4.1 $h_K$ (Kapitza).....	24
3.4.2 $h_{BL}$ (Boundary layer).....	25
3.4.3 $h_{SS}$ (Steady-state).....	26
3.4.4 $h_{HeI}$ (Helium I).....	28
3.4.5 $h_{nucl.boil.}$ (Nucleate boiling).....	29
3.4.6 $h_{film\ boil.}$ (Film boiling).....	31
3.4.7 $h_{HeI}$ (Gaseous helium).....	32
<b>4. The Cryolab experiment</b>	<b>33</b>
4.1 Introduction.....	33
4.2 The experiment.....	33
4.3 A brief outline about AC losses.....	33
4.4 The calibration procedure.....	37
4.5 Temperature measurements and sensors mounting.....	39
4.6 Uncertainty on input power.....	42

<b>5. Numerical model and simulation results</b>	<b>44</b>
5.1 Introduction.....	44
5.2 The Cryolab experiment model.....	45
5.3 Mesh.....	47
5.4 Initial and boundary conditions.....	47
5.4.1 Initial conditions.....	48
5.4.2 Boundary conditions.....	48
5.5 Heat inputs.....	49
5.6 Temperature comparison.....	50
5.7 Simulation results.....	51
5.8 Analytical validation.....	52
5.9 Analysis of the results.....	55
5.10 Time constants.....	58
5.11 Discussion of the results.....	58
5.12 A first consideration.....	60
5.13 The fall of the adiabatic condition.....	62
5.14 Some other comparisons: the error bands.....	63
5.15 Heating distribution.....	66
5.16 The sign of the second derivative.....	68
5.17 A possible explanation.....	70
5.18 A resume of the approach.....	71
5.19 AC losses computation.....	71
<b>6. Tests at the SM 18 facility</b>	<b>72</b>
6.1 Introduction.....	72
6.2 Geometry of a quench heater.....	72
6.3 Boundary conditions.....	73
6.4 Outer layer quench heater tests.....	73
6.5 Interlayer quench heater tests.....	75
<b>7. Conclusion</b>	<b>82</b>
<b>Acknowledgement</b>	<b>83</b>
<b>Appendix I. Effective thermal conductivity of Nb<sub>3</sub>Sn impregnated Rutherford cables</b>	<b>84</b>
A.I.1. Rutherford cables.....	84
A.I.2. Assumptions of the study and definitions.....	85
A.I.3. Local and global reference systems.....	86
A.I.4. Computations.....	88
A.I.4.1. Thermal conductivity along the y' axis.....	88
A.I.4.1.1. Copper fraction in a strand.....	89
A.I.4.2. Thermal conductivity along the x' axis.....	90
A.I.4.3. Thermal conductivity along the z' axis.....	96
A.I.4.4. Tensor rotation and effective thermal conductivity.....	96
A.I.4.5. Thermal conductivity on a multiple twist-pitch scale.....	98
A.I.4.6. Comparison with experimental measurements.....	100
<b>Appendix II. Volume of metallic parts of the Cryolab sample</b>	<b>104</b>
<b>Appendix III. Detailed data about the experiments</b>	<b>105</b>
<b>Bibliography</b>	<b>109</b>

# 1. CERN and the Large Hadron Collider

## 1.1 CERN and its aim

CERN, acronym for Conseil Européen pour la Recherche Nucléaire, is the European laboratory for nuclear research, created in 1954 just few years after the end of the Second World War.

The idea behind the establishment of the center, which laid in the mind of the French physicist Louis De Broglie and which was then supported by other scientists as the Italian Edoardo Amaldi, was to create a place that could gather the best minds all over Europe, in order to carry out fundamental research both in theoretical and experimental physics, while trying to stop the so-called “mind-drain” from Europe to United States, which characterized the war years.

The *Convention for the Establishment of the Organization* [1] states, in its Purposes, that “the Organization should provide for collaboration among European states in nuclear research of a pure scientific and fundamental character, and in research essentially related thereto. The Organization shall have no concern with work for military requirements and the results of its experimental and theoretical work shall be published or otherwise made generally available”.

These words, from which shines a crystalline purpose, derive the main activities of the center. They are basically three: 1) Provide a unique complex of accelerators and facilities to study nuclear physics; 2) Provide a strong international environment, where people from all over the world can gather, in order to push the boundaries of science and knowledge, in a general sense; 3) Deepen the study in fundamental physics, to uncover the secrets of nature and the universe.

## 1.2 The synchro-cyclotron and accelerators operation

The first machine to be built at CERN was the synchro-cyclotron, which at its time became the most powerful accelerator in the world, and whose construction lasted from 1955 to 1957. Its operation was based, as other accelerators, on the combination of electric and magnetic fields, which both act on charged particles. There is a substantial difference in the way electric and magnetic forces act on a particle, which is addressed in eq.(1.1)

$$\vec{F} = q\vec{E} + q \vec{v} \times \vec{B} . \quad (1.1)$$

The first term on the right-hand-side (*rhs*) represents the electric force, which acts in the same direction of the field, so that it makes a work on a particle. The second term, on the other hand, represents the magnetic force, which acts in the direction normal to the field, so that it does not apply a work on the particle. To resume, electric fields accelerate particles, which in turn means give energy to them, while magnetic fields can bend particles.

The machine made use of massive vacuum pumps to extract the air from the inside of its chamber, and to avoid particles to collide with air molecules. In the proton source, hydrogen gas was ionized so that their nuclei, being protons, could be injected in the middle of the synchro-cyclotron. Two D-shaped electrodes with opposite polarity were fixed inside the vacuum chamber, in the middle of the external magnet. The magnet consisted of two coils, each wound with 6380 m of aluminum conductor, carrying 1800 A and dissipating a total power of 750 kW. Pole discs had a diameter of approximately 5 m and the total weight of the magnet was 2500 tonnes [2]. Protons, having a positive charge, were driven to the negative electrode, starting their acceleration through the gap between the two electrodes. The magnetic field forced them to follow a circular trajectory, and they returned to the gap after one-half turn. Meanwhile, the radio-frequency generator reversed the polarity of the two electrodes, so that protons were now attracted to the opposite electrode, continuing their path and gaining more energy. This process was repeated over and over again, and every time protons completed a half turn, the radius of their path increased. After completing more than 100.000 turns they reached an energy of 600 MeV, corresponding to 80% the speed of light [46].

The synchro-cyclotron played a fundamental role in the physics of the pion, particularly in studying its rare decays. From 1964 the machine began to focus on nuclear research, leaving particle physics to the new and more powerful proton-synchrotron. Its life went on, though, providing beams for the ISOLDE facility, dedicated to radioactive ion beams. It was finally dismissed in 1990, when the line was transferred to the proton-synchrotron booster.

### 1.3 The CERN accelerator complex.

It is worth to briefly describe the accelerator chain at CERN. The journey starts from a tiny bottle of hydrogen which, at a precise rate of 1.2 seconds, releases  $10^{14}$  hydrogen atoms which go into the source chamber of a linear accelerator, LINAC 2. Here, hydrogen atoms are stripped off from their electrons, to leave hydrogen nuclei, which are protons, indeed. Having a positive charge, they can be accelerated by an electric field, and by the time they emerge they gain an energy of 50 MeV, corresponding to nearly 30% of the speed of light. They are now about to enter the proton-synchrotron booster (PSB). Started operation in May 1972, the PSB is made up of four superimposed rings. Its main function is to increase the number of protons that its next companion, the Proton-Synchrotron (PS) can accept. In fact, in order to maximize the intensity of the beam, the initial packet is divided into four, one for each of the Booster rings. At this point, a linear acceleration would be impractical, the reason why the PSB is circular, being 157 m in circumference. Protons are here also accelerated by means of a pulsed electric field, which increases the energy of the beams at each turn. As seen for the cyclotron, magnets are used to bend the particles and keep them on track. The concept of a synchrotron is that particles are bent on a fixed path, with the magnetic field increased over time, and synchronized with the energy of the beam. All accelerators we will describe from this moment on are synchrotrons.

The PSB accelerates particles up to 1.4 GeV, corresponding to 91.6% the speed of light. It also squeezes the bunched in order for particles to stay closer together. Recombining the packages from the four rings, the next step is the Proton-Synchrotron (PS), the third stage of the particle journey. The PS was the second machine inaugurated at CERN and accelerated its first protons on 24 November 1959, also becoming for a short period the world's highest energy particle accelerator, and the first CERN synchrotron. From this type of particle accelerators comes the term "synchrotron radiation", which is used in a wide range of applications, from geology to particle therapy. The proton-synchrotron at CERN is characterized by a circumference of 628 m, and has 277 conventional (ferromagnetic) electromagnets, where 100 are dipoles to bend the particle beams. It operates up to 25 GeV and it is a key component in the CERN's accelerator complex.

In its early days, LINAC 2 sent particles directly to the PS. However, its low energy limited the number of protons that the PS could accept and this was the reason to build an intermediate stage, the PSB. Inside the PS, protons circulate for 1.2 seconds, reaching 99.9% the speed of light. A point of transition is reached here: energy transmitted to particles through electric fields does not translate in a further increase in particle velocity, so all the energy contributes only to increase the mass of the particles. This is well explained thanks to the special theory of relativity

$$m = \frac{m_0}{\sqrt{1 - \frac{v^2}{c^2}}} . \quad (1.2)$$

In eq.(1.2)  $m_0$  is the mass of the particle at rest,  $v$  is the velocity of the particle, and  $c$  is the speed of light. To be more precise, it is to be said that in experiments *everything behaves in the same way as if the mass of particles was increased*. Despite this subtle aspect, it will make no difference, for our present purposes, to consider that the energy increase translates in an effective increase in the mass of the particle.

It is worth to define something else before going on. The energy of the particles is commonly expressed in a unit called *electronvolt*, which by definition is the energy acquired by an electron moving in an empty region of space between two points which have an electrical potential difference of 1 V. An electronvolt is a tiny amount of energy, corresponding to

$$1 \text{ eV} = 1.602 * 10^{-19} \text{ C} * 1 \text{ V} = 1.602 * 10^{-19} \text{ J} . \quad (1.3)$$

In the theory of special relativity, energy and mass are interchangeable, due to the Einstein's relation

$$E = mc^2 . \quad (1.4)$$

Therefore, the mass of the particles can be expressed in terms of energy, in  $eV/c^2$ , or  $eV$ , to be shorter. The mass of the proton at rest is  $938.27 \text{ MeV}/c^2$ , almost 1 billion eV. When protons pass through the PS, they acquire an energy of 25 GeV, equivalent to 25 times their mass at rest.

Particles from the PS are injected to the Super-Proton-Synchrotron (SPS). The SPS is the second largest accelerator at CERN, being 7 km in circumference. It began its work in 1976 and during his operation has enabled various kind of studies, from the inner structure of the proton to the investigation of the asymmetry between matter and antimatter. Its major contribution came in 1983 with the discovery of the  $W^\pm$  and  $Z^0$  bosons, which mediate the weak force, using proton-antiproton collision. That discovery was awarded with the Nobel prize in Physics to the Italian physicist Carlo Rubbia and the Dutch Simon van der Meer.

The SPS is properly designed to receive protons at 25 GeV and “accelerates” them up to 450 GeV. It has 1317 conventional (room-temperature) magnets, including more than 700 dipoles to bend the beams. When the packets are energized sufficiently, they are launched into the orbit of the Large Hadron Collider (LHC). Let’s have a look at Fig. 1.1, to visualize what has been said so far.

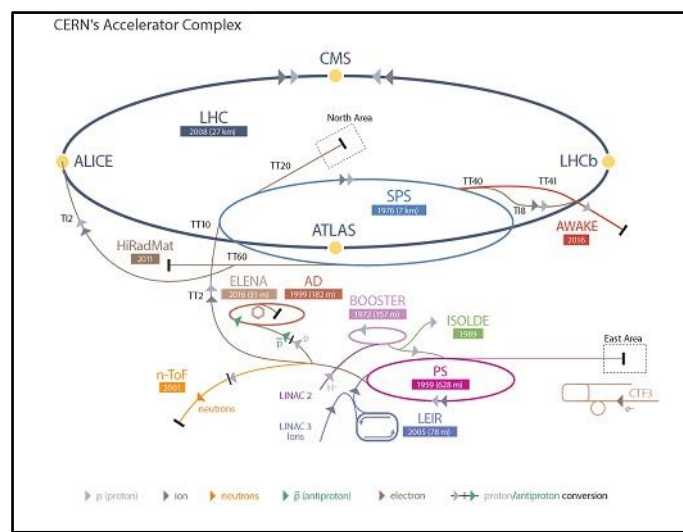


Fig. 1.1: The CERN's accelerator complex.

Being one-hundred meters below ground and 27 kilometers in circumference, the LHC is the world’s biggest and more powerful accelerator. It contains two beam pipes, one circulating clockwise and the other counterclockwise. It takes 4 minutes and 20 seconds to fill each LHC ring, and 20 minutes for the protons to reach their maximum energy of 6.5 TeV. The beams collide in 4 points in the machine, where detectors are placed. They are: ATLAS, CMS, ALICE, and LHCb; the energy in the center of mass is the sum of that of the two beams, namely 13 TeV. Eq.(1.4) shows how a certain amount of energy can be converted into mass, so the higher is the energy, the higher the resulting mass can be. The reason why all the efforts during the past 60 years have been made to go higher in energy are due to this rather simple idea. In fact, as the mass which can be created is higher at higher energies, also the probability that rare phenomena can happen becomes higher. Probability is also related to luminosity, which will be explained hereinafter.

ATLAS and CMS are two general-purpose detectors, which investigate a wide range of particle physics. They were the protagonists of the discovery of the Higgs boson, announced in July 2012, which ended a 50-years race for its search. Similarly to 1983, it brought to the assignment of the 2013 Nobel prize in Physics to the British physicist Peter Higgs and the Belgian François Englert, who independently proposed the Brout-Englert-Higgs mechanism in 1964. The two detectors are also looking at the possible existence of extra dimensions and dark matter particles, in search for physics beyond the Standard Model. ALICE and LHCb, on the other hand, have different objectives. ALICE studies the properties of the quark-gluon plasma, a form of matter that is supposed to have existed at the very beginning of the Universe, few fractions of a second after the Big Bang. It has been so far observed that this mixture behaves as a very particular fluid, being 30 times denser than an atomic nucleus, but that also having zero viscosity, as a perfect fluid. LHCb, where the “b” stands for beauty

(after the name of the corresponding quark), is the smallest of the four detectors, and investigates the existing asymmetry between matter and antimatter.

The LHC is an outstanding machine, which represents the peak of the efforts made by generation of scientists all over the world. Despite all that LHC represents, CERN is more than that. Several other experiments are conducted there. To give some examples, the aim of the ALPHA experiment is to study the properties of anti-matter, and of anti-hydrogen atoms, in particular. One of its goals will soon be the measurement of the behavior of the anti-atoms in the Earth's gravitational field. Another important test will be the analysis of the spectrum of the anti-hydrogen, to put the famous CPT symmetry at test. There are other wonderful pieces of science at CERN, such as nTOF, for the study of interactions between neutrons and nuclei, ISOLDE, for the exotic atomic nuclei, and the CERN Neutrinos to Gran Sasso, whose aim is to investigate neutrino properties as its changes in flavor.

#### 1.4 The High luminosity LHC

The LHC is a synchrotron-type accelerator, which means that the magnetic field is increased over time in order to follow the energy increase of the beams. Electrical fields are used to accelerate particles, through RF cavities which operate frequencies around 400 MHz. Magnetic fields, on the other hand, have three main roles in a particle accelerator: 1) Beam bending; 2) Beam focusing; and 3) Particle detection.

The bending of the beams is achieved using dipole magnets (MB, Main Bending), while focusing is done thanks to quadrupole magnets (MQ, Main Quadrupole). Particle detectors take also advantage of magnetic fields to bend particles inside the detector itself, making it easier to reveal the charge and mass of the particles, relying on the covered path when subject to a given field.

Back in 2011, studies for the enhancement of the LHC began, which would have involved a 15-year project, whose aim was to raise the potential of discoveries of the machine after 2025. The main goal of the High-luminosity project is to increase the luminosity of the LHC by a factor ten beyond its first design project, enabling to gather much more statistics. This may lead to a better understanding of the 10 TeV energy scale and potentially bring to new discoveries.

Luminosity is an extremely important indicator of the performance of an accelerator, and is defined as the number of events detected,  $N$ , in a certain time,  $t$ , to the interaction cross-section,  $\sigma$  [3]

$$L = \frac{1}{\sigma} \frac{dN}{dt} \quad \left[ \frac{\#}{cm^2s} \right] . \quad (1.5)$$

In practice,  $L$  is dependent on the particle beam parameters, such as beam width and flow rate. A very important quantity is also the integrated luminosity, which is the integral of the luminosity with respect to time

$$L_{int} = \int L dt . \quad (1.6)$$

Luminosity and integrated luminosity are crucial parameters to characterize a particle accelerator. The LHC has the highest luminosity with respect to all the other accelerators ever built in the world, sharing it with the KEKB in Japan, with a value of  $2.1 * 10^{34} cm^{-2}s^{-1}$ .

The effort to be put in place to achieve luminosities ten times higher than the present values will be very demanding from a technological point of view. Several components of the machine will need replacement or new installation, and can be summarized in the following:

- Main Focusing magnets
- Main Bending magnets
- Crab cavities
- Power transmission lines
- Accelerator chain

One of the most relevant aspects consists in increasing the “squeezing” of the beams. This is put in practice using sets of quadrupole magnets. The High-luminosity project aims at the substitution of existing quadrupoles with new generation ones, which will make use of  $Nb_3Sn$ , a superconducting material which was never used before, but which enables to reach magnetic fields much higher than the present material,  $Nb-Ti$ . New versions of the main bending magnets will also be built, using again  $Nb_3Sn$ . The magnets will be shorter than in the present machine, each being 5.5 meter-long, and coupled in pairs so that 4 meters will be left to have additional space for corrector magnets, thus enabling a better control of the beams even far from the interaction regions. One single demonstrator of the so-called 11T dipole will be installed during the Long Shutdown 2 (2019-2020) and put into operation during the Run 3 (2021-2023).

Another fundamental aspect of the project are the crab cavities, an innovative superconducting equipment which will give the particle bunches a transverse momentum before meeting, thus enlarging the overlap area of the two bunches and increasing the probability of collision. Sixteen of such cavities will be installed close to the main detectors, ATLAS and CMS.

Superconducting transmission lines will connect the power converters to the accelerator. This new type of cables makes use of both high-temperature superconductors (HTS) and magnesium diboride ( $MgB_2$ ) superconductors, representing the very first industrial application of such materials. They are able to carry currents of record intensities, up to 100.000 amperes.

The injector chain described in Section 1.3 requires some major upgrade. LINAC 2 which has been in operation for 40 years, is going to be replaced by a more powerful linear accelerator, LINAC 4, which brings particles up to 160 MeV, becoming the first element of the accelerator chain. Other interventions are also planned on the PSB, the PS, and the SPS. Last, but not least, due to the much higher rate of radiation generated by the increase in luminosity, works of civil engineering are necessary in order to provide new underground facilities for electrical equipment (power converters).

## 2. Superconductivity

The purpose of this chapter is to give an overview on superconductivity, providing a first historical introduction and description of the main features of superconducting materials. The attention is then focused on the application of superconductivity for cables and coils production for the construction of accelerator magnets. The discussion is inspired by [5] and [44].

### 2.1 Introduction and historical background

Superconductivity is a special property of various materials, which can carry current under specific conditions, without any losses. The history of superconductivity began in 1908 with the work of Heike Kamerlingh Onnes, after a race that spanned all along the 19<sup>th</sup> century to reach lower and lower temperatures. During the 1870s only a few substances had not yet been liquified: oxygen, helium, nitrogen, and hydrogen, which for this reason were called “permanent gases”. The saturation temperature of some cryogenic fluids, at ambient pressure, is reported in Table 2.1.

Substance	Saturation T
LHe	4.2 K
LH <sub>2</sub>	20 K
LN <sub>2</sub>	77 K
LO <sub>2</sub>	90 K
LCH <sub>4</sub>	111 K

Table 2.1: Saturation temperatures of some cryogenic fluids.

The term “cryogenics” is usually referred to temperatures below -100° C. One of the biggest problems during the 19<sup>th</sup> century was to make vacuum in order to remove the mechanism of heat exchange by convection, which was achieved by Dewar in 1898. Ten years later, Onnes managed to liquefy helium (in a volume of 60 cm<sup>3</sup>), something of paramount importance, since it made available a cold reservoir to conduct experiments at very low temperatures. In that sense, liquid helium played the same role as the Volta pile for the electromagnetic field, which on its side made available a source of direct current.

In the same laboratory, but three years later, in 1911, studying the electrical properties of a very pure sample of mercury (Hg), Onnes observed the phenomenon of superconductivity for the very first time. To be more specific, Onnes noticed a sudden transition in the resistance-to-temperature diagram for mercury, as Fig. 2.1 depicts. The sample resistance diminished to non-measurable values, and mercury passed to a state with completely different electrical properties, unknown until that moment. Onnes decided to call it “superconducting state”.

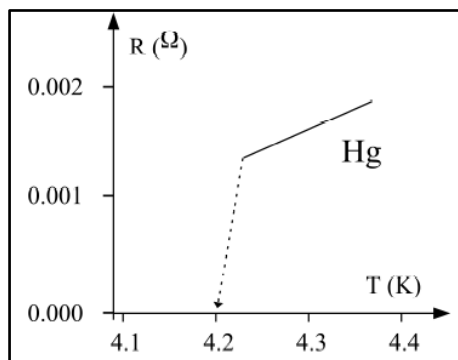


Figure 2.1: Electrical resistivity as a function of temperature for mercury.

Using the words of Onnes himself, “There is plenty of work which can already be done, and which can contribute towards lifting the veil which thermal motion at normal temperature spreads over the inner world of atoms and electrons” [4].

Researches have shown that 26 metallic elements and around 1000 alloys and compounds become superconducting at low temperature.

Before the discovery of superconductivity, resistivity was thought to be the sum of two contributions (Matthiessen formula)

$$\rho = \rho_T + \rho_R , \quad (2.1)$$

where the first is due to thermal motion and the second to crystalline imperfections. Electrical resistivity in metals depends on the interactions of the conduction electrons with ions of the crystal lattice, which vibrate around their equilibrium position. As temperature decreases, the amplitude of motion of the ions and the energy given by the electrons to the crystalline lattice, does the same. At zero Kelvin, the motion stops, and the remaining energy transfer is due to the imperfections in the lattice. Consequently, an ideal crystal at 0 K would have no resistivity, while a real crystal would still have a residual  $\rho_R$ , dependent on the level of imperfections. Regarding traditional materials, one can define the RRR (Residual resistivity ratio)

$$RRR = \frac{\rho(273\text{ K})}{\rho(4\text{ K})} , \quad (2.2)$$

which is expressed as the ratio of the resistivity at 273 K and at 4 K, which varies significantly with the degree of purity. This can be also visualized in Fig.2.2.

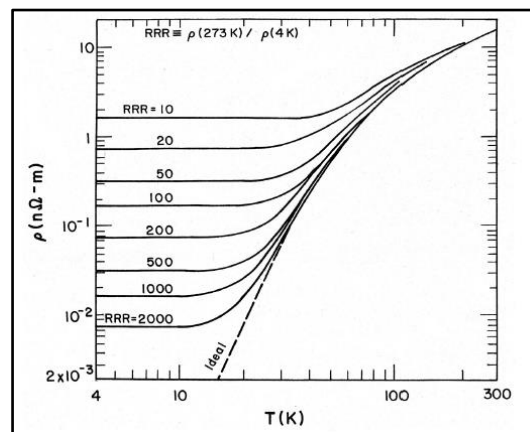


Figure 2.2: Resistivity dependence of copper from temperature and for different value of the RRR.

In practice, the higher the purity, the less the resistivity at 4 K, and the higher the RRR is. This is what classical theories predicted about the behavior of metals at low temperature. Thanks to quantum theory, though, it was discovered that  $\rho$  could not even arrive at zero, due to Heisenberg Uncertainty Principle. That's why helium does not become a solid even close to 0 K, and to reach that state it needs to be put under high pressures.

Despite the classical theory, some metals were discovered to behave very differently from copper: when they are cooled, their resistance decreases linearly, until a certain value of temperature, called the **critical temperature,  $T_c$** , at which it drops to non-measurable values. Such materials are called superconductors, and the transition happens independently from the degree of purity of the crystal. The transition is actually a real phase change; it does not happen only electrically, but also thermodynamically, being a second-type transition, without any associated latent heat.

This can be observed in Fig.2.3.

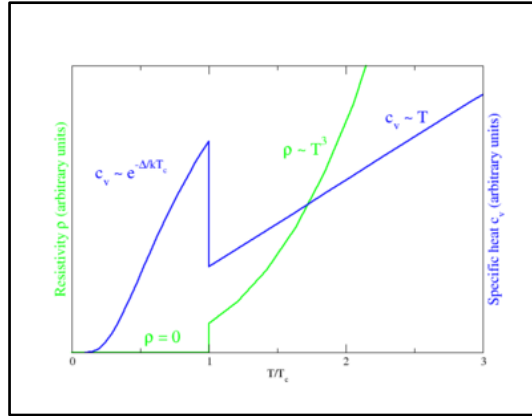


Fig.2.3: The blue curve depicts the specific heat of the super-electrons compared to normal electrons.

It represents the ratio of the normalized specific heat, namely that of super-electrons referred to normal electrons,  $C_{e,s}/C_{e,n}$ , versus the normalized temperature,  $T/T_c$ . A similar behavior can be observed for magnetic susceptibility.

### 2.2 Perfect diamagnetism (Meissner effect)

The absence of electrical resistivity at very low temperatures does not enable, alone, to categorize a material as a superconductor. Conventional materials have a resistivity approaching zero, as well. The key feature of superconductors is their response to external magnetic fields, which reveals their diamagnetic nature.

Both for an ideal conductor and a superconductor, the Faraday law is true

$$\vec{\nabla} \wedge \vec{E} = -\frac{\partial \vec{B}}{\partial t}, \quad (2.3)$$

while the Ohm law, also called constitutive law

$$\vec{E} = \rho \vec{J}, \quad (2.4)$$

is valid only for an ideal conductor. When resistivity goes to zero, no electric field is present inside the material, and in turn, there is also a constant magnetic field. This means that, cooling a sample of conductor material and inserting it into a static magnetic field, the magnetic field vector,  $\vec{B}$  remains zero inside the material. Conversely, if one puts the material inside the field, at room temperature, when cool down is applied, the field remains constant in the material even after removing the field. The state of magnetization of an ideal conductor does not only depend on external conditions, but also on the sequence perform to arrive at certain conditions. This is properly shown in Fig. 2.4.

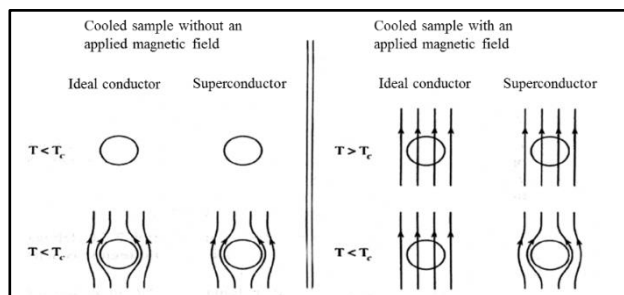


Fig.2.4: Different behavior of an ideal conductor and of a superconductor when subject to external fields and cooling. Field always remains zero in a superconductor.

A superconductor, on the other hand, always presents no magnetic field ( $\vec{B} = \vec{0}$ ) inside it, whichever sequence of external field and cooling down is applied. Such effect of repulsion of magnetic field lines is what really distinguishes an ideal conductor from a superconductor, and it is called *Meissner effect*.

The Ampère law is important, as well

$$\vec{\nabla} \wedge \vec{B} = \mu_0 \vec{J} . \quad (2.5)$$

In fact, if  $\vec{B}$  is zero, then also  $\vec{J}$  should be zero, the reason why shielding currents generate a magnetization only on the surface of the material. The total field inside the material can be expressed by the contribution of two factors, the external field,  $\vec{H}$ , and the magnetization of the material itself,  $\vec{M}$

$$\vec{B} = \mu_0 (\vec{H} + \vec{M}) . \quad (2.6)$$

Again, if  $\vec{B}$  is zero, then  $\vec{M} = -\vec{H}$ , which means that the magnetization given by the material acts in the exactly opposite way of the external field. Currents flow in the first 10-100 nm layer, the reason why the magnetic field can also penetrate for a certain depth, decaying with an exponential law from the outside to the inside. This can be seen in Fig.2.5.

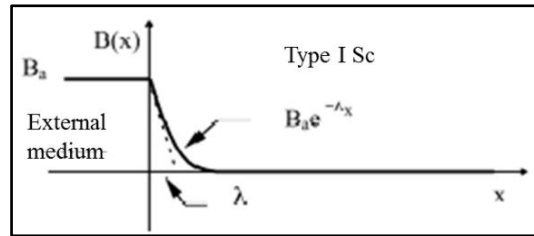


Fig.2.5: Field trend across the surface of a sample made of a type I superconductor.

The layer where currents flow is called **penetration depth**,  $\lambda$ , and represents the depth at which the external induction field is able to penetrate. It is defined in a way that

$$B_a \lambda = \int_0^{+\infty} B dl , \quad (2.7)$$

and its dependence on temperature is given by an experimental law

$$\lambda(T) = \frac{\lambda(T=0)}{\sqrt{1 - \left(\frac{T}{T_c}\right)^4}} . \quad (2.8)$$

Even though for a completely different purpose, eq.(2.8) resembles in its form eq.(1.2). This means that, when  $T$  is relatively far from the critical temperature,  $\lambda$  is almost unaltered with respect to its maximum value; on the contrary, as it approaches  $T_c$  it gets bigger, due to the asymptote. When the magnetic inductance penetrates completely inside the material, then it returns to the normal state.

### 2.3 Critical parameters of superconductors

The only quantity that has been described until now is the critical temperature, which governs the transition to the superconducting state. However, there are other parameters that determine the transition, and the superconducting state is given also by current density,  $J$ , and magnetic field,  $B$ . Together, they define a critical curve, shown in Fig.2.6.

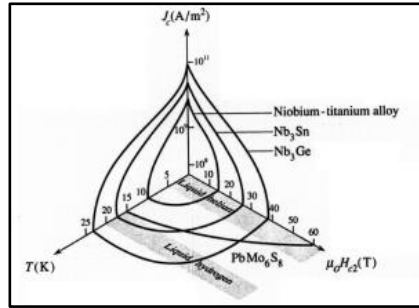


Fig.2.6: Critical curve ( $J, B, T$ ) for three superconducting materials.

If the critical surface is cut at constant temperature, one can see the variation of  $J_c$  with  $B$ .

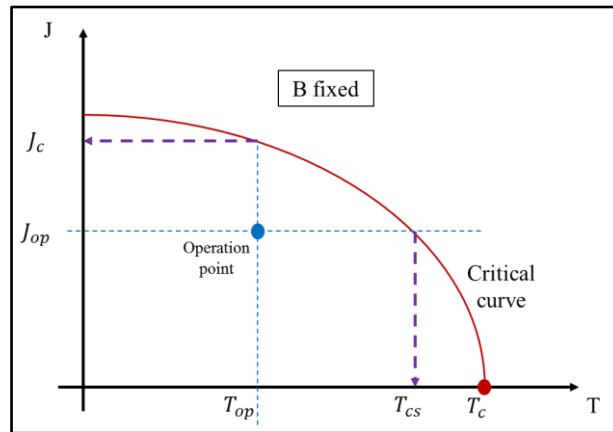


Fig.2.7: An example of  $T_{cs}$  and  $J_c$  at a certain operating condition.

Fig.2.7 shows the relevant quantities in the operation of a superconductor. Drawn in red is the critical curve, at a given external field. Starting at a certain value of operating current density and temperature,  $J_{op}$  and  $T_{op}$ , if temperature is increased at fixed current, one arrives to cross the red curve, which means that the current sharing regime is established: the material is still superconducting, but current starts to flow also in the surrounding copper of the cable (superconducting filaments are plunged in a copper matrix which acts as a stabilizer and brings the exceeding current). At  $T_c$ , the material loses completely the superconducting state and returns normal conducting. On the other hand, starting from the operation point and keeping the temperature fixed, one can increase the current until  $J_c$ , where the superconducting state is lost again. Unfortunately, there is no parallel for current as for the current sharing temperature as for temperature itself. Conventional conductors, like copper or aluminum, can carry around 1-2 A/mm<sup>2</sup>, arriving at a maximum of 6 using powerful cooling systems. Superconducting cables, on the other hand, can reach 500 A/mm<sup>2</sup> (meant as an engineering current density) as it is the case for accelerator cables, thus helping to keep magnet systems compact.

Finally, a fourth quantity is a critical parameter, namely the frequency. This is not normally taken into account, but can play a significant role above 10<sup>9</sup> Hz, bringing to the transition to the normal state at around 10<sup>11</sup> Hz. The reason for this can be better understood in next sections, but it is basically related to the energy that super-electrons receive from an oscillating electric field. For all the applications we are interested in, frequency can be neglected to be a critical parameter.

### 2.4 Type I superconductors

Eq.(2.6) has shown that, if the magnetic field inside the material is zero,  $\vec{B} = \vec{0}$ , the magnetization generated by the material itself, by the superficial currents, is exactly the opposite of the induction field. This remains true until the critical field is reached, when a sudden transition is observed (Fig.2.8).

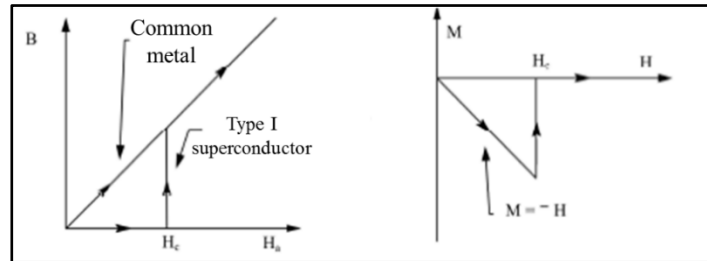


Figure 2.8: Magnetic induction  $B$  and magnetization  $M$  inside a type I superconductor as a function of the applied magnetic field.

A high number of elements of the periodic table shows the superconducting state, between the 0.325 K of rhodium (Rh), to the 9.3 K of niobium (Nb). Most of them belongs to type I superconductors, which cannot be used to build magnets (critical fields are in the order of mT). It is important and curious to underline that common conductors are not superconductors. In other cases, it is the shape of the material to determine superconductivity (as for Beryllium), and sometimes the composition of two non-superconducting elements gives a superconductor compound. Once again, some materials become superconducting only under the effect of pressure.

### 2.5 Type II superconductors

In type II superconductors, the transition to the normal state does not happen with a sharp profile as for type I materials. Increasing the field, the material remains initially in a perfect diamagnetic state, until the so-called lower critical field,  $H_{c,1}$  is reached. Here, the magnetic flux starts to penetrate inside the material, bringing it to the “mixed state”. The “mixed” region is much wider than the Meissner region, and magnetization diminishes as one approaches the upper critical field,  $H_{c,2}$ , as Fig.2.9 depicts.

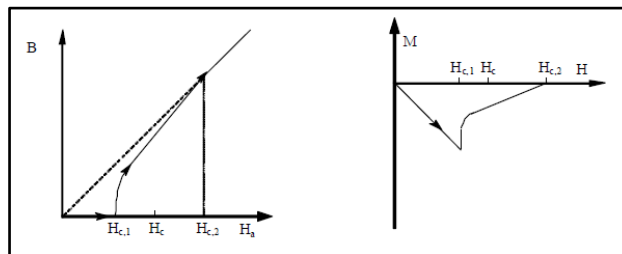


Fig.2.9: Magnetic induction (a) and magnetization (b) as a function of the applied magnetic field, for type II superconductors.

In the theory by Abrikosov (which was developed in analogy to super-fluidity), the penetration of the magnetic field in the material is quantized and happens thanks to flux quanta, called vortices ( $\varphi_B = 2.07 * 10^{-15} Wb$ ). Super-currents rotate around vortices and sustain the field inside them. Fig.2.10 shows the idea.

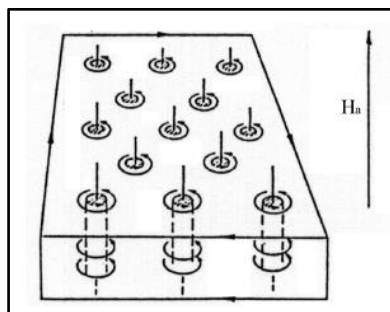


Fig.2.10: Simple drawing of the super-currents that support the flux inside vortices.

Current can easily flow around vortices, but the problem comes when their number increases. In fact, vortices repel each other, so they tend to distribute uniformly in the material, at the vertices of hexagonal structures, in order to minimize Gibbs energy.

When a current flows in the material, a Lorentz force is exerted on the vortices, which tries to make them move, originating a dissipative phenomenon (*flux flow*). To avoid dissipation, lattice imperfections are used to literally block the vortices, in a procedure called *pinning*. This can be enhanced through thermal and mechanical treatments which try to bring the average distance among imperfections close to the mean distance among vortices. If the pinning force,  $F_p$  is bigger than the Lorentz force,  $F_L$ , vortices remain blocked, but as soon as the two forces are the same, vortices start to move causing dissipation. The threshold is given by  $F_p = F_L$ , and  $J_c = F_p/B$ . The critical current density is then closely related to the ability to have a very high value of the pinning force.

To resume the differences between Type I and Type II superconductors, we can have a look at Fig.2.11.

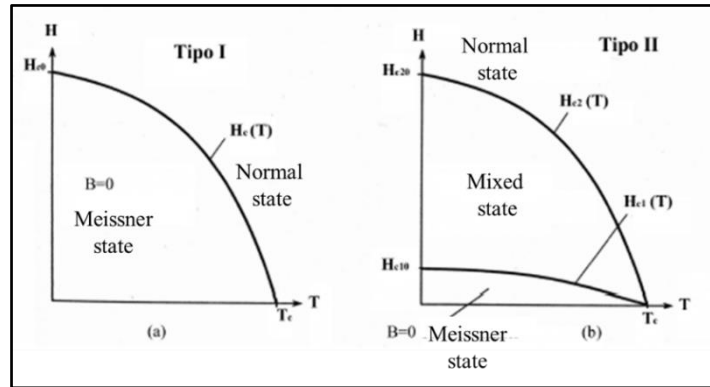


Fig.2.11: Comparison of critical curves of type I and II superconductors. Type II is characterized by the wide mixed state.

Type II superconductors have values of  $H_{c1,0}$  in the same order of  $H_c$  of type I superconductors. However, values of the upper critical field,  $H_{c2,0}$  can be very high, so that for some materials are still unknown.

## 2.6 Theories of superconductivity

The very first description of the macroscopic effects of superconductivity came from London, with his two famous equations. The first is

$$\vec{E} = \mu_0 \lambda^2 \frac{\partial \vec{J}}{\partial t} , \quad (2.9)$$

Which justifies the absence of resistance and it is derived from Newton second law of motion and the Ohm law for common materials. The second one, eq.(2.10) is the diffusion equation for the magnetic field, and gives reason of the Meissner effect

$$\nabla^2 \vec{B} - \frac{1}{\lambda^2} \vec{B} = 0 . \quad (2.10)$$

After London's macroscopic explanation of superconductivity, there were other descriptions of the phenomenon, all using quantum theory. The process was finally completed with the BSC (Bardeen-Cooper-Schrieffer) theory of 1957, which describes the isotopic effect. In fact, thanks to various experiments, it was discovered that

$$T_c M^{1/2} = constant , \quad (2.11)$$

where  $T_c$  is the critical temperature, while  $M$  is the mass of the specific isotope in the material. This relation made people realize that the crystal lattice played an important role in the superconducting phenomenon, differently from what was thought at the time, namely that interactions would have brought to dissipation. A force of attraction is actually exerted between electrons, so that two of them put together to form a pair. A certain amount of energy, in the form of a phonon, is given by a first electron to the lattice, which then given to a second electron. In this way the lattice acts only as a mediator, with no losses involved. Simultaneously, a boson is formed, which does not respond to the Fermi-Dirac statistics but to Bose-Einstein. The energy level occupied by the Cooper pairs is below the lowest energy for normal electrons, of the exact amount needed to break the couple. This energy can be provided in different ways, as thermal motion, magnetic field or even electric field (remind that frequency is a critical parameter). The amount of this energy is very little and corresponds to the photon exchanged with the lattice:  $\hbar\omega_n + 1/2$ .

The BCS theory works for elements and alloys as NbTi and Nb<sub>3</sub>Sn, but not for High-Temperature-Superconductors (HTS), which have a critical temperature above 77 K, the nitrogen saturation temperature. BSCCO and YBCO are the main materials in this field. The advantages generated by HTS are undeniable: much higher critical fields (so high that are in part still unknown), and the possibility to not rely on superfluid helium, thus using a much simpler cryogenic system. The disadvantage is that HTS, being ceramic materials, are very fragile. There are some empirical rules to describe the behavior of the critical temperature in materials.  $T_c$  is higher for elements that have an odd atomic number, it increases with the number of elements involved, and with the anisotropy of the material itself

$$T_c(Nb) < T_c(NbTi) < T_c(BSCCO) .$$

These are, of course, only empirical rules, and could be proved wrong with future discoveries.

### 2.7 High Temperature Superconductors (HTS)

The structure of an HTS (schematically shown in Fig.2.12) is formed by a series of Cu-O<sub>2</sub> layers spaced out by Calcium or Yttrium atoms. The n Cu-O<sub>2</sub> layers are closed by two blocks containing metals, rare earths and O<sub>2</sub>. Superconductivity acts along Cu-O<sub>2</sub> planes if they are properly adducted by the two blocks at the extremities, which constitute a reservoir for positive charges.

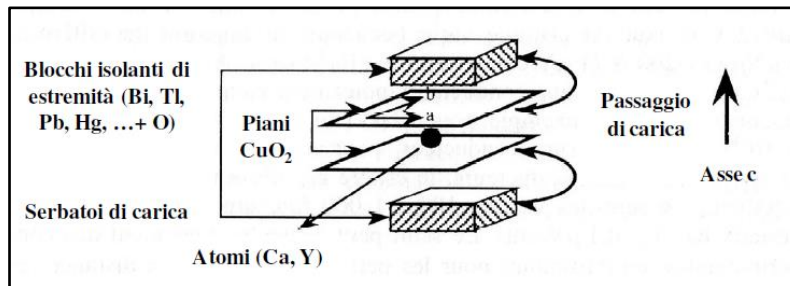
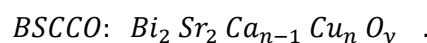


Figure 2.12: Typical structure of an HTS, with a, b, and c planes.

Currents easily flow along (a;b) planes, but much more unlikely along c. The orientation of the external field is highly important, too: a field along (a;b) planes is always better in terms of critical current density.

The superconductor is characterized by the number of planes between the insulation blocks, and by the elements they are made of. The number of planes is very important for the  $T_c$ , and the maximum is reached at n=3. The typical structure of both YBCO and BSCCO is that of perovskite, ABX<sub>3</sub>



In the composition of BSCCO, n can be either 2 or 3. In fact, its two possible composites are called 2212 and 2223, respectively. In YBCO, the role of A is sometimes carried out by Y, other times by Ca. Values of  $\delta$  must

be at least equal to 6.35 and more than 6.93 to maximize the  $T_c$ . Controlling the oxygen quantity and its maintenance is then extremely important during the material formation process.

Cooper pairs are the carriers of electric charge in superconductors, but they are not necessarily close in space. The coherence length,  $\xi$ , is the quantity that defines the interaction between electrons in a Cooper pair which is at a distance, indeed. If an insulation layer thinner than  $\xi$ , is interposed in some way, the material can remain in the superconducting state. LTS materials have very high  $\xi$  (as NbTi, Nb<sub>3</sub>Sn), so that grain borders do not represent a problem; on the contrary, one wants more of them because they act as pinning centers. The same does not happen with HTS, since  $\xi$  is smaller and the grain border would make  $J_c$  drop drastically with respect to the inter-grain. Therefore, a single crystal is grown in bulk materials (with dimensions around 25-30 mm) even if this does not enable to build cables. The texturation process is used to give preferential directions to the growth of grains, so that they can be aligned (RabiTs). This process is currently highly expensive, the reason why LTS are still much more used than HTS.

The biggest difference between LTS and HTS is due to the irreversible field,  $\mu_0 H^*$ , as Fig.2.13 shows.

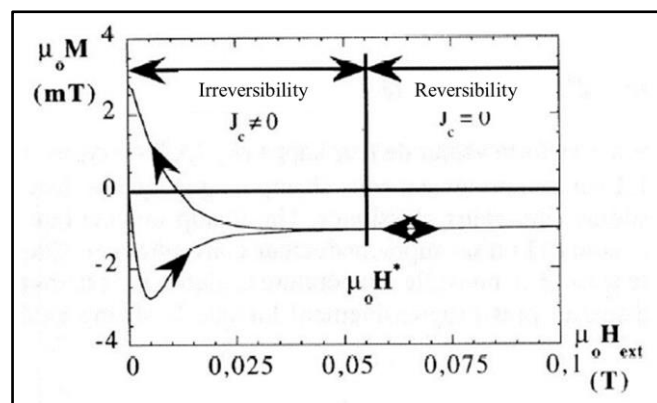


Fig.2.13: Magnetization curve of an HTS.

Above the irreversible field, the critical current density becomes zero, due to the perfect reversibility in magnetization. Above this threshold vortices behave as a liquid, so that the material cannot be used anymore. An HTS then shows 4 phases rather than 3 (Fig.2.14).

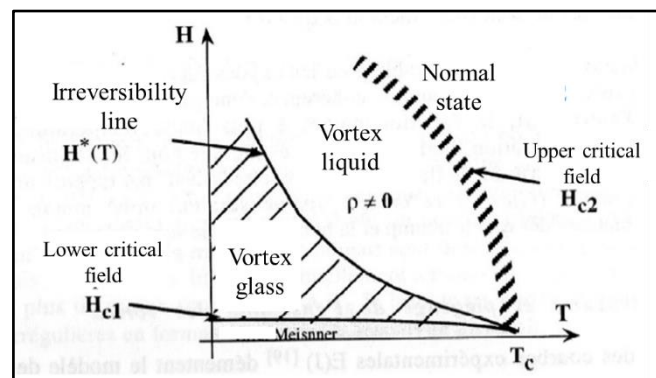


Fig.2.14: The four phases of an HTS. The vortex liquid appears, which makes materials unusable.

Below the irreversibility line, vortices are arranged in a glass structure, with a regular pattern as it happened for the Abrikosov mesh in conventional superconductors. Another difference is that vortices are two-dimensional, rather than three-dimensional, laying on Cu-O<sub>2</sub> planes.

BSCCO is much penalized by the irreversibility field above 77 K, so it is to be used at 4.2 K. Things are better for YBCO, which at 77 K can still sustain a 4 T field (which becomes 30 T at 4 K). A second problem of these materials is anisotropy: if field and planes are normal to each other,  $J_c$  drops.

To conclude, HTS have the relevant advantage to show very high critical fields and currents. On the other hand, they are fragile, anisotropic, and expensive, since they require the RabiTs process which constitutes a manufacturing difficulty. They also require a bigger amount of stabilizer compared to LTS, since they do not carry current during the transition at all, and without a stabilizer everything would break apart.

## 2.8 Technologies for superconducting materials

This paragraph is dedicated to the description of the technological processes for the production of cables and coils made of NbTi and Nb<sub>3</sub>Sn, with a special focus on accelerator applications.

### 2.8.1 Niobium-Titanium

Materials used to produce cables are built in thin filaments in order to reduce flux jump, and they are also immersed in a copper matrix for stabilization. A strand made of NbTi has a diameter between 0.81 and 0.83 mm and has a multi-filamentary structure. Production starts from NbTi bars (diameter: 20.3 cm, height: 76.2 cm and weight: 136.1 kg) firstly inserted in a Nb container, surrounded by an even bigger second container, made of copper. The resulting billet is extruded at cold and reduced in diameter in various stages, which bring to the formation of the filaments of the final cable. Then, the multi-filamentary billet is obtained inserting various filaments in an external copper container (called the Cu-can) and after a second, long process of extrusion, a single – one millimeter - strand is finally procured. The Cu can contains hundreds of superconducting filaments at this stage, each coming from one single billet of NbTi.

NbTi is used in 90% of applications and it has firstly been exploited for various reasons. First, it is a metallic alloy, which means that it is quite easy to manufacture and superconducting properties are almost independent from the applied strain, at the same time. Second, it can be used to produce fields up to 10 T, which is enough for most applications. It has a critical temperature,  $T_c$ , around 9 K, as Fig. 2.15 shows.

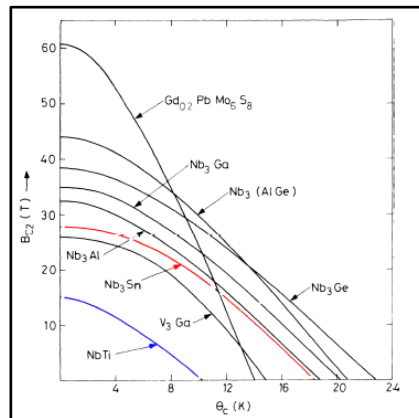


Figure 2.15: Upper critical field vs critical temperature for some superconducting alloys and compounds.

Heat and mechanical treatments at cold are put in place and interchanged once strands are formed. This is done in order to form  $\alpha$ -phases, rich in Ti, uniformly spaced inside the material, and alternated to  $\beta$ -phases at a reciprocal distance which should be very similar to that of vortices. In this way, they can act as pinning centers, in order to maximize the  $J_c$ . Artificial pinning centers (APC) are also added to the material, and can be made of pure Nb, NbTa, W, or Fe. In fact, adding Ta, the upper critical field,  $H_{c2}$ , increases by 1.3 T at 2K, even if the process of strand making becomes more complex.

NbTi was the first superconducting alloy to have a commercial application: it has optimal mechanical and metallurgical properties, being a ductile material, which makes it simpler to manufacture. The winding process is very easy, too, and the temperatures required for heat treatments are relatively low (250-600°C). The main disadvantages are given by the maximum field and temperatures of employment, which force to work with liquid helium.

### 2.8.2 Niobium-Tin

Nb<sub>3</sub>Sn was discovered in 1954, even before NbTi. It is an intermetallic compound, and this means that it has a crystalline structure, which makes it very fragile. The critical temperature of Nb<sub>3</sub>Sn is 18.3 K that can be

used to produce fields up to 25 T (Fig.2.15). Being very fragile is much more difficult to manufacture with respect to NbTi. As an example, it is very sensible to deformation, as Fig.2.16 depicts.

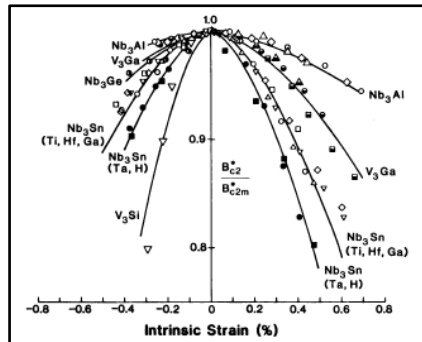


Figure 2.16: Upper critical field as a function of strain (J.W.Elkin,1984)

The upper critical field suffers from relevant decreases already at few decimal points of the strain. Consequently, strain is not negligible as it was for NbTi, and it affects all the critical parameters:  $J_c = J_c(B, T, \varepsilon)$ ,  $B_c = B_c(J, T, \varepsilon)$ ,  $T_c = T_c(J, B, \varepsilon)$ .

The manufacturing process for Nb<sub>3</sub>Sn is much more complicated than for NbTi. In fact, the superconducting compound must be in the form of the A15 phase, which requires temperatures in the range between 925 to 1050°C. This is quite a long process and enables the formation of grains, which need to be of the proper dimension in order to make their borders to act as pinning centers. At the same time, grains should not be too large (above 0.2 μm) since this dimension would become similar to the coherence length,  $\xi$ , thus causing a drop in the critical current.

There are two methods to form the Nb<sub>3</sub>Sn compound, which are the React-and-Wind and Wind-and-React techniques. In the latter, the material is firstly wound to form the coil and then is put in the oven at 1050°C to form the superconducting compound. Thanks to that, the material does not break apart when it is wound, which is instead the problem of the React-and Wind technique. Copper is also involved in the reaction, and acts as a stabilizer, resulting in a ternary phase diagram. To resume, the superconducting phase is formed thanks to diffusion by heat treatment, but there are some problems: at  $T > 700^\circ\text{C}$  the glass fiber insulation deteriorates, and ceramic materials should be used, which in turn, is expensive. Furthermore, the grain dimension is enlarged, and a compromise to keep  $J_c$  at acceptable values must be found. Finally, the different phases produced during the heat treatment have different densities, so that voids can be formed due to the different contraction coefficients of the elements inside the material itself.

### 2.8.3 Fabrication methodologies of Nb<sub>3</sub>Sn strands

Three techniques are commonly used to produce Nb<sub>3</sub>Sn strands: 1) Bronze route. In this technique, Niobium bars are inserted in a bronze (Cu + Sn) matrix, with a high tin content ( $\alpha$ -bronze). An anti-diffusive barrier prevents tin diffusion into copper. Fig.2.17 shows the idea.

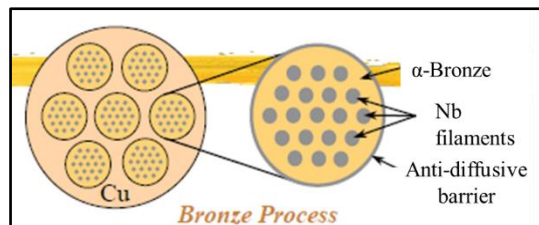


Figure 2.17: Bronze route process

It is important that copper does not mix with tin, which on the other hand, needs to diffuse in niobium. The anti-diffusive barrier made of tantalum is inserted for this reason, which also guarantees that copper remains pure thus being a heat and electricity conductor in order to stabilize the system.

2) Powder in tube. A  $NbSn_2$  powder is inserted in Nb tubes, immersed in a copper matrix. Copper remains very pure and the thermal treatment is short, but the material is not very ductile. Fig.2.18 depicts the system.

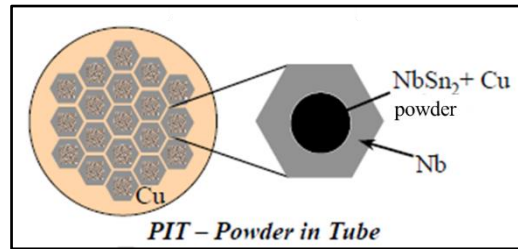


Fig. 2.18: Power-in-Tube process.

3) Internal Tin. In this last process, tin diffuses both into copper, forming bronze, and in niobium, but it is prevented from going in the outside copper by an anti-diffusive barrier. This is shown in Fig.2.19.

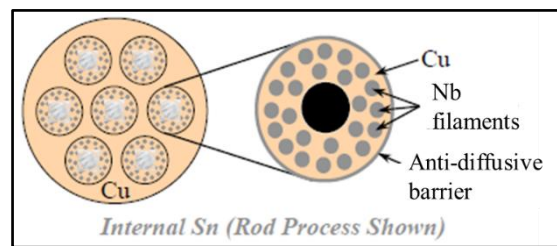


Fig. 2.19: Internal tin process

#### 2.8.4 Cables and coils for accelerator magnets

There are basically two types of cables which make use of  $Nb_3Sn$  strands: Rutherford cables and Cable-In-Conduit-Conductors (CICC). CICC are used for magnets for the controlled thermonuclear fusion (ITER project), while Rutherford cables are mainly exploited for particle accelerator magnets. Our attention will be focused on this second type of cables, since they are of interest for the present work.

Rutherford cables are manufactured through a winding process which involves the use of a winding machine (Fig.2.20).

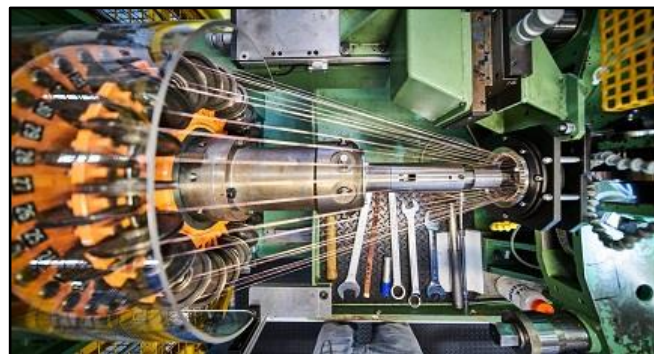


Figure 2.20: A part of the winding machine. On the left, one can see the numeration of each spool. Courtesy: CERN.

This machine is instrumented with 40 spools of  $Nb_3Sn$  conductor, one for each strand of the final cable, which are mounted in the first section of the machine. During operation the machine rotates, and each spool is equipped with an electric motor, to control the strand tension, so that it remains always close to the proper value. The 40 strands converge towards the rolling section of the machine, where they are pressed together by vertical and horizontal forces (30 kN and 5 kN, respectively), in order to give a flatten shape. A stainless-steel core is put between the two layers of strands that made up the cable and it is added in order to cut the coupling currents. Once the cable is formed, it passes to the quality control, where high-resolution cameras are used to analyze the shape of the cable, in order to verify that it fulfills all the required specifications.

The cable is now added with the insulation clothing. The first layer is made of mica, a composite material used for electrical insulation. It is also not perfectly closed around the cable for two main reasons: 1) ensure an opening to let epoxy resin to get in, and 2) avoid the risk of over-thicknesses, which would induce high mechanical stresses on the cable itself. The second layer is made of glass-fiber, a white material which is used as electrical insulator, as well. Both mica and glass-fiber are 50  $\mu\text{m}$  thick, so that their sum is 100  $\mu\text{m}$ . The combination of the two can be seen in Fig.2.21.



*Figure 2.21: Insulation materials of the Nb<sub>3</sub>Sn cable. On the left, in white, there is glass-fiber, while mica comes out from it, on the right. Total thickness is 100  $\mu\text{m}$ .*

The next step in the chain is coil winding. As underlined in Section 2.9.2, the reaction of the Nb and Ti to form the superconducting phase can only take place after winding, due to the high fragility of the Nb<sub>3</sub>Sn crystalline compound. One single cable is used for the winding and takes place in two steps. The coil has in fact two layers, the inner and the outer.

At first, the inner layer is wound, followed by a heat treatment in which temperature is brought to 150°C. This is done in order to let the coil “relax”, while it is also put under compression, in order to maintain the proper dimensions. Then, the radius of the cable winding is increased, such that the outer layer can be wound, as well. The heat treatment is repeated. The result is shown in Fig.2.22.

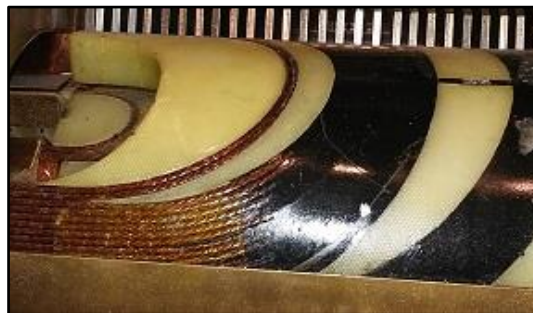


*Figure 2.22: The coil after winding, and before reaction. The thickness of a single cable can be seen.*

Reaction can now take place. Coils are placed inside a mold and then put in an industrial oven at temperatures around 670°C (the actual process is a little bit different from the other described above) for a couple of weeks, to ensure the proper formation of the superconducting phase. It is worth noticing the range of endurance of the coils: from the formation process to real operation (in superfluid helium), they are able to withstand a temperature range of about 1000° C.

The last stage is the vacuum impregnation. Epoxy resin CTD 101 K is used to impregnate  $Nb_3Sn$  coils. This material has a low viscosity, similar to that of water, and can filter through the interstices left in between the two layers, between cables, and even strands. Epoxy has also an excellent performance at cryogenic temperatures and a very high radiation resistance. Coils are impregnated with a mold temperature of  $60^\circ C$ . The tray on which the mold is placed, is lifted-up at 12 degrees to give a slope to the mold. In this process, quench heaters are also impregnated on the outer layer of the coil. In the end, the coil appears with a black color, given by the hydrocarbons in the epoxy that have been burnt during the impregnation.

This is how the final coil looks like (Fig.2.23) from the outside.



Figure 2.23: The final coil. The two layers can still be distinguished, but they turned black, due to the impregnation stage.

And Fig.2.24 shows a cross-section of the dipole of the 11 T.



Figure 2.24: Cross-section of a Dipole coil for the 11 T project.

### 2.9 Comparison with NbTi cables

It is relevant to point out the differences between cables for the present LHC machine and cables for the High-luminosity project. To begin with, NbTi cables are much simpler to manufacture. All the cables for the present LHC were wound using the same machine, previously seen in Fig.2.20. Cables were made of 36 strands instead of 40, and no stainless-steel core was needed. A scotch-type material, named Kapton®, and wrapped all around the cable, was used to provide electrical insulation.

Helium, the liquid coolant, could filter in every small interstice in the system, both between cables, and even inside them, thanks to its superfluid state, characterized by zero viscosity. Very thin channels were also derived in the Kapton insulation, so that helium could provide an even more efficient cooling. A review of the state-of-the-art about the heat exchange mechanisms involving helium and NbTi cables will be presented in next chapter.

On the other hand, the presence of epoxy resin in  $Nb_3Sn$  cables prevents helium from filtering inside the coil pack, thus changing completely the heat exchange mechanism.

The last step in the manufacturing process was coil winding, after which the coil was already completed: this makes one realize how the entire process was much simpler. The cause is attributable to the nature of the two materials. NbTi is, in fact, a metallic alloy, thus having all the properties of a metal, as ductility and workability. Nb<sub>3</sub>Sn, on the contrary, shows a completely different behavior, being an intermetallic compound and thus having a crystalline structure. This makes it very fragile, which calls for the Wind-and-React technique, together with the impregnation process, which is put in place to prevent strands from moving (strain acts to strongly reduce the critical parameters).

Despite its very good mechanical properties, NbTi has the disadvantage of the low values of the upper critical field and critical temperature. It is to be used only in liquid helium and to produce fields below 10 T. To go at least higher with fields, another material was to be chosen, which is Nb<sub>3</sub>Sn. As it has been pointed out, it brings difficulties with it, due to its worse mechanical properties. Nevertheless, thanks to this new project, the material is beginning to be known better and better, and its superconducting properties will allow to push magnetic fields and thus accelerator energies up to the 16-20 T range during the next decades.

### 3. Heat exchange properties of Helium in Nb-Ti superconducting cables

#### 3.1 Heat loads during machine operation

Heat loads are a major reason of concern for the operation of superconducting magnets of the LHC and are mainly driven by two mechanisms: AC losses and beam losses.

AC losses are induced during the ramp-up stage of the magnetic field, which is gradually increased all over the 1232 dipoles of the machine to allow the parallel increase in beam energy (let's remind that the LHC is a synchrotron accelerator). A varying magnetic field over time,  $dB/dt$ , induces AC losses due to the simultaneous presence of both current and electric fields in the superconducting material. This can be shown in the simplified case of an infinite slab [5], and even in tapes [6]. A second source of heating comes from steady-state operation, and it is given by beam losses, which release energy into the magnets mainly through secondary showers of particles. A beam screen is used at the present day to limit the energy that hits the magnets. The screen is placed directly inside the beam pipe and it is covered on its inner surface by a few millimeters of tungsten (W), an element which is capable to absorb a high percentage of the energy of colliding particles. Despite the presence of the beam screen, still a 50% of the energy reaches the magnet, thus making it crucial to determine coil behavior under heat loads. Losses are dangerous, in general, since they could trigger a quench, the subject of next section.

#### 3.2 The quench phenomenon

A superconducting coil under operation is immersed in a bath of superfluid helium, in order to keep the temperature at the values required to maximize the magnetic fields. Helium inside the system continuously exchanges heat with a second line of "fresh" helium at 1.8 K, so that heat leaks through the non-ideal insulation and synchrotron radiation can be counterbalanced, as properly considered from the design project.

Nevertheless, unforeseen heat sources can release additional heat in the coils. These are attributable to various phenomena, such as slips between strands or cracks in the epoxy resin, which can result in a temperature increase of a localized region. If the region transits to the normal state, the extremely high current flowing through it generates an enormous amount of heat by Joule effect, much bigger than the initial source. Depending on the cooling mechanism, the conductor can restore its initial condition by a process called *recovery*, or further increase its temperature, causing a *quench*.

Quench is a very fast phenomenon, which acts in the  $10^{-4} - 10^{-1}$  seconds range, due to the ability of the normal zone to propagate at high velocities, reaching in few moments even the farthest parts of the magnet and causing a rise in the resistance of the entire coil.

Before going on, it is worth to point out that superconducting coils are always made of composite strands, where the superconductor is even less than half of the total material. This is done for stability reasons, since it can be shown [5] that quench energy is 4 orders of magnitude bigger using a composite than a pure superconducting material. Reliability is, in fact, one of the most critical technological problems for superconducting magnets, and it is directly linked with stability and quench.

For these reasons, an external protection system is designed to measure the increase in the resistance of the coil. When a threshold value is overtaken, the magnet supply system is immediately switched off, and the energy stored in the magnet is dumped by means of an external resistance (an RL circuit dumper). This prevents from converting all the magnetic energy stored in the coil in heat inside the coil itself, by Joule heating. Nevertheless, caution should be adopted with this kind of dumpers, since a rapid de-energization could be the cause of electric arcs. In fact, the combination of a high inductance and discharge rates produces a very high voltage,  $v_L = L di/dt$  which can break the insulation. To avoid arcs, accelerator magnets are instrumented with inductive heaters to heat up the entire magnet. Despite having 400-500 K localized, which would cause a permanent damage of the magnet, making it unusable, heaters warm up the magnet uniformly to 100-150 K, safeguarding its life.

A relevant concept in magnet operation is quench training: when a magnet is tested for the first time, the current at which quench is reached is just 30% of the critical current. The "quench current" slightly improves with the number of tests, until an almost steady value between 80 and 90% of the critical current is reached. This happens both for Nb-Ti and Nb<sub>3</sub>Sn, and the enhancement is due to settlement of the magnet in time. In fact, all the weak zones break during the first tests, so that a general reinforcement takes place with loads and



The first three components are thermally coupled and, in addition, heat exchange between the cable insulation and the external bath and between the *He* fraction in the cable and the external bath is allowed. This thermal network is described by a system of ordinary differential equations based on local balance of energy, as reported in [7]

$$\begin{cases} A_s \rho_s C_s \frac{\partial T_s}{\partial t} = q'_{ext} + q'_{Joule} - p_{s,h} h_{s,h} (T_s - T_h) - p_{s,i} h_{s,i} (T_s - T_i) \\ A_h \rho_h C_h \frac{\partial T_h}{\partial t} = p_{s,h} h_{s,h} (T_s - T_h) - p_{i,h} h_{i,h} (T_i - T_h) - (p_{i,h} + p_{s,i}) Q_{HeII} \\ A_i \rho_i C_i \frac{\partial T_i}{\partial t} = -p_{i,h} h_{i,h} (T_i - T_h) - p_{s,i} h_{s,i} (T_i - T_s) - p_{i,b} h_{i,b} (T_i - T_b) , \end{cases} \quad (3.1)$$

where *s* refers to the strands, *h* to the *He* fraction in the cable, *i* to the insulation, and *b* to the external bath. These equations are used to solve the heat balance problem, while they do not allow to solve the heat conduction equation in a solid. The third paragraph of the paper is entirely devoted to the description of the heat transfer coefficient between *He* and the strands,  $h_{s,h}$ , while for the other coefficients the following expressions are used

$$\begin{cases} h_{s,i} = \frac{h_s h_i}{h_s + h_i} \\ h_{i,h} = \frac{h_i h_{s,h}}{h_i + h_{s,h}} \\ h_{i,b} = \frac{h_i h_b}{h_i + h_b} , \end{cases} \quad (3.2)$$

Where empirical definitions  $h_i = 2k_i/t_i$  and  $h_s = 1/R_c = 1000 \text{ W/m}^2\text{K}$  define the thermal contact of insulation and strands.  $k_i$  is the thermal conductivity of the insulation and  $t_i$  is its thickness.  $1/h_b$  is the Kapitza resistance between the insulation and the external bath. The relations above express a series between thermal resistances, which take the form of a parallel system when using the heat transfer coefficient (let's remind that  $R = 1/h$ ).

The term  $Q_{HeII}$  allows taking into account thermal coupling between the *He* inside the cable and the external bath through the complicated *He* channels network between the insulation layers and through the insulation porosity. The heat flux in the Gorter-Mellink regime,  $Q_{HeII}$ , is modeled defining an equivalent channel in terms of heat transport properties and assuming that *He II* heat transfer in the channels and conduction in the insulation are independent [16]

$$Q_{HeII} = \frac{1}{A_t} \left( \frac{A}{L^3} \right) \left[ \int_{T_b}^{T_h} f(T) dT \right]^{\frac{1}{3}} \quad (3.3)$$

Where the cross-section *A* and the length *L* of the equivalent channel mentioned above define the geometrical group;  $A_t$  is the heat transfer surface and  $f(T)$  is the thermal conductivity of the superfluid.

### 3.4 Heat transfer to helium

Heat exchange between *He* and a superconducting strand is described through a number of heat transfer coefficients, which differ due to the various phases that *He* undergoes during magnet operation. The explanation of the various coefficients follows.

#### 3.4.1 $h_K$ (Kapitza)

Below the lambda point ( $T_\lambda = 2.172$  K,  $p = 0.5$  bar), defined on the phase diagram for He [8] shown in Fig.3.3, the *He II* region (*He II* is also called *superfluid* helium) can be identified.

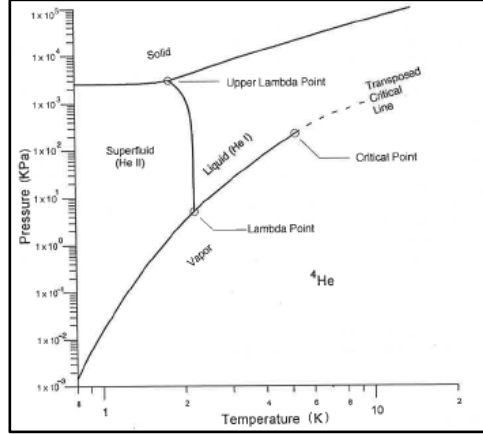


Figure 3.3: Pressure vs Temperature diagram for helium.

Heat exchange with *He II* is limited by the Kapitza resistance at the interface between the *He* and the strands. Thermal boundary conductance occurring at the interface between a solid and liquid *He II* was first discovered by Kapitza in 1941, during an experiment to study the flow of heat around a copper block immersed in the liquid [9].

For times in the microsecond range, after the local conductor temperature begins to rise, the heat transfer is limited by the Kapitza value,  $h_K$  [21]. This is primarily a function of the heated surface properties and not of the *He* properties. Its magnitude depends strongly on surface finish, phonon density, etcetera. However, since it is an important heat transfer mechanism only for such short times, the results have little sensitivity to errors in its assumed value, and the same formula given below, is used.

The Kapitza heat transfer coefficient,  $h_K$  is defined as [8,9]

$$h_K = \lim_{\Delta T \rightarrow 0} \left( \frac{q}{\Delta T} \right), \quad (3.4)$$

where  $\Delta T = T_s - T_{He}$ .  $T_s$  is the temperature of the surface in contact with *He II* and  $T_{He}$  is the *He II* temperature (1.9 K in the present case). For practical purposes, an easier definition is used

$$h_K = \left( \frac{q}{\Delta T} \right). \quad (3.5)$$

Theories that try to explain the phenomenon of Kapitza conductance use the same heat transfer law [10, 21]

$$q = \chi_K (T_s^4 - T_{He}^4), \quad (3.6)$$

which is similar to the radiation heat transfer between two parallel infinite surfaces, and can also be re-written as

$$q = \chi_K (T_s^2 - T_{He}^2)(T_s^2 + T_{He}^2) = \chi_K (T_s - T_{He})(T_s + T_{He})(T_s^2 + T_{He}^2), \quad (3.7)$$

where  $\chi_K$  is the Kapitza coefficient. When  $\Delta T \ll T_{He}$  it means that  $T_s \approx T_{He}$  and the equation can be simplified as

$$q \cong 4\chi_K T_{He}^3 (T_s - T_{He}) \cong h_K (T_s - T_{He}) . \quad (3.8)$$

So  $h_K \cong 4\chi_K T_{He}^3$  or, more precisely, from the expression above

$$h_K = \chi_K (T_s + T_{He}) (T_s^2 + T_{He}^2) , \quad (3.9)$$

where  $\chi_K$ , or  $\sigma$ , depends on the nature and surface state of the strands and is taken equal to  $200 \text{ W/m}^2\text{K}^4$  [10, 24]. Deepening the study in the literature, it can be found that  $\sigma$  has a certain variability, and it depends strongly on the surface in contact with helium. In the case of OFCH (Oxygen Free High Thermal Conductivity) copper covered by a thin layer (14  $\mu\text{m}$ ) of PVF (Poly-Vinyl-Fluoride) the expression is modified [24]

$$q \cong h_K (T_s - T_{He}) , \quad (3.10)$$

where  $h_K$  is equal to  $710 \text{ W/m}^2\text{K}$  and the exponent of the temperatures,  $n$ , is brought to 1. Values of Kapitza conductance are often experimentally determined, since theories fail to predict them. Furthermore, the Kapitza conductance is a function of different parameters linked to the material itself, its roughness and shape [9].

Values for bare copper are typically

$$\begin{cases} h_k \approx 900 T^3 & \text{for clean surfaces} \\ h_k \approx 400 T^3 & \text{for dirty surfaces} . \end{cases} \quad (3.11)$$

To have a numerical evaluation, by applying the formula above for a dirty and a clean surface at 2 K, 3200 and  $7200 \text{ W/m}^2\text{K}$  are respectively obtained, while at  $T_s = 2.0 \text{ K}$  and  $T_{He} = 1.9 \text{ K}$ ,  $h = 5936 \text{ W/m}^2\text{K}$ , which is almost in the middle of these two values.

### 3.4.2 $h_{BL}$ (Boundary layer)

When all the *He* surrounding the strands reaches  $T_\lambda$ , the *He I* phase starts and temperature gradients are established in the *He* bulk. Under a sustained heating, the boundary between the *He I* and *He II*, the so-called  $\lambda$ -front, starts propagating, while the *He I* phase grows. At this point a thermal boundary layer forms at the interface between the *He* and the strands [10]. The definition of the heat transfer coefficient [11] is

$$h = \frac{\phi_{He}}{A(T - T_{bulk})} , \quad (3.12)$$

where  $A$  is the wetted area inside the tube and  $T_{bulk}$  is the bulk temperature of the fluid before the heat pulse is released ( $t < 0$ ).  $T$  is the copper wall temperature, and  $\phi_{He}$  is the heat power released to *He*.

Since the whole heat transfer phenomena did not change much when varying the heat flux, pressure and mass flow [11], the idea stands that the heat transfer takes place in a thin layer of stagnant helium along the wall of the conduit. If the heat penetration is small enough, the results can be compared with the solutions in the case of heat transfer from a flat plate to a semi-infinite medium. The analytical solution for a fixed heat flux per unit area,  $\phi/A$ , starting at  $t = 0$  is

$$T(y, t) - T_b = \frac{2\phi}{\lambda} \left\{ \left( \frac{\alpha t}{\pi} \right)^{\frac{1}{2}} e^{-\frac{y^2}{4\alpha t}} - \frac{y}{2} \operatorname{erfc} \left[ \frac{y}{(\alpha t)^{\frac{1}{2}}} \right] \right\} , \quad (3.13)$$

where  $T_b$  is the bulk temperature at  $t = 0$ ,  $y$  is the distance from the wall and  $\alpha$  is the thermal diffusivity of helium,  $\alpha = \lambda/(\rho c_p)$ . A penetration depth  $\delta_T$ , determined by the thermal diffusivity, can be defined

$$\frac{T_b - T(0, t)}{\delta_T} = \left. \frac{d(T(y, t) - T_b)}{dy} \right|_{y=0}. \quad (3.14)$$

In the constant flux model  $\delta_T$  is given by:  $\delta_T = (4\alpha t/\pi)^{1/2}$ . The expected temperature penetration in the millisecond time scale is in the order of the tens of micrometers.

From the results it can be concluded that the transient heat transfer takes place in a thin helium layer along the wall of the conduit. This model will hold for short times, when the heat transfer mechanism is heat conduction [11]. From the previous expression of the heat transfer coefficient and from the analytical expression of  $\Delta T$ , for  $t = 0$ ,  $\Delta T = T(0, t) - T_b$ .

It can be derived that

$$h_{BL} = \frac{1}{2} \sqrt{\frac{\pi \lambda \rho c_p}{t}}, \quad h_{BL} \propto \frac{1}{\sqrt{t}}, \quad (3.15)$$

where  $\varepsilon = \lambda \rho c_p$  is a kind of volumetric heat absorption coefficient. After the boundary layer is fully developed, the heat transfer mechanism is driven by a steady state heat transfer coefficient,  $h_{SS}$ . For slightly larger times, normally  $10^{-4}$  to  $10^{-2}$  seconds, thermal diffusion into a laminar boundary layer of warm helium is the dominant impedance to heat transfer. For a constant conductor temperature and fluid properties, the classical expression for the transient heat transfer coefficient, at times  $t$  after the start of the heat pulse is given by  $h_{BL}$ . However, when the wall temperature changes with time,  $h_{BL}$  depends in addition upon the previous wall temperature profile  $T_w(t')$  for  $t' < t$ .

The boundary layer is not relevant in the case of *He II*, for which only the Kapitza resistance matters. On the other hand, in *He I* there are both the layers, since Kapitza is present in any case. Heat transfer in solids is governed by the phonon mechanism inside the crystal of the solid itself, and when a contact between two solids is realized, or between a solid and a liquid, the change in crystal structure at the interface causes the temperature to drop. Macroscopic contact resistance is originated from this phonon interaction and also from the limited contact area between the surfaces of the materials, which occurs only in three or four points. However, for times longer than  $10^{-2}$  to  $10^{-1}$  seconds,  $h_{BL}$  becomes small and the steady-state heat transfer coefficient is obtained,  $h_{SS}$ .

### 3.4.3. $h_{SS}$ (Steady-state)

The transition to the steady state heat transfer in the boundary layer takes place when the temperature reaches the steady state, linear profile. Experiments carried out in supercritical helium [15] show an initial peak in the heat transfer followed by a drop with the inverse square root of time. The transient heating induces motion of the helium through the cable porosity, in all directions across the cable width and along the cable length. The motion is associated with a convection heat transfer that corresponds to a fully established thermal boundary layer [17]. It is assumed that  $h_{SS}$  may be evaluated from standard time-independent correlation for turbulent flow, even when flow changes rapidly in time. The local Nusselt number can deviate by almost an order of magnitude with respect to the value given by the steady state correlation that involves the local Reynolds number, when also  $Re$  changes rapidly in time [21]. In general, a Dittus-Boelter correlation is used, for large wall-to-bulk temperature differences, as it is possible to find again in [21]

$$\frac{D_h h_{SS}}{k} = Nu_{SS} = 0.023 Re^{0.8} Pr^{0.4} y, \quad (3.16)$$

where

$$\begin{cases} y = \frac{1 + 0.4z - (1 + 0.8z)^{0.5}}{0.08z^2} \\ z = \alpha \frac{T_w - T_h}{T_h} . \end{cases} \quad (3.17)$$

A similar approach could be found in [17], where the correlation is

$$h_{ss} = 0.0259 \frac{K_h}{D_h} Re^{0.8} Pr^{0.4} \left( \frac{T_{He}}{T_s} \right)^{0.716} , \quad (3.18)$$

and they both bring to similar results. These correlations are used to describe heat transfer in the interstitial flow in CICC and in [7] it is postulated that it should be valid also for the outflow in the porous structure of strands and insulation of a Nb-Ti accelerator cable.

The value given in [10] for  $h_{ss}$  is 50 W/m<sup>2</sup>K, based on evaluations on the channel dimension defined by the contact between two strands in a Nb-Ti Rutherford cable. One can try to reconstruct this value, substituting the proper values in expression (3.18)

$$K_h = 1.803 * 10^{-2} \frac{W}{m K} . \quad (3.19)$$

Fig.3.4 is useful to compute the hydraulic diameter

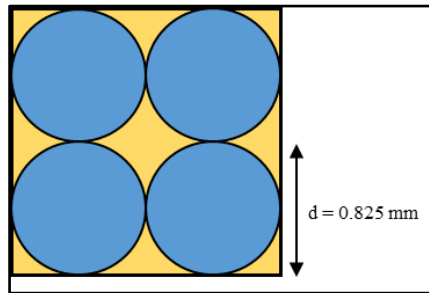


Figure 3.4: Image of a unit cell of a Rutherford cable. Diameter of Nb-Ti strands is 0.825 mm.

We consider the channel defined by the central space among the four strands. The hydraulic diameter is

$$D_h = \frac{4S}{P} = 4 * \left( \frac{1.65^2 - 4 * \frac{\pi * 0.825^2}{4}}{0.825 \pi} \right) * \frac{1}{4} = 0.225 \text{ mm} , \quad (3.20)$$

while the other quantities are computed in the following expressions

$$Re = \frac{\rho v D_h}{\mu} , \quad (3.21)$$

$$\rho = 137.9 \frac{kg}{m^3} , \quad (3.22)$$

$$\mu = 3.674 * 10^{-6} \text{ Pa} * \text{s} . \quad (3.23)$$

For  $v = 0.3 \text{ m/s}$

$$Re = 2533.5 , \quad (3.24)$$

which is the lower limit for the turbulent regime, and thus of eq.(2.18). The last quantity to be determined is

$$Pr = \frac{c_p \mu}{k} , \quad (3.25)$$

where

$$c_p = 3281 \frac{J}{kg K} .$$

The Prandtl number becomes

$$Pr = \frac{c_p \mu}{k} = 0.53 , \quad (3.26)$$

so that

$$h_{ss} = 0.0259 * \frac{K_h}{D_h} Re^{0.8} Pr^{0.4} \left( \frac{T_{He}}{T_s} \right)^{0.716} = 773.2 \frac{W}{m^2 K} . \quad (3.27)$$

The last expression is computed with values of  $T_{He} = 3.5 \text{ K}$  from [8], since it is in the middle range between 2.17 K, the lambda temperature, and  $T_s = 4.2 \text{ K}$ , the saturation temperature. Similar computations come up from eq.(3.16).

It appears from these computations that we were not able to reproduce the same value given in [7]. Further controls are then suggested from both sides, in order to get the proper value, since this so big difference could strongly affect simulation results.

The general synthesis between the above coefficients for  $h_{HeI}$  was not unique when [21] was written. Two different relations were presented

$$h_{HeI} = \max \left\{ \frac{h_k h_t}{h_k + h_t}; h_{ss} \right\} , \quad (3.28)$$

and

$$h_{HeI} = \frac{h_k h_t}{h_k + h_t} + h_{ss} . \quad (3.29)$$

The difference between the two expressions is quite significant when studying system response near stability limit. During the years, it has been established that the first expression is better in describing the real behavior of heat transfer for *He I*.

#### 3.4.4. $h_{HeI}$ (Helium I)

In [10] the first approach is followed

$$h_{HeI} = \max \left\{ \frac{h_K h_{BL}}{h_K + h_{BL}}; h_{ss} \right\} , \quad (3.30)$$

where the first term is a series between two thermal resistances, the Kapitza resistance and boundary layer resistance (let's remind that, in general,  $h = 1/R$ , per unit length). During the first moments, in the transient

regime, the first term is predominant, but as time passes, the regime turns to steady-state and the second term becomes more relevant.

Steward [10] deduced from his data that Kapitza resistance and the pure conduction resistance of the developing thermal boundary layer, added in series, dominate the heat transfer process in the early part of the transient; this would explain the reason of the expression (3.30). The phenomenon occurs before convective and boiling processes become established. At longer times the heat transfer coefficient tends towards the steady-state value during which convection or boiling dominate.

### 3.4.5 $h_{nucl.boil.}$ (Nucleate boiling)

Once the state of *He* reaches the critical line, heat transfer is governed by boiling. From [13], one can derive a rough estimate of the heat transfer coefficient for liquid helium (*He I*) by means of Fig.3.5.

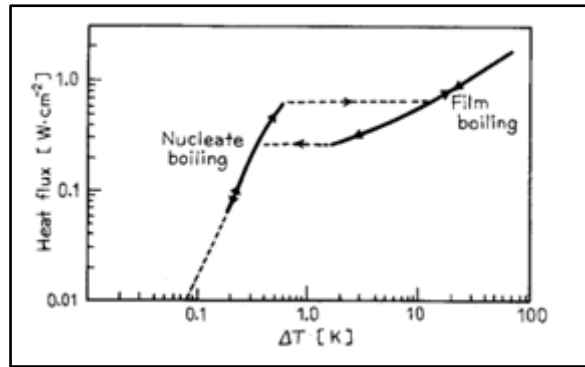


Figure 3.5: Nucleate boiling regime

As the peak heat flux in nucleate boiling is approximately  $6.0 \text{ kW/m}^2$  for at a  $\Delta T \cong 0.7 \text{ K}$ . The model in [14], assumes that the heat exchange process during transient nucleate boiling is mainly governed by the Kapitza thermal resistance, and can be described as

$$h_{nucl.boil.} = \frac{Q_K}{S_s^{wet}(T_s - T_{He})} = \frac{\beta(T_s^m - T_{He}^m)}{(T_s - T_{He})}, \quad (3.31)$$

where  $Q_K$  is the Kapitza thermal flux, the values used for  $\beta$  and  $m$  are:  $\beta = 242 \text{ W/m}^2\text{K}^m$  and  $m = 2.8$ . Using  $T_s = 6 \text{ K}$  and  $T_{He} = 4.2 \text{ K}$ , the formula gives:  $12'818 \text{ W/m}^2\text{K}$ .

Considerations made in [12] for the transient nucleate boiling regime are also reported. Fig. 3.6 shows temperature traces for step input heat pulses for a copper surface. The parameter is the heat flux.  $\Delta T$  remains constant until a “take-off” time,  $t_f$ , then rises sharply.

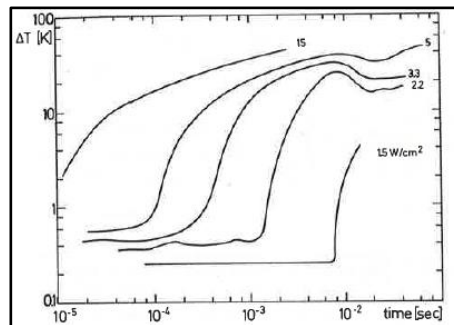


Figure 3.6: Transient heat transfer experiment using a monofilamentary Nb-Ti/Cu superconductor, both as a heat and a thermometer. The plot shows surface temperature traces for various heat fluxes  $Q$ . Credits: reference [12].

It is possible to explain this sudden temperature increase by the onset of film boiling (in the film boiling regime, a temperature overshoot is seen at about 10 ms, which is due to the onset of convection.

In the time range below 1 ms, convection does not play any role). The surface remains in the nucleate boiling regime for some time, even for heat fluxes well above the steady-state nucleate boiling maximum.

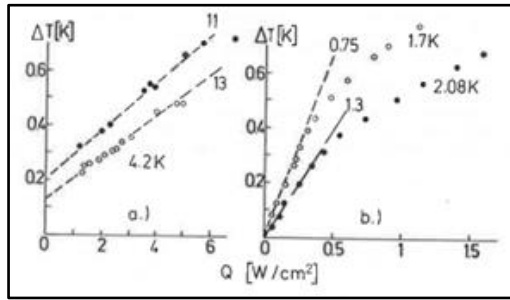


Figure 3.7: Nucleate boiling regime initiation.

Fig. 3.7(a) is a plot of the initial temperature, taken for times  $t \ll t_f$ , versus the heat flux. Data can be fitted with an expression such as

$$\Delta T = \Delta T_0 + \frac{Q}{h_K}. \quad (3.32)$$

The last term can be explained in terms of a Kapitza resistance, as previously explained, while the first term is a constant. The measured  $\Delta T_0$  values were between 0.13 and 0.25 K for different samples, and  $h_K$  was in the range of 10-15 W/cm<sup>2</sup>K. This is quite in agreement with other values found in the literature for the heat transfer coefficient during transients [23, 24]. In this last two references, values for the critical heat flux, of 35 kW/m<sup>2</sup>K at steady-state and of 100 kW/m<sup>2</sup> during transients, are given. It is to be underlined that these values are useful to get a sense of the orders of magnitudes involved in the heat exchange mechanism, although they are only a rough estimate of the real values.

Going back to [14], one can notice that temperature differences are quite small during nucleate boiling and precise measurement is rather difficult (note that the more is the heat removed from the surface, the less is the  $\Delta T$  between the surface and the liquid bulk). The identification of  $1/h_K$  as a Kapitza resistance is supported by the measurement of  $\Delta T(Q)$  below the lambda point (fig. 3.7b), where  $h_K$  is expected to have a  $T^3$  dependence (in accordance to what was said before).

In [15] a reference to previous important works [12] and [13] in determining the transient heat transfer properties of helium is presented, which resulting plot is shown in Fig.3.8.

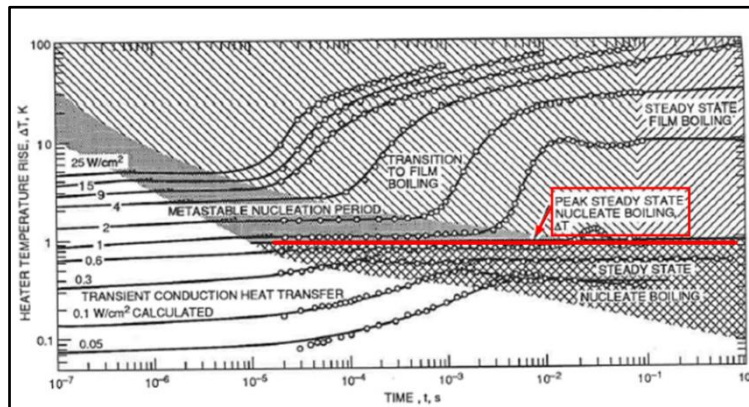


Figure 3.8: Steward's curves of transient heat transfer from a vertical surface to boiling liquid helium at atmospheric pressure.

Right at the start, the heater temperature rises suddenly by a few tenth of a Kelvin. This modest, early temperature rise corresponds to heat transfer limited by, as already mentioned, the Kapitza resistance. In this regime, the rate-determining heat transfer process is transient conduction through the heated layer of liquid helium adjacent to the heater surface. After a time, the heat being transferred to helium causes bubbles to appear, and the dominant mode becomes nucleate boiling.

For small heat fluxes the nucleate boiling may persist indefinitely, while for larger fluxes it ends with the transition to film boiling accompanied by a large increase in temperature. We will return on this matter a little farther.

### 3.4.6 $h_{film\ boil.}$ (Film boiling)

A relevant aspect of modeling is the assessment of the maximum heat flux at which the sudden drop of the heat exchange coefficient occurs, i.e., the transition from nucleate to film boiling. In fact, nucleate boiling could last indefinitely if the heat flux towards  $He$  does not exceed the critical heat flux or if the surface superheat does not exceed the threshold  $\Delta T^*$ . If one of these thresholds is overcome the nucleate boiling phase cannot evacuate anymore heat without starting a film boiling [10]. In the present case, this value is reduced to 0.4 K due to the movement of  $He$  in narrow channels.

The total energy flux transferred to  $He$  is linked to the onset time of film boiling through

$$E_{lim} = \alpha(t_{on} - t_0^*)^n , \quad (3.33)$$

where  $t_{on}$  is the onset time of film boiling,  $t_0^*$  is when  $T_s$  becomes equal to  $T_{sat} + \Delta T^*$ ,  $\alpha$  is a constant coefficient equal to  $720 \text{ J/m}^2\text{s}^n$  and  $n = 0.6$  [7] - [25]. After  $E_{lim}$  is reached the heat transfer coefficient drops to its film boiling value.

The onset of film boiling strongly depends on the heat flux,  $Q$  [12], see Fig.3.9.

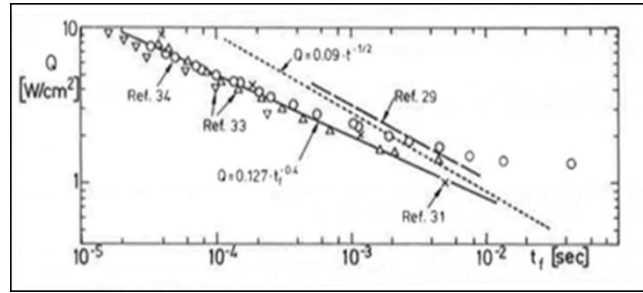


Figure 3.9: Correlation between "take-off" time (onset of film boiling) and heat flux,  $Q$ . The dotted line is given by theory, while the solid line was proposed to be used for numerical stability calculations. Credits: reference [12].

The near constancy of  $qt_f^{1/2}$  suggests the following elementary theory of transient heat transfer in saturated helium. According to ordinary diffusion theory, when the flux entering a half-space is suddenly clamped at a constant value  $q$ , the temperature rise  $\Delta T$  at the front face is given by [15]

$$\Delta T = (4q^2t/\pi kS)^{1/2} , \quad (3.34)$$

where  $t$  is the elapsed time, in [s], since the heater was energized,  $k$  is the thermal conductivity of helium in [W/m/K] and  $S$  is its volumetric heat capacity, in [J/m³K]. Heat introduced per unit area during the time  $t$  is  $qt$ . If heat is absorbed by a thin layer of thickness  $\delta$  in which the temperature rise is uniform at the value given in eq.(2.34), then  $S\Delta T\delta = qt$ , with dimensions [J/m²], so that

$$\delta = (\pi kt/4S)^{1/2} . \quad (3.35)$$

Schmidt postulates that take-off occurs when transmitted heat  $qt$  equals the latent heat  $L\delta$  of the heated layer, for a that time he supposes there is enough heat able to vaporize the entire heated layer

$$qt_f^{1/2} = (\pi k/4S)^{1/2}L \cong 39 \text{ mW/m}^2\text{s}^{-1/2} . \quad (3.36)$$

Let's suppose to have a short pulse of energy  $H$  [J/m²], in a time interval  $\Delta t$ , so that  $q = H/\Delta t$ . Since the product  $qt_f^{1/2}$  remains almost constant, substitution in the equation returns that  $H$  is proportional to the half

power of  $\Delta t$ ,  $\Delta t^{1/2}$ . On the other hand, Joule heating is proportional to  $\Delta t$ , and for this reason it is a satisfactory approximation to neglect the  $\Delta t$  for times short enough.

Finally, the take-off time does not seem to be sensitive to the surface condition, but it is only a function of liquid helium properties. With decreasing heat fluxes, the  $Q(t_f)$  curve approaches the steady-state nucleate boiling maximum value. Similar considerations could be found in [20]. The appropriate value for film boiling is given in Table 3.1, and it is extracted from [18].

Sample	$T_s$ (K)	$T_f$ (K)	$\Delta p$ (kPa)*	$h$ (kW/m <sup>2</sup> ·K)	Reference
Wire ( $d = 76 \mu\text{m}$ )	1.8	150	0.42	1.1	55
Wire ( $d = 25 \mu\text{m}$ )	1.8	150	0.56	2.2	
Flat rectangular plate (39 mm × 11 mm)	1.8	75	0.14	0.22	49
	1.8	75	0.28	0.3	
Flat surface ( $d = 13.7 \text{ mm}$ )	1.8	75	0.84	0.55	
	2.01	40	0.13	0.69	3
Horizontal cylinder ( $d = 14.6 \text{ mm}$ )	2.01	25	0.237	0.98	
	1.88	40	0.10	0.2	51
Wire ( $d = 200 \mu\text{m}$ )	2.14	40	0.10	0.2	
	2.05	150	0.14	0.66	52
Cylinder ( $d = 1.45 \text{ mm}$ )	1.78	80	0.06	0.22	53

\* 1 kPa = 7.5 torr = 70.3 cm He.

Table 3.1: Typical film boiling heat transfer coefficients. The interesting case for our purpose is highlighted.

Highlighted in Table 3.1 is the last row, which corresponds to a cylinder 1.45 mm in diameter. That is exactly the situation we are interested in, since the diameter is very similar to that of a strand. The same value is confirmed in [20] and [12] where the heat transfer coefficient for film boiling is stated to be in the range between 0.017 and 0.028 W/m<sup>2</sup>K.

### 3.4.7. $h_{gas}$ (Gaseous helium)

When the film thickness equals the channel width, the whole  $He$  in the channel is vaporized, namely for  $E_{gas} = E_{lat}$ . A further worsening of the heat transfer coefficient is observed, due to the transition to a totally gaseous phase. The value of 70 W/m<sup>2</sup>K for the heat transfer coefficient is given again in the paper by Schmidt [20], where he refers to a previous work [10]. Values of heat transfer coefficients for gases and liquids at room temperature and in various conditions are listed, as a comparison, in Table 3.2.

Conditions of heat transfer	W/(m <sup>2</sup> K)
Gases in free convection	5–37
Water in free convection	100–1200
Oil under free convection	50–350
Gas flow in tubes and between tubes	10–350
Water flowing in tubes	500–1200
Oil flowing in tubes	300–1700
Molten metals flowing in tubes	2000–45000
Water nucleate boiling	2000–45000
Water film boiling	100–300
Film-type condensation of water vapor	4000–17000
Drops-size condensation of water vapor	30000–140000
Condensation of organic liquids	500–2300

Table 3.2: Heat transfer coefficients for various substances at room temperature.

## 4. The Cryolab experiment

### 4.1 Recalls

The magnets for the high-luminosity project of the LHC will be the first accelerator magnets to rely on Nb<sub>3</sub>Sn. It is known that this material is very different from Nb-Ti, both for its superconducting and mechanical properties. When considering the superconducting properties, Nb-Ti has a critical temperature,  $T_c$ , of about 9 K and it is used to build magnets can generate magnetic fields under 10 T. Nb<sub>3</sub>Sn, on the other hand, allows to go higher with fields, being appropriate for the production in the range of 10-21 T. The problem with Nb<sub>3</sub>Sn is that, once formed, it becomes fragile and sensitive to deformation, so it is much more difficult to handle with respect to Nb-Ti, and this has limited, until now, its use for applications.

In the upgrade project of the LHC, luminosity is planned to be increased approximately by a factor ten with respect to its present value. This will be achieved by substituting both dipoles and quadrupoles magnets. From one side, few Nb-Ti dipoles will be replaced with shorter-11 T elements that will enable to insert a higher number of collimator magnets; from the other side, quadrupoles close to the interaction region will be used to further focus the beams. In the operation scenario, proton bunches will be focused much more than they are in present machine, and this means, in turn, that higher magnetic field gradients are requested. The higher field gradients will result in peak fields on the conductor in the 11.5-12 T range, which as it has just been said, are out of the range of use of Nb-Ti.

All the present superconducting magnets for the LHC machine, not only dipoles and quadrupoles, are wound with Nb-Ti conductors, with a maximum magnetic field of 8.4 T on the conductors themselves (at 14 TeV energy of the proton beams). Nevertheless, fields up to 12 T are needed to ensure the high values of luminosity of the new project, so that a new material must be considered for the magnets, Nb<sub>3</sub>Sn.

Due to its fragility, Rutherford cables made with 40 strands of this intermetallic compound, have to be impregnated with epoxy-resin to limit deformations induced by strands movements during normal operation. Impregnation makes a substantial difference when one compares the behavior of Nb-Ti and Nb<sub>3</sub>Sn coils; helium is not able to fill the small interstices between strands as described in [7], and the magnet can exchange heat only through an inner annular channel of 1.5 mm thickness at the coil inner radius. In principle, helium is not able to penetrate inside the impregnation of the cables, except for small cracks that may originate upon cool-down due to thermal shrinkage differentials.

For these reasons, the thermal behavior is quite different from Nb-Ti, and it is interesting and important to assess how a magnet responds when subject to a heat load. Heat loads can be induced by various processes, like beam losses, AC losses during current ramps, and so on.

### 4.2 The experiment

The recalls present the framework of the Cryolab experiment, which is the subject of the present chapter. The experiment was carried out during the last months by Mário David Grosso Xavier at the cryogenics laboratory at CERN (Cryolab), under the supervision of Robert Van Weelderen [37].

The dipole coils used to bend particles and keep them on track inside the beam pipe, are designed in order to reproduce a  $\cos \theta$  current distribution. Consequently, the current density is not the same in every part of the cross-section, being maximum on the magnet middle plane ( $\theta = 0^\circ$ ) and zero at  $90^\circ$ . Various options have been explored in other accelerators, but LHC magnets have been the first to have such a high number of blocks (6 on a quarter of the cross-section). This same configuration is adopted also for the 11 T upgrade, and it is shown in Fig.4.1.

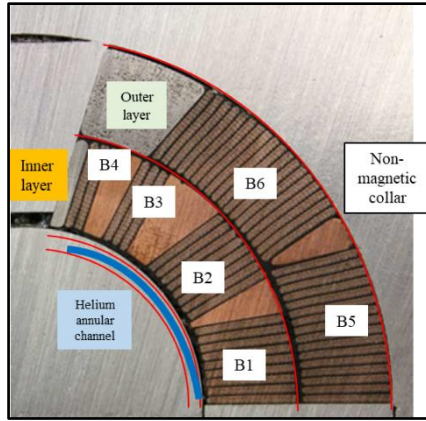


Figure 4.1: Nomenclature of the parts inside the magnet coil. Starting from the inner radius, we find: 1) Annular channel for helium; 2) Inner layer; 3) Outer layer; 4) Non-magnetic collar.

First, an annular channel of 1.5 mm thickness is placed on the very inner side of the magnet, where  $He$  is in direct contact with the conductor insulation of the inner layer, allowing to keep the temperature of the magnet at 1.9 K. Next, we encounter the inner and outer layer, their names coming from the radial distance from the center of the beam pipe. Coils are finally enclosed in a non-magnetic collar made of stainless steel, which acts to keep every part in position thanks to its pre-compression.

In the experiment, a quarter of a coil of the 11 T magnet, being 280 mm in length, was cut in order to derive a sample made of 9 cables in the inner layer, plus the copper wedge, and 16 cables in the outer layer (blocks 1 and 5 in Fig.4.1), for a total length of 140 mm. Both the original and final samples are depicted in Fig.4.2.

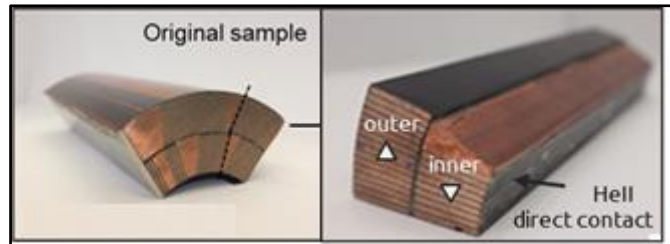


Figure 4.2: Original and final sample for the Cryolab experiment

In order to reproduce this configuration, and to be closer as possible to real operation, the sample was inserted into an open box of insulation material, which is G10 (impregnated fiber-glass, CTD 101K + S2). The only surface directly exposed to the  $He$  bath was the inner one, shown on the right in Fig.4.2, so that the other three were touching the insulation and could be considered, in a first approximation, as adiabatic. The final set-up is shown in Fig.4.3.

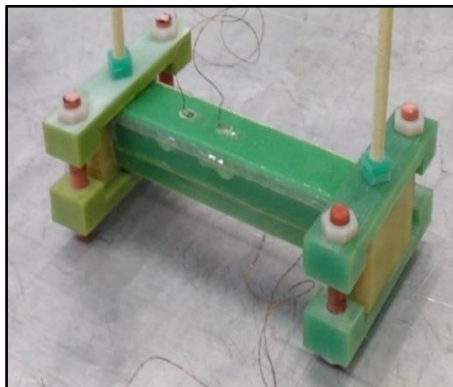


Figure 4.3: The insulation box, where the sample was inserted. Three sides can be considered adiabatic, while one was in contact with helium.

The box was then put inside a pot of superfluid helium, with its face pointing downwards. The length of the inner face effectively exposed to helium was 125 mm, less than the 140 mm of the sample. This was due to the extremities of the sample, which were clamped over a short length inside the left and right fixtures, represented in dark yellow in Fig.4.3.

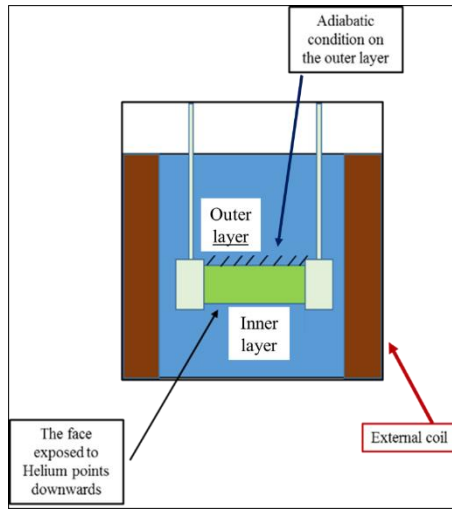


Fig. 4.4: The pot of superfluid helium. The external superconducting coil is represented in brown.

To complete the presentation of the experimental configuration, it can be pointed out that the sample was put inside a pot, filled with superfluid helium (below the lambda temperature,  $T_\lambda$ ) and pressurized at 30 mbar over the ambient pressure. The pot was surrounded by a second and bigger pot of saturated liquid helium, where a superconducting solenoidal magnet was immersed. A solenoid produces a field oriented along its axis, which is supposed to be homogeneous inside its volume. A simplified scheme of this description is shown in Fig.4.4. The entire apparatus is in Fig.4.5.

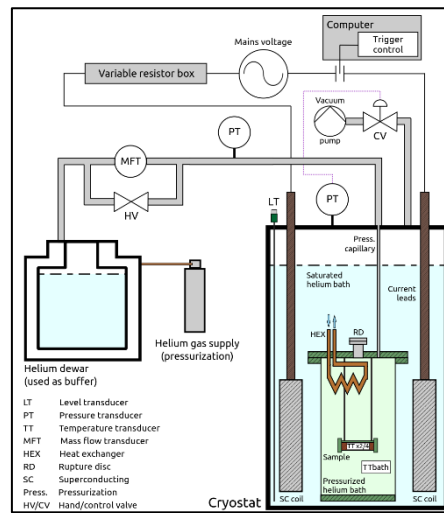


Figure 4.5: Schematics of the entire experimental apparatus.

The external pot was also used to provide the inner with a thermal shield, in order to make simpler to keep the low temperatures in the superfluid bath. This type of configuration is often used in similar kind of experiments [8]. The external bath allowed the operation of the external superconducting coil, used to induce AC losses in the sample, in order to heat it up.

Generally speaking, AC losses are induced by the variation of a magnetic field over time, namely  $dB/dt$ . There are basically two ways to change the level of the induced AC losses: 1) changing the frequency  $f$ , of the

magnetic field applied by the external magnet or, 2) changing the intensity of the upper and lower values of the external magnetic field,  $\pm B_0$ . In the Cryolab experiment, the external solenoid was supplied directly from the grid, and no frequency variator was used, so that it remained always equal to 50 Hz. To induce different levels of losses in the sample, the amplitude of the external field swing was changed. This was realized varying the current intensity that flowed in the external superconducting magnet. Table 4.1 shows some details of the operation of such a magnet. Increasing the resistance which was in series with the solenoid, allowed to decrease the current flowing in the solenoid itself and with that, the magnetic field and its change rate.

Resistance	Impedance (0.5 H, 50 Hz)	Maximum current	Maximum magnetic field	Maximum magnetic field change rate
$\Omega$	$\Omega$	A	mT	$T s^{-1}$
0	157	2.07	10.3	3.25
50	165	1.97	9.8	3.09
83	178	1.83	9.1	2.87
125	201	1.62	8.1	2.54
175	235	1.38	6.9	2.17
250	295	1.10	5.5	1.73
300	339	0.96	4.8	1.51
375	407	0.80	4.0	1.26

**Table 3.2.** The utilised resistances and the resulting impedances of the sample heating system. The maximum current in the magnet as well as the calculated magnetic field are listed in additional columns.

*Table 4.1: Values of R, I, B, and dB/dt characterising the external magnet operation. Credits: [47].*

Table 4.1 reports operation data for tests carried out at 230 V. Other tests were conducted at 400 V, and further numerical details can be found in [37].

There is another aspect about the sample which needs to be clarified, namely its orientation. Let's start looking at Fig.4.6.

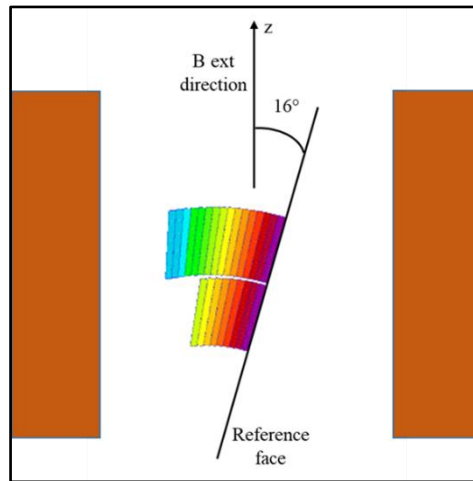


*Figure 4.6: Sample orientation relatively to the external field direction. Colours represent the amount of heat generated by AC losses.*

As previously mentioned, the coil sample was put inside the G10 box with its outer side touching the insulation, and the inner one facing helium and pointing downwards.

The orientation of the various cables with respect to the external field is a very important parameter to be known. The amount of AC losses strongly depends, in fact, on the angle between the two, and it is therefore necessary to define a reference surface. This surface lays on the so-called middle plane of the magnet. As Fig.4.6 depicts, the angle is  $16^\circ$ , while the angles formed with the other cables in the sample are immediately known, so that the losses can be computed. The color scale represents the amount of dissipation in the various layers. We should return on this later on.

### 4.3 A brief outline about AC losses

There are different types of AC losses generated inside a magnet, caused by currents at different scales: ISCC, IFCC, and Persistent currents. Inter-strand coupling currents, ISCC, flow among strands in a cable, and are dictated by the adjacent and crossing strand resistances. Typical values are

$$R_a = 0.3 - 3 \mu\Omega$$

$$R_c = 30 - 300 \mu\Omega$$

Inter-filament coupling currents, IFCC, flow among filaments which are inside a single strand of a cable, while persistent currents flow inside filaments themselves, due to the shielding effect in response to an external variation of a magnetic field. As their name suggests, they cannot be canceled once they begin to flow, and the only way to limit them is to produce filaments as thinner as possible.

AC losses, as the word itself suggests, are losses which deposit energy in the coil sample, thus resulting in a temperature rise in the various parts of the sample itself. To give an estimate of the energy deposition by induction, a calibration with a Joule heater was used, where heat was injected in the system simply through a Joule heater. The explanation of this calibration procedure follows.

### 4.4 The calibration procedure

The calibration consists of two sets of measurements. In each set two measures are performed, the first conducted on the pot alone (full of helium), and the second on the pot together with the sample immersed in the helium. Temperatures are measured by means of sensors that are directly instrumented in the sample and in the pot.

Starting from the first set, a certain value of  $dB/dt$  is applied on the pot alone and when steady-state is reached, a temperature increase,  $\Delta T_{p,1}$ , is measured. It is to be noted, in fact, that, even without the sample inside the pot, some metallic parts are present in the system. These are subject to AC losses when a changing magnetic field is applied, so that a small heating is produced. The sample is inserted in the pot, and a second temperature increase,  $\Delta T_{p+s,1}$  is registered. It can be stated that  $\Delta T_1 = \Delta T_{p+s,1} - \Delta T_{p,1}$  is the contribution given only by the AC losses generated in the sample itself. The procedure is outline in Fig.4.7.

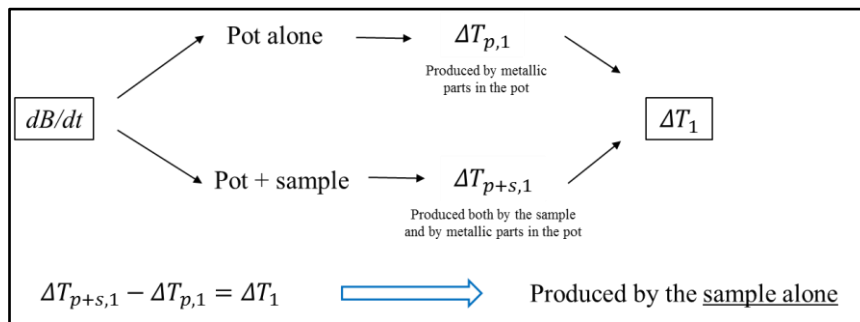


Figure 4.7: First set of measurements for the calibration procedure, involving the external solenoid.

The second set is conducted in a very similar way, while this time heating is produced by the Joule heater, located inside the pot. Fig.4.8 shows a very simple idea of how the heater is instrumented.

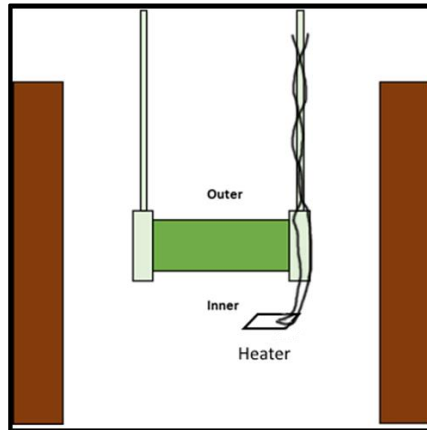


Figure 4.8: Joule heater instrumentation

To be more specific, its wires are quite thick and taped to the sample holder, ensuring that the heater remains in place and with its face (where the heating comes from) pointed at the sample, as Fig.4.9 depicts.

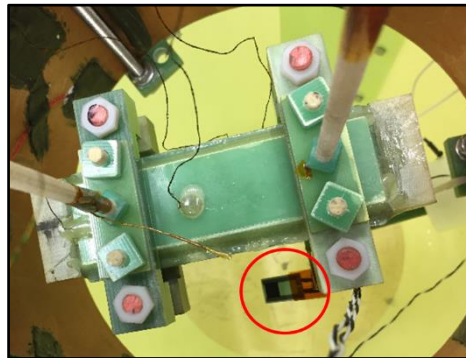


Figure 4.9: Top-view of the experimental set-up. The Joule heater is circled in red.

As before,  $\Delta T_2 = \Delta T_{p+s,2} - \Delta T_{p,2}$  is the contribution given by the sample alone. Fig.4.10 resumes the approach.

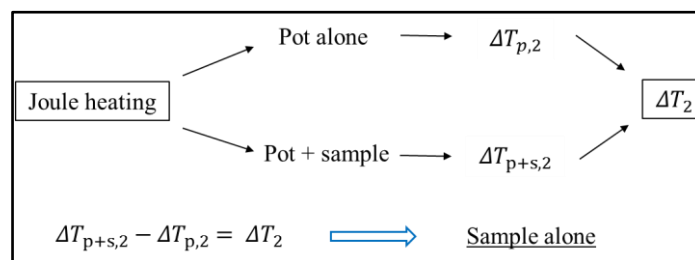


Figure 4.10: Second set of measurements, this time involving the Joule heater

The reason why the calibration procedure is carried out using a Joule heater is that, being basically a resistance, both the current and the applied voltage are perfectly known, and the input power, with them. Through a comparison of the temperature increases of the two different cases, one can establish an equivalence between the inductive and the Joule heating methods, thus assigning a total input power for a certain temperature increase measured in the inductive case.

$$\Delta T_1 \leftrightarrow \Delta T_2 \quad \Rightarrow \quad \frac{dB}{dt} \leftrightarrow Q \quad (4.1)$$

The expression in eq.(4.1) resumes the idea that through the equivalence between the temperature rises, one can establish an equivalence between the magnetic field variation and the Joule heating. It is important to notice that the heating by AC losses is generated inside the sample, while the resistive heater heats the sample from the outside. At steady-state, the heating produced in the superfluid helium by the sample because of the AC losses and by the Joule heater from the outside are the same, given a same temperature increase in the sample. This is the reason why the equivalence expressed in Fig.4.11 can be established.

Finally, it is to be said that, rather than dealing with temperature increases, one should think about the power inserted in the sample, both by induction and joule heating. It is power, and energy along with it, which causes a temperature increase. The equivalence should be, in principle, established using powers, not due to energy conservation. The difference is subtle, but it is still rather important from an energetic point of view. Nevertheless, considering temperatures will still not bring us to commit mistakes.

A vast campaign of measurements has been conducted, in a temperature range for the helium bath between 1.8 and 2.1 K (let's remind that the lambda temperature is 2.17 K) and for input powers spanning from 17 to 392 *mW*, referring to the total power coupled with the sample. The AC losses, which depend on the orientation of the cables in the external magnetic field, are not uniformly distributed in the sample. As a first approach to the problem, however, it will be considered that they are uniformly generated in the cable volumes of the sample. From calculations that will be better specified later, the volume by which the total heat will be divided for, is 59.10 *cm*<sup>3</sup> so that the input power density spans from 0.288 to 6.631 *mW/cm*<sup>3</sup>.

#### 4.5 Temperature measurements and sensors mounting

The calibration procedure is based on temperature measurements, extracted from the inside of the sample and from the helium bath. The present paragraph is dedicated to its description.

There are four temperature sensors mounted in the sample, two in correspondence with the inner layer, and two with the outer layer. Each inner sensor is placed approximately on the same radial line as the corresponding outer sensor, so that the four sensors are organized in two pairs. This will be an important factor in the comparison with simulation results.

The word “approximately” finds its reasoning in the fact that the sensors are not just drilled inside the sample in the radial direction, but they are instrumented following the direction of a strand. In order for the sensors to fit inside the coil, the coil itself has to be machined. Since the coil has already gone through the fabrication and impregnation processes, a first hole needs to be cut into the insulation before the cable can be machined. All in all the cut should be big enough so that the strand can be cut using a cnc machine with a head approximately of 1 mm. These holes are very thin, as Fig.4.11 shows.

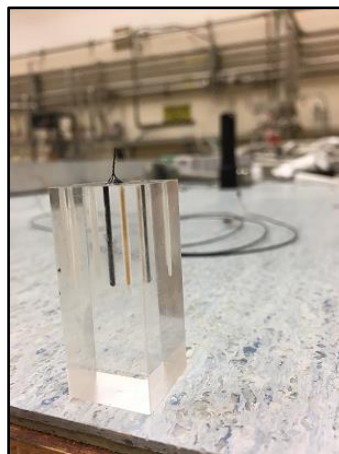


Figure 4.11: A few holes have been drilled in a transparent composite, to show how small the diameter is.

Care is adopted in order to drill just a single strand, for about a 2 cm depth inside the coil, starting from its edge and following the strand ( $16^\circ$ ). The hole is then filled with epoxy, and the sensor is slowly inserted in the hole, letting epoxy come out. Once the sensor is placed in the hole, glue is added until the level is even with the surrounding cable. No glue should be above the cable level. Once the glue is dry, the sample is inserted in the insulation box.

The 2 cm depth inside the coil translates in 5.7 mm in the radial direction, since the strand twisting angle is  $16.5$  degrees. Fig. 4.12 and 4.13 help to visualize what has been said.

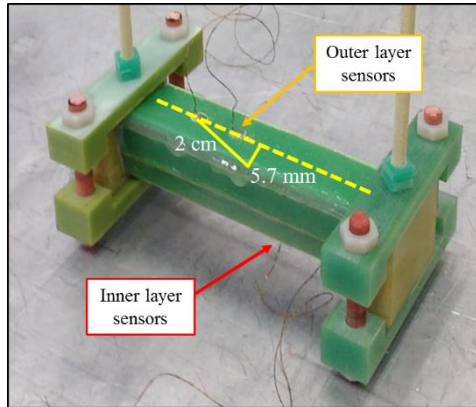


Figure 4.12: Sensors instrumentation in the sample. The figure is similar to 4.3.

The two pairs of sensors are referred as inner and outer center sensors, and as inner-off and outer-off center sensors, respectively. The captions “center” and “off-center” are given with respect to the middle axis of the sample, the two pairs being at  $1/3$  and  $2/3$  of the sample length (which is 140 mm).

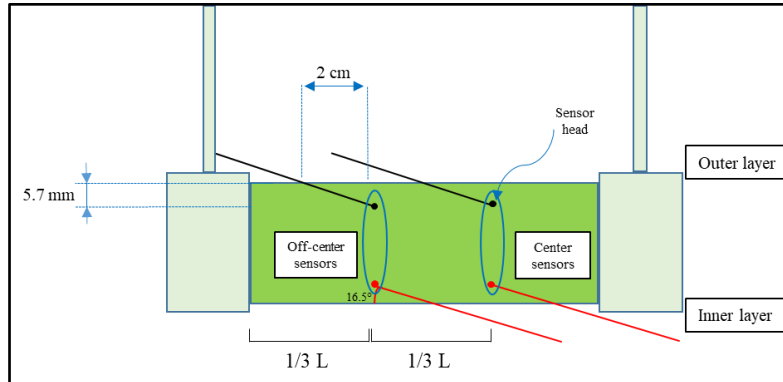


Figure 4.13: Drawing of the insulator box. It shows how the sensors are instrumented.

It has just been said that the presence of two pairs of sensors can be used to assess the uniformity and reproducibility of the measurements, allowing to understand if there is a problem with one (or more) sensors. This is, of course, a common practice in experimental measurements, and it has revealed to be very important also in the present case. In fact, let us have a look at Fig.4.14.

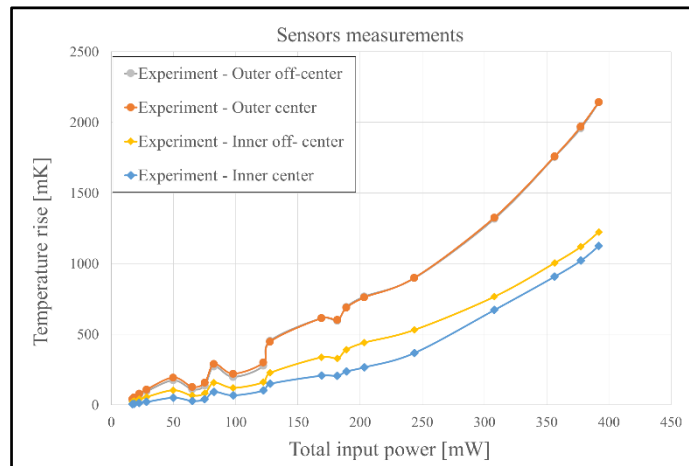


Figure 4.14: Temperature as a function of the total input power, both for the inner (circles) and the outer layer (diamonds).

Fig.4.14 shows the measurements of the temperature increases for the four sensors and for various heating regimes. The temperature bath was fixed at 1.9 K. As reasonable, the comparisons were made for couples of sensors in the same layer. Having a look at the two upper curves (orange and grey), belonging to the “outer” sensors, one can see how measurements were in rather good agreement, starting from a 5% difference for the lowest heating regimes, and going down to less than 1% already at 169 mW, up to the maximum at 392 mW. Table A.III.1 in Appendix III reports the same data in table form, for all the heating regimes applied in the experiment. To be more accurate, the temperature increase reported in Fig.4.15 is  $\Delta T_{p+s,1}$ , already mentioned in the description of the calibration procedure.

The situation is quite different for the “inner” sensors. Disparity is much larger, never being less than 10%, with an average of 30%, and peaks of 75%. The discrepancy between the yellow and blue curves is not negligible both at the lowest and at the middle region of powers. Things improve increasing the input power, but still not in a good agreement as for the “outer” sensors.

It is useful to discuss also some temperature plots as a function of time [47].

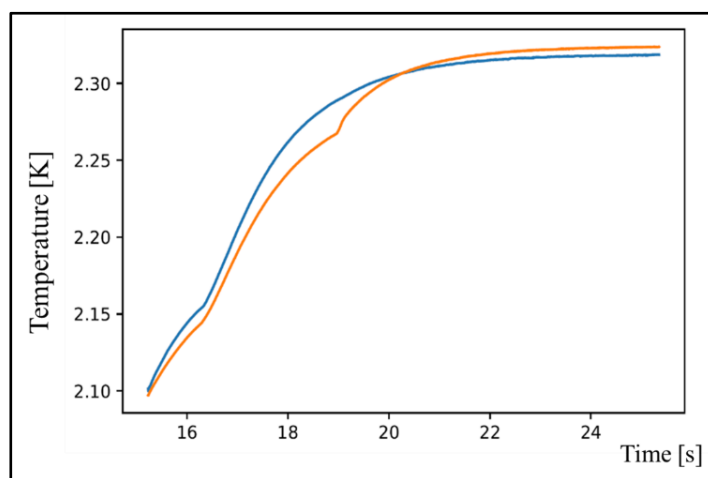


Fig. 4.15: Temperature measurements of the outer pair of sensors, at a helium bath temperature of 2.1 K and 300 Ohm of resistance. Change in the curve slope is a hint of the possible presence of helium in the sample.

Fig.4.15 shows the curves for the pair of outer sensors, at a helium bath temperature of 2.1 K and 300 Ohm of the external resistance. Each sensor presents a change of slope near to 2.2 K, a value which is very close to the lambda temperature,  $T_\lambda$ . This is not what would have been expected from a measurement of a “pure solid” and could be the hint of the presence of helium in contact with the temperature sensors.

It is, in fact, possible to state that a certain, little amount of helium is present close to the sensors, even if it is difficult to evaluate the exact amount that surrounds each sensor. It is not yet clearly explained why this is happening; it could be linked to the insulation stage that takes place during sensors instrumentation. In all of this, the inner-center sensor remains an outlier, the quantity of helium inside it being much higher than for the other three sensors, due to the stronger peaks at  $T_\lambda$ . This is well described and justified in [37].

A further element in support to the presence of helium are the values of the time constants. A time constant is defined as the time it takes for the temperature to reach 63.2% of its steady-state value, and it is a useful parameter for comparison between experiments and simulations. The time constants for the inner-center sensor are around 1.8 and 2.2 seconds (Table A.III.2 in Appendix III), being generally higher than for the other sensors, and it helps in assessing a significant presence of helium close to the inner center sensor itself. Consequently, it has been agreed with the Cryolab team to exclude this sensor from the analysis, so that only the “off-center” pair of sensors will be considered.

#### 4.6 Uncertainty on input power

Another aspect of the measurements is to be pointed out. The calibration procedure is affected by uncertainties, expressed in the form of a relative error as

$$\frac{(P_{nom} + \Delta P/2) - (P_{nom} - \Delta P/2)}{P_{nom}} = \frac{\Delta P}{P} (\%) , \quad (4.2)$$

which is also shown in Fig.4.16 as a function of the total input power.

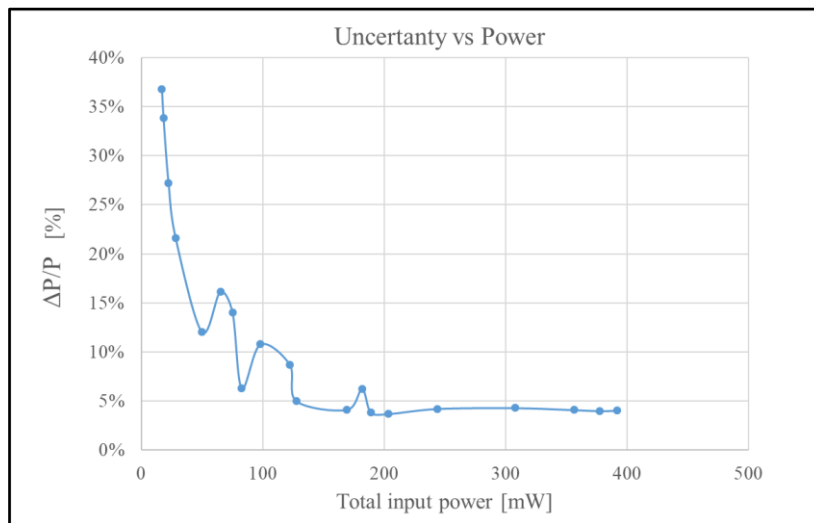


Figure 4.16: Plot of the uncertainty, expressed as  $\Delta P/P$  (%), as a function of the total input power.

As one can clearly see from Fig.4.16, the percentage error is up to 37% at 17 mW and remains still around 10% at 100 mW. It then stabilizes down to 5% from 130 mW up to the highest value of the total input power, 392 mW.

Let's also visualize Fig. 4.17, which presents data in a similar form to Fig.4.14, but with absolute temperature.

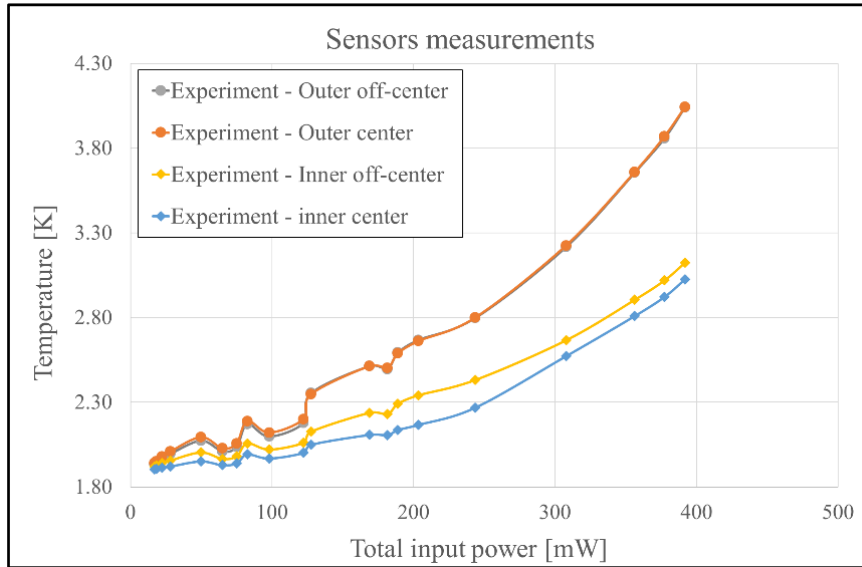


Figure 4.17: Experimental measurements expressed using absolute temperature.

Fig.4.17 shows the temperature evolution as a function of the total input power, for the inner and the outer off-center sensors. The trend is of a general increase with increasing input power, thus showing a positive sign of the first derivative, as it would have been expected.

It is also interesting to notice the sign of the *second* derivative which is positive, indeed

$$\frac{d^2 \Delta T}{dP^2} > 0 . \quad (4.3)$$

If the material properties remained the same with temperature, the  $\Delta T$ 's would have increased linearly with the input power. The real case is different, though, since each material shows a dependence of the thermal conductivity and of specific heat on temperature (see Fig.5.28 for further explanation). This results in a non-linear evolution of the  $\Delta T$  with  $P$ , and we should return on this in the proceeding.

Let us also note that there is a good agreement between the center and off-center outer sensors, their curves being almost overlapped, in contrast to the inner ones, as it has been highlighted through Figs.4.14 and 4.17. Another weird behavior in the experimental data, is in correspondence with five values of the input power (see again Fig.4.14) where it appears to be a dip in the temperature rise. This is clearly not physical and could be a hint of some problems encountered during the measurements, which have yet to be identified.

## 5. Numerical model

### 5.1 Introduction

Starting from the Cryolab experiment, which has already been presented in Chapter 4, a numerical model was developed in order to reproduce the results. The simulation was built up also to identify the parameters that mostly influence the thermal behavior of the coil in response to heat loads.

Simulations are based on the knowledge of physical laws and material properties, and some assumptions are made, like on the boundary conditions to apply. Both the simulation or the experiment can be proved wrong, due to an incorrect assumption, or an error during set-up preparation. For these reasons, careful consideration and practices must be adopted.

The numerical simulation relies on the HEATER software [40], which is a program for the analysis of transient and steady-state heat transfer by heat conduction in three-dimensional solids. It computes the evolution of an initial distribution of temperature in solid materials subject to volumetric heating or cooling, with prescribed boundary conditions. It is based on a general 3-D finite element solver of Partial Differential Equations (PDE), which allows optimal flexibility on the modeled geometry, the heat sources and the boundary conditions considered [40].

The HEATER model consists primarily of a mesh of solid finite elements in 3-D, and the elements implemented range from 1-D line elements, through 2-D shells of triangular or quadrilateral shape, to 3-D solid tetrahedra, pyramids and hexagons [40]. The equation solved by the PDE routine is the transient heat conduction equation

$$\rho c_p p \frac{\partial T}{\partial t} - \vec{\nabla} \cdot (p \hat{k} \vec{\nabla} T) = p \dot{q}''' , \quad (5.1)$$

written here in a general case. In the equation,  $\rho$  is the density, in  $[\text{kg}/\text{m}^3]$ ,  $c_p$  the specific heat, in  $[\text{J}/\text{kg}/\text{K}]$ , and  $\hat{k}$  the thermal conductivity, in  $[\text{W}/\text{m}/\text{K}]$ , expressed as a tensor quantity in a 3-D case. In fact, materials can be anisotropic, which means that they could have different values of thermal conductivity along different directions (as it could be the case of a fiber).  $\dot{q}'''$  is the input power per unit volume, in  $[\text{W}/\text{m}^3]$ : we should return on this definition later. Then,  $p$  is an element property, which in the 1-D case, is the area of the cross-section transverse to the heat flow. If it remains constant all over the domain, it can be simplified in all the three terms of the equation, which then becomes

$$\rho c_p \frac{\partial T}{\partial t} - [(\vec{\nabla} \cdot \hat{k}) (\vec{\nabla} T) + \hat{k} \nabla^2 T] = \dot{q}''' . \quad (5.2)$$

To solve the equation, it is necessary to provide initial and boundary conditions to the problem. An initial condition can be written as

$$T(x, 0) = T_0(x) , \quad (5.3)$$

while boundary conditions can be of different types: adiabatic (no heat exchange through the surface associated with the node where the condition is applied), isothermal (surface at constant temperature) or convective, which means that heat exchange is between the surface and a bulk medium at constant temperature. The PDE solver applies a finite element algorithm on the user mesh for the discretization of eq.(5.1) in space. There is quite a high number of elements programmed in the software, but what we are really interested in are 1-D line elements. They can be made of 2 nodes and first order shape functions (linear), or 3 nodes and second order shape functions (parabolic). They are shown schematically in Fig.5.1.

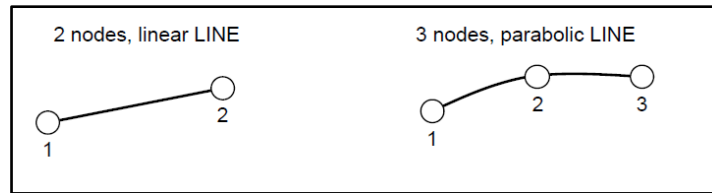


Fig.5.1: Schematic representation of the 1-D finite element types implemented in HEATER [40].

The time discretization is based on a multi-step finite element difference algorithm of the Beam and Warming family with at most a third order accuracy. In numerical mathematics, this algorithm is an implicit scheme, used to solve non-linear hyperbolic equations. The time step is adapted automatically to achieve a user-defined error. The user has control on the time integration accuracy through the choice of the algorithm, while the time adaptivity is controlled specifying the error estimator and the desired accuracy [40].

### 5.2 The Cryolab experiment model

The simulation that has been developed consists of a 1-D numerical model, which reproduces the geometry and the properties of a line that crosses the magnet in the radial direction, as shown in Fig.5.2.

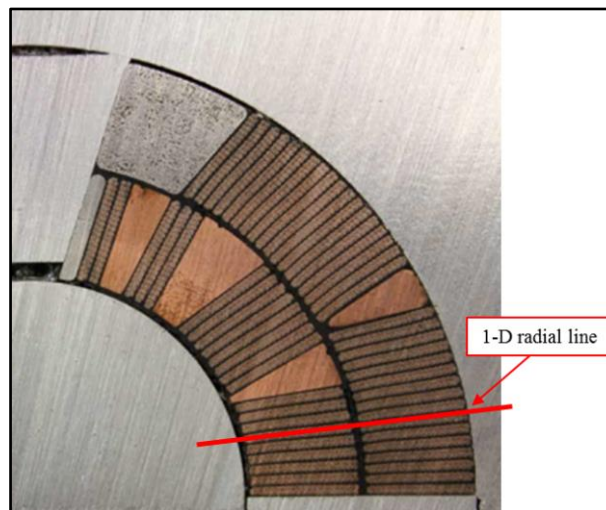


Fig. 5.2: Picture of a quarter of the dipole cross-section, taken with the magnet placed in a mould. Our interest falls upon the 1-D radial line, highlighted in red.

The choice of a 1-D simulation instead of 2-D or even 3-D, was made in order to see if a simplified model was able to give a good description of the magnet behavior, and to see if it could have then been used for similar studies. The behavior of the magnet with its 3-D geometry differs from the model, both for the presence of the copper wedges and the longitudinal development of the coil itself. Nevertheless, it will be the aim of this chapter to show how a 1-D simulation could be a reliable tool to describe the coil behavior as a first approximation.

The model details are depicted in Fig.5.3.

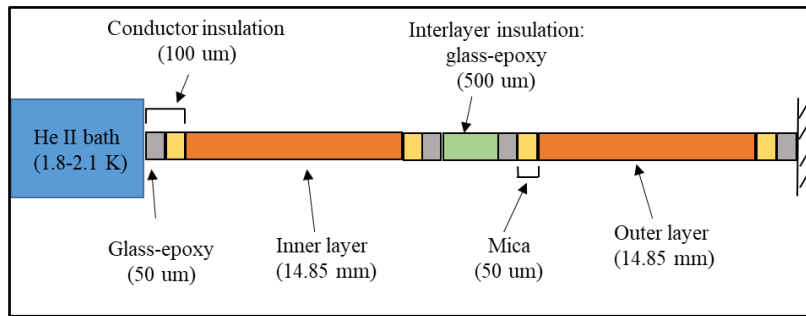


Figure 5.3: Outline of the 1-D radial line.

There are two layers of insulated cables in the sample, separated by an interlayer insulation. The cables are 14.85 mm wide and are made of composite strands with Nb<sub>3</sub>Sn and Copper, in a proportion given by a Cu/non-Cu ratio equal to 1.15. The cable insulation is made up of two layers: one layer of mica (50 μm) and one of impregnated glass-fiber (50 μm), which technically is indicated as: S2 + CTD 101K. They are shown in Fig.5.4.



Figure 5.4: Photograph of the conductor insulation. The external white fiber is S2 glass, while mica comes out on the right, having a chip structure.

The term “mica” actually refers to a composite material which is made of mica (around 65%), glued over a glass tape (25% glass plus 10% glue). The technical data sheet [35], reports: “mica paper bonded to an electrical grade glass cloth as the supporting fabric, impregnated with a specially selected high temperature resistant silicone elastomer”. For what concerns the present purposes and for simplicity, “mica” will be considered with all the properties (thermal conductivity, specific heat, etcetera) of a single material.

On the other hand, impregnated glass-fiber is the common S2 glass-fiber (a white fabric) that undergoes an impregnation stage during coil manufacturing, thus changing its thermal properties. This material is referred to as glass-epoxy and, even if not the same, is usually considered as G10 [48]. The interlayer insulation, being 500 μm thick, is also entirely made by glass-epoxy. Table 5.1 resumes these characteristics.

Type of layer	Material	Thickness/Proportion
Conductor insulation	Epoxy impregnated glass fiber (S2 + CTD 101K)	50 μm
	Mica	50 μm
Interlayer insulation	Epoxy impregnated glass fiber	500 μm
Outer and inner layer	Nb <sub>3</sub> Sn	46.5%
	Copper	53.5%
		Total thickness of a sc layer: 14.85 mm

Table 5.1: Layers and their constitutive materials

Taken all together, the total length of the 1-D radial line is 30.60 mm.

### 5.3 Mesh

A relevant aspect when setting up a simulation, is to have a correct spatial resolution in the regions which are the most interesting to study. In the present case, the insulation layers will play the most important role in determining the temperature profile in the domain. In fact, insulators have a thermal conductivity that is between 3 and 4 orders of magnitude smaller than the cable layers (made up by more than 50% of copper). Consequently, they behave as high thermal barriers to the flow of heat. Making a parallel with the electrical case, where the potential drops significantly in correspondence with high electrical resistances, the temperature drops in a similar way when encounters a high thermal barrier.

The conductor insulation and the interlayer insulation, call for a very dense mesh, with a node located every 10 and 20  $\mu\text{m}$  respectively. On the other hand, due to the higher thermal conductivity in the conductor layers, temperature will tend to flatten out in these regions, so that a much larger spacing can be considered, starting from a value of 200  $\mu\text{m}$ . Table 5.3 resumes the mesh parameters used in our model.

	Outer/Inner layer	Interlayer insulation	Conductor insulation
Spacing	200 $\mu\text{m}$ (75 nodes)	20 $\mu\text{m}$ (25 nodes)	10 $\mu\text{m}$ (10 nodes)

Table 5.3: Mesh spacing in the different regions of the system.

Table 5.3 also reports the number of nodes in each layer. Despite that the outer and inner layers are roughly 150 and 30 times bigger than the conductor and interlayer insulations, their number of nodes is just 7 and 3 times higher, respectively. As a result, the total number of nodes in the domain is 216. Fig.5.5 shows what was written in Table 5.3.

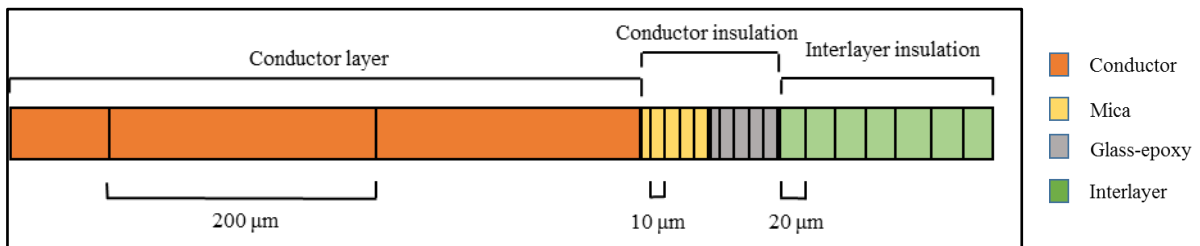


Figure 5.5: Spacing in the domain. Starting from the left and going to the right there are: the conductor layer, the conductor insulation (mica + glass-epoxy), and the interlayer insulation (glass-epoxy)

In fact, it helps to get the idea we are trying to express. It is to be said that this is just a first attempt to mesh the domain, and it is not clear if it is the most suitable to the problem. Therefore, a convergence study should be conducted, in order to understand if the results of the simulations are affected by a change in the mesh spacing.

### 5.4 Initial and boundary conditions

The HEATER software [40] reads an input file which contains all the necessary information for the resolution of eq.(5.1) for the specified geometry. We refer to [40] for all the details about the input file. This section presents only the aspects relevant to the discussion.

“Points” are defined inside the domain in order to extract the temperature in the most critical positions of the system. Of these, five are highlighted in Fig.5.6.

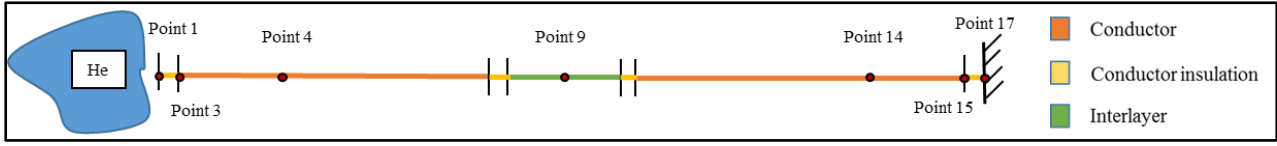


Fig. 5.6: An outline of the domain. The legend indicates the layers in the geometry. Boundary conditions are also represented (convective on the left and adiabatic on the right). Five points are shown, the most important being no. 4 and 14, used for comparison with the measurements.

Starting from the left and going to the right, Point 1 and 3 are on the internal and external surfaces of the conductor insulation of the inner layer, respectively, Point 4 is placed near to the center of the inner layer, Point 9 exactly in the middle of the interlayer insulation and at the center of the dominion, Point 14 is the equivalent of point 4 for the outer layer, and Point 15 and 17 are the end of the dominion. Just as a small note, the most important points, which will be used in the proceeding for the comparison with the experimental results are no. 4 and 14. Table 5.4 provides a legend that will be used also later.

Point	Letter
Point 1	A
Point 3	B
Point 4	C
Point 9	D
Point 14	E
Point 15	F
Point 17	G

Table 5.4: Letter assignment to points in the domain.

#### 5.4.1 Initial condition

The initial condition is applied to the temperature of all nodes, which means a uniform condition all over the spatial domain. It is set depending on the initial temperature of the bath in the experiment, which in this case was 1.9 K. It was assumed that, before turning on the external superconducting magnet, the sample was always in thermal equilibrium with the bath.

#### 5.4.2 Boundary conditions

Boundary conditions have the same physical units independently on the type of geometric support. In a 1-D geometry, there are only two boundary conditions which can be seen back in Fig.5.6.

This paragraph is dedicated to the justification of the choice of the two boundary conditions. The inner layer is directly in contact with superfluid helium, so that heat exchange inside it is dictated by the Gorter-Mellink regime, which is basically a modified Fourier's law for heat conduction

$$\vec{q} = -k(\vec{\nabla}T)^{1/3} \quad (5.4)$$

This behavior is not considered in the software, and a convective condition, with a proper heat transfer coefficient is used at its place. The heat transfer coefficient is derived from the Kapitza formulation, and taken at the proper helium bath temperature, 1.9 K, in order to have the minimum possible discrepancy with the physical situation.

On the other side, there is the right boundary condition. In the Cryolab experiment, the coil sample was inserted in an open box of G10 insulation, 5 mm thick from each side. The outer layer was put in contact with the box, since the only face exposed to helium in real magnet operation, is on the inner radius. The low value of thermal conductivity of G10 and its thickness made us suppose that it constitutes a very high thermal barrier, which in the first place, can be seen as an adiabatic wall.

### 5.5 Heat inputs.

The heat input, which imply the definition of a heat source inside the conductors, is an aspect worthwhile to focus the attention on. Thanks to the calibration procedure, it is possible to assess the total input power in the sample generated by induction, so that this goes from 17 to a maximum of 392 *mW*. HEATER requires the heating input in [*W/m<sup>3</sup>*], so the input power needs to be divided by a volume. This volume should be that of the metallic parts of the sample, since the variation of the magnetic field over time, *dB/dt*, only couples with them. Here derives the importance to compute them carefully.

The sample was derived from a quarter of an 11 T dipole coil, and was made of 9 cables in the inner layer, plus the copper wedge, and 16 cables in the outer layer. Taking the proper dimensions of a bare Rutherford cable, which are 14.85 mm of width, *w*, and 1.307 mm of thickness, *t*, one gets

$$A_{bare\ cable} = w * t = 19.41\ mm^2 . \quad (5.5)$$

The next step is to estimate the metallic fraction in the cable. Strands are twisted in a Rutherford cable, so that a cross section orthogonal to the cable returns an elliptic area of the strands. To compute this area, the two semi-axes dimensions, *a* and *b*, are needed. The strand diameter, being 0.714 mm, is divided for the twisting angle, which is 16.5°, obtaining the first semi-axis

$$a = \frac{d_s}{\cos(\vartheta)} = \frac{0.714\ mm}{\cos(16.5^\circ)} = 0.745\ mm . \quad (5.6)$$

This dimension is slightly enlarged, due to the twisting. No modifications occur along the *y*-direction, so that the second semi-axis, *b*, is *d<sub>s</sub>*, the strand diameter itself.

The elliptical area is then

$$A_{strand} = \frac{a * b}{4 * \pi} = 0.418\ mm^2 . \quad (5.7)$$

There are 40 strands that make up the cable, so the area of metallic parts is just obtained multiplying the previous value by 40

$$A_{metallic} = 40 * A_{strand} = 16.72\ mm^2 . \quad (5.8)$$

This number needs then to be multiplied by 25 (the number of cables in the sample) and by 140 mm, the sample length, so that

$$V_{metallic} = 16.72\ mm^2 * 140\ mm * 25 = 58.5\ cm^3 . \quad (5.9)$$

This is a rather easy way to compute the volume of metallic parts. Being more precise, a volume of 59.1 cm<sup>3</sup> can be derived. The procedure is shown in detail in Appendix II, and this last value will be used in the proceeding, since it is assumed to be a better estimation.

Dividing the column of the total input powers by the metallic volume, values between 0.3 and 6.6 [*mW/cm<sup>3</sup>*] are obtained. Table A.II.3 shows all the values in detail.

The heating, which is the same in both conductor layers, is also considered uniform over the volume length. This assumption has been made just as a starting point to perform the simulations. It could induce errors in the extractions of temperature from the system, and constitutes an interesting topic of further discussion, being deepened hereinafter.

As discussed in section 5.4.1, the sample was in thermal equilibrium with the helium in the pot before applying the heat source. The temperature for the initial condition was taken, from time to time, equal to that of the bath.

This could vary among four values, 1.8, 1.9, 2.0 and 2.1 K, which means that operation was always started from the superfluid, *He II*.

One last point is about the boundary conditions. The sample was inserted into an open box of G10 insulator, which enables helium to be in direct contact only with the inner layer, while all the other sides were insulated by the G10. In the model, a radial line “crosses” the sample, and it is used to model the behavior of the system. Then, the inner side of the line is in contact with helium, while the outer touches the insulator. The box of G10 had walls of 5 mm thickness, the reason why made us suppose that this could play some sort of an adiabatic condition.

On the other hand, the inner face, directly exchanging heat with helium, had a convective condition, which can be written as

$$\dot{q} = h(T_w - T_0) \left[ \frac{W}{m^2} \right], \quad (5.10)$$

where

$$\dot{Q} = \dot{q}A \quad [W]. \quad (5.11)$$

where  $h$  is the heat transfer coefficient, in  $[W/m^2K]$  expressed by the Kapitza formula.  $T_w$  is the temperature of the last node of the domain, and  $T_0$  the bulk temperature of helium, reasonably far from the sample.  $A$  is the area exposed to the fluid.

The adiabatic condition is just an idealization of the real situation, and again, just a starting point to make the first simulations simpler. More careful considerations will be made in the proceeding.

### 5.6 Temperature comparison

In the Cryolab experiment, temperature was extracted from two pairs of sensors, the center and the off-center sensors. It is of great importance to correctly evaluate the position of the sensors, since some points are defined in HEATER in the exact positions where sensors are supposed to be. Temperatures can be compared, in this way, to the measurements.

Figs. 4.13 and 4.14 show that the four sensors were inserted about 2 centimeters inside the sample, at an angle following a strand,  $16.5^\circ$ . A Rutherford cable was drilled in order to remove a single strand, which was then substituted with the sensor probe, presenting the sensor head at his termination.

The head was placed, in this way, fully inside the conductor layer, approximately at a depth of 5.7 mm (the projection of the 2 cm over the twisting angle). However, due to the presence of copper in the conductor layers, the temperature distribution inside them is almost flattened, and it does not really matter where points were located. It could have had an influence only if the sensor was inside an insulation layer but, luckily, this was not the case. Two points were defined to perform the comparison, one in position  $x = 5.8 \text{ mm}$ , which takes into account the 5.7 already mentioned, plus a 0.1 mm of insulation. The other was at 24.8 mm, 5.8 mm inside the sample, from the outer layer side (30.6 - 5.8 mm). Without going in the detail of the input file, but just as a future reference, they were called “point 4” and “point 14”, respectively.

It must now be reminded that the inner center sensor was excluded from the analysis, due to a major leak of helium inside the sample. The leak could be induced by the non-ideal seal effect by the epoxy resin, which may reveal some imperfections during the sensor instrumentation process.

There are, however, still three sensors that can be used: the two off-center sensors, which lay on the same radial line, plus the outer center sensor. This last sensor cannot, unfortunately, be coupled with its inner equivalent, but it would not be correct to discard it altogether. Its measurements are averaged with those of the outer off-center sensor, and then compared with the simulations. This is, for sure, a better approach for the comparison with the experimental measurements.

### 5.7 Simulation results

Let's begin to visualize some results. Fig.5.7 displays the temperature distribution along the spatial dimension of the domain for the lowest heating regime,  $0.288 \text{ mW/cm}^3$ .

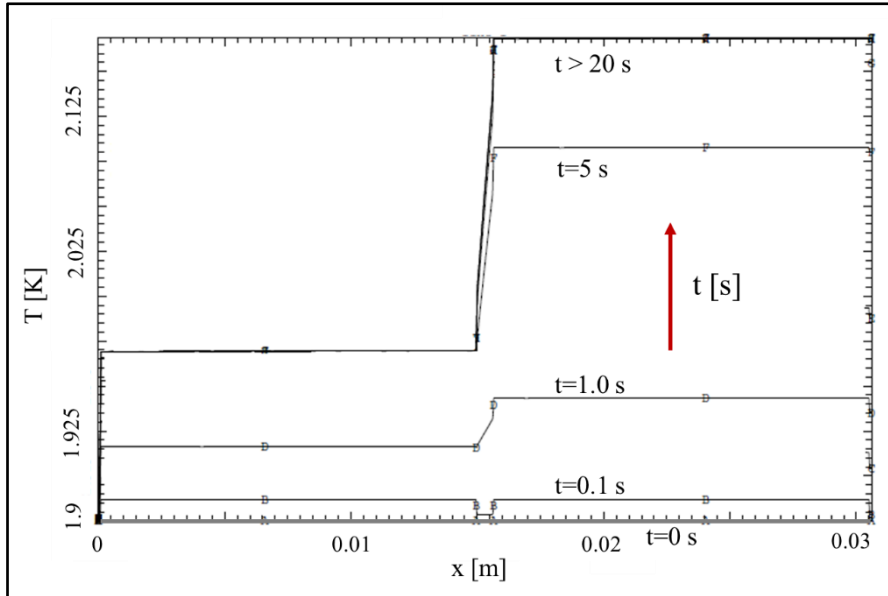


Fig.5.7: Evolution of the temperature profile in time. Steady state was reached after 10 s.

Four curves are represented in Fig.5.7. The lowest ( $t = 0 \text{ s}$ ) shows that the system starts from a temperature of 1.9 K, which is the helium bath temperature for the considered case. In the first 100 ms, the temperature starts to rise in the two conductor layers, while a dip can be observed in correspondence of the interlayer. This last one behaves, in fact, as a heat sink, at least during the first moments, leaving the two conductors as independent from each other. Difficult to see but present, nevertheless, are the dips at the border of the domain, where the conductor insulation are also acting as sinks, keeping the temperature increase confined inside the layers.

The adiabatic condition on the right wall starts to play its role after these first moments, then the temperature on the outer layer rises more rapidly. The inner layer, on the contrary, experiences contact with helium on the left, its temperature being restrained by heat exchange with the fluid. The biggest part of the temperature evolution is reached within the first five seconds from the initial heating, stabilizing approximately after ten seconds.

There are two main drops in the spatial temperature distribution during steady-state. They can be recognized thanks to their respective slopes. Looking at the interlayer insulation, the smaller slope is produced by the  $500 \mu\text{m}$  of impregnated glass-fiber. The other two, on the left and on the right of the interlayer, are caused by mica which, despite being only  $50 \mu\text{m}$  thick, has a very low thermal conductivity and behaves as a thermal wall to the flow of heat. The same effects are present on the left boundary, as well, but are much more difficult to distinguish due to the small dimension ( $0.1 \text{ mm}$  versus the  $0.7 \text{ mm}$  of the total dimension of the insulation in the middle of the domain).

A second graph of interest is Fig.5.8, representing temperature evolution in time, with specific coordinates used as parameters.

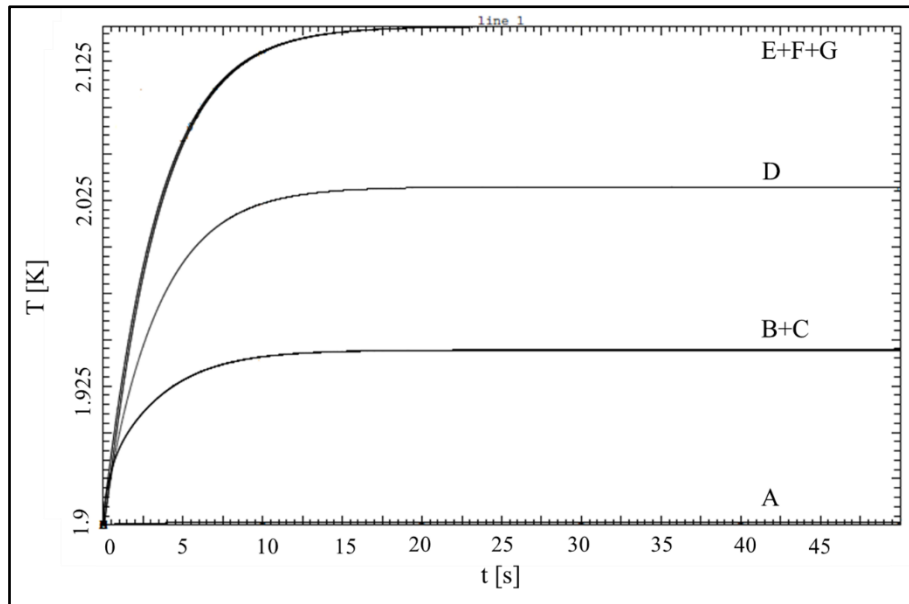


Fig.5.8: Temperature evolution in time with selected coordinates as parameters. The differences in the curves is given by the different thermal resistances seen by the different points.

Seven points were selected to plot the temperature as a function of time, even if only four curves can be distinguished in the graph. Letters refer to Table 5.4 above. Curve “A”, which represents point 1, just slightly increases its temperature over time, remaining low because of the contact with helium. B and C come together and next, because there is almost no thermal resistance between them, the first being at the edge of the left conductor of the inner layer, and the other directly on the inner layer. Point D is right in the centre of the domain and in the interlayer, so its temperature differs from all the others significantly, having insulation on its right and left. Finally, Points F and G are placed in the conductor insulation and together with point E, which is in the outer layer, show the same evolution in time. Their temperature is the highest in the domain, due to the adiabatic condition on the right wall.

Time constants, on the contrary, are shorter in the inverse order. Points closer to the adiabatic wall see their temperature increase faster, and even if their steady-state value is higher, the time to reach it is smaller; the opposite is valid for points closer to helium, which of course acts to remove heat from the system.

### 5.8 Analytical validation

Finite element codes are very useful and fascinating tools. They enable to solve partial differential equations for the most various types of geometries, boundary and initial conditions, and can show all different kinds of results desired by the user, both in the form of plots and print-out files. It would not be possible to do all the same analytically, since it would require days of calculations and just for the solution of very simple cases. Luckily, for the present geometry, it is possible to make some analytical check, thus having a way to confirm or disprove the computational results.

To be more specific, temperature steps across the layers of insulation can be checked. There are two of them: on the left conductor insulation of the inner layer, and across the interlayer. The insulations can be treated as thermal resistances, whose definition is:

$$R_{th} = \frac{\Delta T}{\dot{Q}} \quad , \quad \left[ \frac{K}{W} \right] . \quad (5.12)$$

To be able to correctly apply the formula, it is useful to have a look at Fig.5.9.

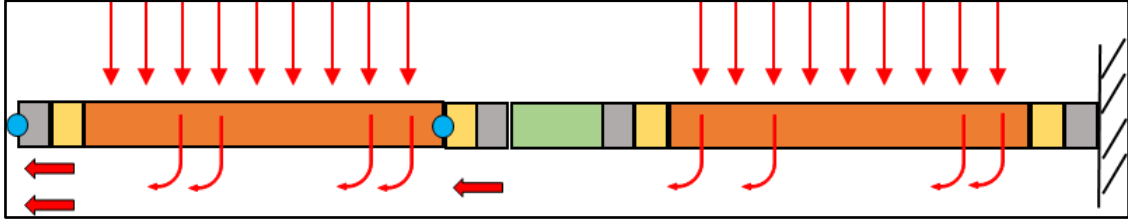


Figure 5.9: Steady-state condition and direction of heat outflow.

The input power is uniformly distributed over the inner and the outer layers, schematically shown through the equally spaced vertical red arrows. At steady-state, the adiabatic wall forces heat to drain towards the inner layer, so that once heat is deposited (let's say by a vertical arrow), it immediately changes direction and starts flowing towards the helium.

Considering the light-blue coloured point on the right, it experiences all the heat coming from the outer layer, which is:  $P_d * l$ , and whose units are  $W/m^2$ . The other point, on the left, sees heat generated inside the inner layer, plus the heat already coming from the outer layer, so that the total heat flux through it is:  $2 * P_d * l$ .

Calling  $\Delta T_1$  and  $\Delta T_2$  the drops across the interlayer and on the left conductor insulation, respectively, we can write

$$\Delta T_1 = R_1 * 2\dot{Q} = R_1 * 2q_0 * l, \quad (5.13)$$

and

$$\Delta T_2 = R_2 * \dot{Q} = R_2 * q_0 * l. \quad (5.14)$$

Let's make an example of comparison, then, taking a helium bath temperature of 1.9 K and a  $q_0$  of  $0.843 \text{ mW/cm}^3$ . The left insulation is made of mica and glass-epoxy (G10).

Resistances are computed using (5.12), as

$$R_1 = \frac{S_{mica}}{k_{mica}} + \frac{S_{G10}}{k_{G10}}, \quad (5.15)$$

where the dimensions are specified in Table 5.1. Thermal properties are extracted from [36] and at 1.9 K, as a first attempt. Table 5.5 resumes all the thermal conductivity data used in the following computation.

Thermal conductivity	Material	Temp [K]	Units [W/m/K]
	<b>Mica</b>	1.9 K	$6.0 * 10^{-3}$
		2.1 K	$6.4 * 10^{-3}$
		2.2 K	$6.8 * 10^{-3}$
		2.6 K	$8.2 * 10^{-3}$
	<b>G10</b>	1.9 K	$2.04 * 10^{-2}$
		2.2 K	$2.63 * 10^{-2}$
		2.4 K	$3.03 * 10^{-2}$
		2.6 K	$3.42 * 10^{-2}$

Table 5.5: Thermal conductivity values for Mica and G10 at various temperatures between 1.9 and 2.6 K.

So

$$R_{1,1^\circ} = \frac{S_{mica}}{k_{mica}(1.9K)} + \frac{S_{G10}}{k_{G10}(1.9K)} = \frac{5 * 10^{-5}}{6.0 * 10^{-3}} + \frac{5 * 10^{-5}}{2.04 * 10^{-2}} = 0.0108 \frac{m^2K}{W} , \quad (5.16)$$

$$\Delta T_{1,1^\circ} = R_1 * 2q_0 * l = 270.4 \text{ mK} , \quad (5.17)$$

while from the computations, the temperature drop is 258.1 mK. The relative error is 4.8%, but we have taken the thermal properties as the materials were at 1.9 K all over the domain, so it is possible to make an improvement. Considering the  $\Delta T_{1,1^\circ}$  to estimate the temperature steps inside the system, we can make a second tentative, with glass-epoxy again at 1.9, while mica at 2.1 K (mica sees the highest  $T$  drop)

$$R_{1,2^\circ} = \frac{S_{mica}}{k_{mica}(2.1K)} + \frac{S_{G10}}{k_{G10}(1.9K)} = \frac{5 * 10^{-5}}{6.4 * 10^{-3}} + \frac{5 * 10^{-5}}{2.04 * 10^{-2}} = 0.0103 \frac{m^2K}{W} , \quad (5.18)$$

$$\Delta T_{1,2^\circ} = 257.9 \text{ mK} , \quad (5.19)$$

which gives an error of less than 1%. A similar procedure can be followed for the interlayer. In a first approximation, the resistance across the interlayer and of the two cable insulations is

$$R_{2,1^\circ} = 2 * \frac{S_{mica}}{k_{mica}} + 2 * \frac{S_{G10}}{k_{G10}} + \frac{S_{int}}{k_{int}} . \quad (5.20)$$

Let's start by considering all the thermal conductivity again at 1.9 K, so that

$$R_{2,1^\circ} = \frac{1.0 * 10^{-4}}{6 * 10^{-3}} + \frac{1.0 * 10^{-4}}{2.04 * 10^{-2}} + \frac{5.0 * 10^{-4}}{2.04 * 10^{-2}} = 0.046 \frac{m^2K}{W} , \quad (5.21)$$

and,

$$\Delta T_{2,1^\circ} = R_{2,1^\circ} * \dot{Q} = R_{2,1^\circ} * q_0 * l = 575.9 \text{ mK} . \quad (5.22)$$

The  $\Delta T$  from the simulation gives: 421.8 mK, which requires some improvement. Let's then split the contributions from the layers of mica and G10, since a pair belongs to the inner layer and one to the outer, thus experiencing different temperatures. The first layer of the conductor insulation is considered at 2.2 K, the interlayer at 2.4 K, and the last conductor insulation at 2.6 K. We obtain

$$R_{2,2^\circ} = \frac{S_{mica}}{k_{mica}(2.2K)} + \frac{S_{G10}}{k_{G10}(2.2K)} + \frac{S_{int}}{k_{int}(2.4K)} + \frac{S_{mica}}{k_{mica}(2.6K)} + \frac{S_{G10}}{k_{G10}(2.6K)} , \quad (5.23)$$

$$R_{2,2^\circ} = \frac{5 * 10^{-5}}{6.8 * 10^{-3}} + \frac{5 * 10^{-5}}{2.63 * 10^{-2}} + \frac{5 * 10^{-4}}{3.03 * 10^{-2}} + \frac{5 * 10^{-5}}{8.2 * 10^{-3}} + \frac{5 * 10^{-5}}{3.42 * 10^{-2}} = 0.033 \frac{m^2K}{W} , \quad (5.24)$$

$$\Delta T_{2,2^\circ} = 413.1 \text{ mK} , \quad (5.25)$$

which is a discrepancy of 2.1%. It is a little bit higher than for the second tentative for the insulation layer, but it is due to the higher temperature drop across the thicker insulation, which would require to take even smaller layers, each with its own temperature, to get a better result.

Despite the limitations given by analytical computations, the few previous lines have demonstrated how they still reveal to be adoptable and that they can be used as useful tool to cross-check the much more complicated calculations made by the machine. To conclude this paragraph, it is fascinating to use simple formulas to get a sense of the numbers involved in the problem.

### 5.9 Analysis of the results

It is time now to present some other results, which will enable to look at the Cryolab experiment from different angles. To begin with, let's remind that the experiments were conducted using different values of the input power, so that the temperature increase, at steady-state, as a function of this parameter can be visualized looking at Fig.5.10.

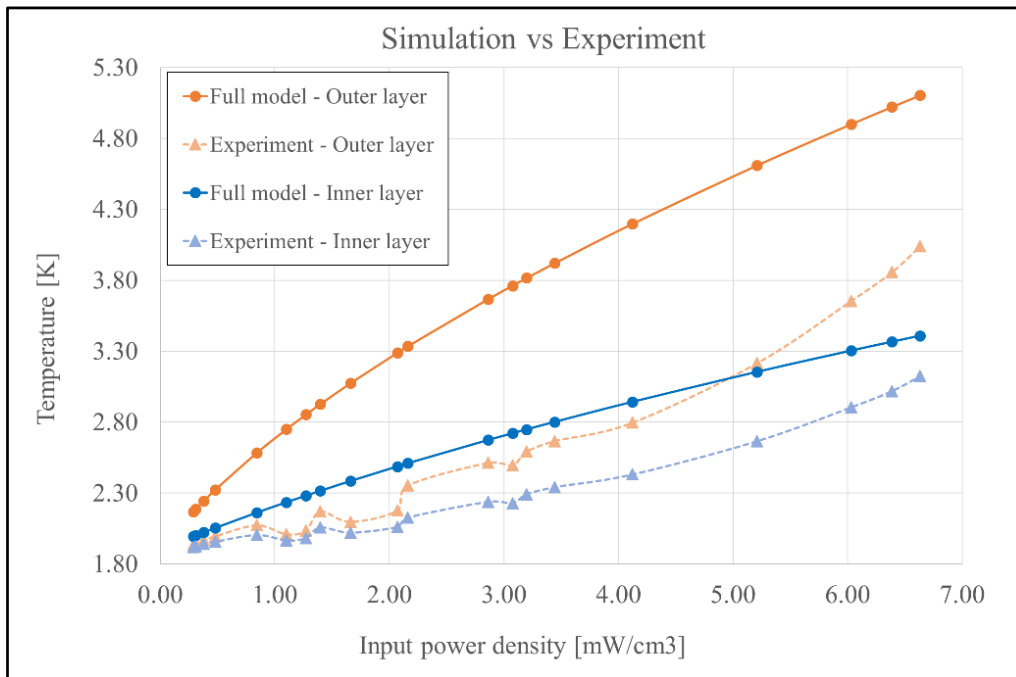


*Fig.5.10: Temperature plot as a function of the input power, both for the experiments and the simulations, at steady-state. The dashed lines represent the experiments, the continuous are for the simulations.*

The caption “full model” is used to indicate the model with materials implemented as from design project. “Full” was adopted being a short word. The full model and the experimental curves need to be analyzed in two pairs, one for the inner and one for the outer layer. Fig. 5.10 refers to the case of a helium bath temperature of 1.9 K. Circles are for the temperature values obtained from the simulations, while triangles are for the experimental measurements.

What can be immediately noticed is that the discrepancies are quite relevant already for the inner layer, starting from 4%, reaching a peak of 20% at middle power regimes, and then going down to 9%. The situation is even worse for the outer layer, for which discrepancies are of 12, 50 and 26% when the same power range is scanned. This oscillating behavior in the discrepancy could be explained by the second important feature of the graph, namely the opposite concavity in the experiment and in the simulations. We will come back on this in section 5.12.

As for now, these “errors” are too high, since a simulation can be considered accurate only if it remains inside a 10-15% band of difference with the experiments. Fig.5.11 depicts data in an opposite way.

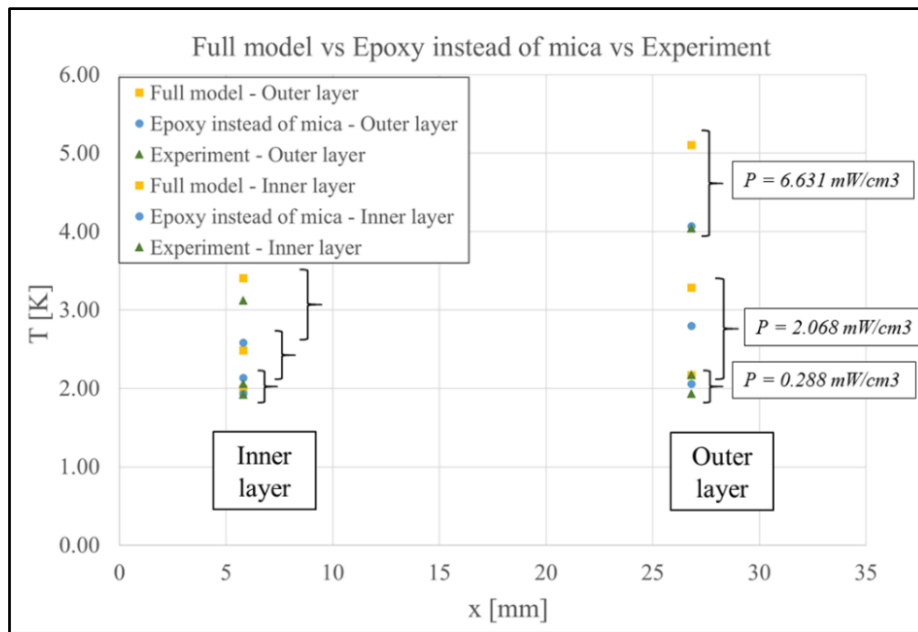


Figure 5.11: Data points for the full model (yellow squares), the model with mica substituted by epoxy-resin (blue circles) and the experiment (green triangles).

In fact, it shows *Temperature vs x-coordinate* for the inner and outer layer, with input power taken as a parameter. In this way, we can realize that all the following comparison are made just in these two points.

Points are reported only at 5.8 and 24.8 mm, which correspond to the position of temperature sensors in the inner and outer layer. Data are organized in three “blocks”, highlighted in brackets, which correspond to input power densities of 0.288, 2.068 and 6.631 mW/cm<sup>3</sup> or, which is the same, 17, 122 and 392 mW of total input power. Points representative of another simulation have also been added, in order to compare the results it gives with the “full” model. In such new simulation, mica is substituted with epoxy resin, and the reason for that will be clarified later on.

At the lowest value of input power, points from the experiment (green triangles), the full-model simulation (yellow squares), and the simulation with epoxy instead of mica (blue circles), are very close to each other, so that the approximation seems rather good (7% for glass-epoxy and 12% for the full model). For the middle range of input powers, the situation changes completely. Both the blue circle and the yellow square are away from the experimental point, which even falls inside the previous block. Even for the glass-epoxy case, the discrepancy is still 30%. For the highest level of power, the glass-epoxy simulation falls very near to the experiment (only 1.5% difference), while the full model is still far, being at 26% difference. In the case of the inner layer, the two simulations are actually very close to the experiment both at low and middle powers, then going to -15% and +9% at higher regimes.

Three values of input power have been presented in the graph, and they are descriptive of the general behavior of the system. It seems that the inner layer can be better approximated by the simulations, especially for what concerns epoxy-instead-of-mica, for which case the curves really lay inside the experimental ones up until medium-high powers.

A third type of graph, which is worth to be presented, is showed in Fig.5.12 and reports a plot of correlation between experimental and computational  $\Delta T$ s.

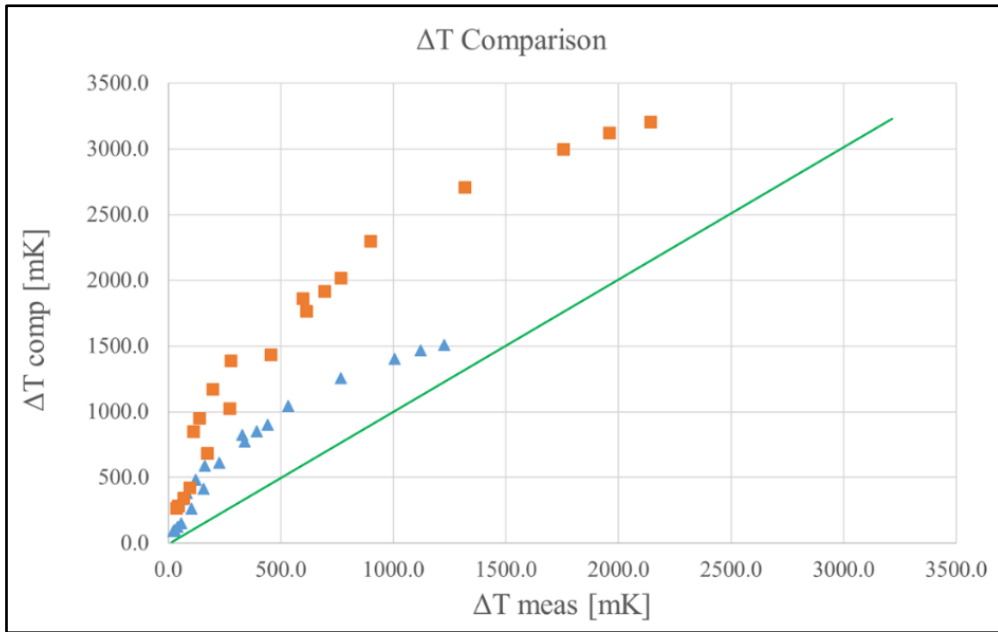


Fig.5.12: Comparison between measured and computational  $\Delta T$ s.

Ideally, points should lay on the green bisector line. This would mean that, for a measured  $\Delta T$  in the experiment, the simulation would be perfectly able to reproduce it. The plot is quite explicative, in the sense that it shows how the computational  $\Delta T$ s are bigger than the experimental.

The discrepancy starts from almost zero at low power, both for the inner and the outer layer, but it then increases as the input power goes up. Considering the outer layer, and for a computational  $\Delta T$  of 1500 mK, correspondent to an input power of 2.160 mW/cm<sup>3</sup>, the measured value is just 500 mK. Even if the situation gets better for the inner layer, at an input power of 4.122 mW/cm<sup>3</sup>, the computation gives 1000 mK, while the experiment 500 mK of temperature increase. Things come back to be better at higher values of input power, but points are still far from the ideal line.

### 5.10 Time constants

Another factor of comparison between simulations and experiments are the time constants, already defined in previous sections. They are determined by the sample composition, and by two material properties in particular: thermal conductivity and specific heat. In fact, time constants refer to the transient condition, so that all terms in eq.(5.1) play a role. Time constants start from 1.5 seconds, experiencing a rapid increase to 2.5 s at 2.0 mW/cm<sup>3</sup>, to slowly return to 1.5 s at the highest heating regimes. All this can be visualized in Fig.5.13. Table A.III.2 in Appendix III shows numerical values.

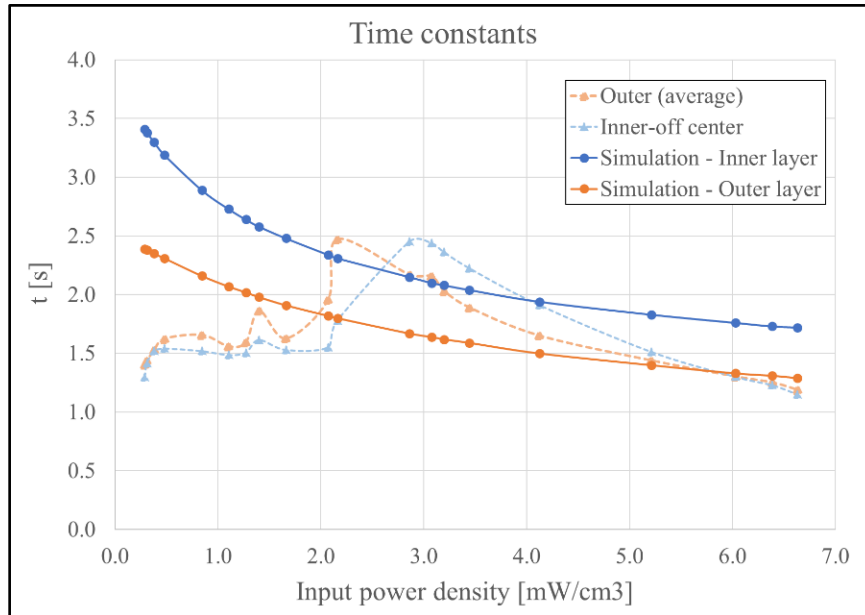


Figure 5.13: Time constants. Experimental values are shown with dashed lines, simulation results using continuous lines. Simulations refer to the full model (mica + glass-epoxy).

A good result from the simulations (the continuous curves) is that the time constants are in the same order of magnitude of the experiments, with values that progressively decrease with increasing the input power. The agreement is very good for input powers above 150 mW, while the simulation overestimates the experimental values by a factor 2 at low powers. The “peak” feature of the time constants at middle powers, coming from the measurements, is not present in the simulation, and could be the hint of possible helium leaks in the sample.

### 5.11 Discussion of the results.

The presentation of the simulation results has shown that we are not able to reproduce the experimental data as they have been given to us by the Cryolab team. The full model, as it has already been called, and which reproduces the design geometry and materials, contains something that needs to be modified if we want to get closer to experimental data. This also includes initial and boundary conditions, together with all the other factors which contribute in forming the temperature evolution and steady-state profiles.

Experimental results are not flawless, as well. Looking back at Fig.4.17, the calibration procedure was far from being perfectly accurate. In fact, the uncertainty on the input power reaches very high values (more than 35%) at low powers. Another important point about the experiment is that, it is not clear what is the actual precision and accuracy of the measurements.

Sensors of the “Cernox” type are commonly used at low temperature, due to their very high resolution. In fact, they are *semi*-conductors, which have a completely different behavior with respect to *super*-conductors, their resistivity becoming higher and higher as the temperature approaches the absolute zero. This is a very relevant aspect when considering a measurement, since, if the resistance is high, to a little variation in temperature

corresponds a big variation in the voltage. This, in turn, can be easily measured even in the order of 1  $\mu\text{V}$ . Figure 5.14 shows this behavior.

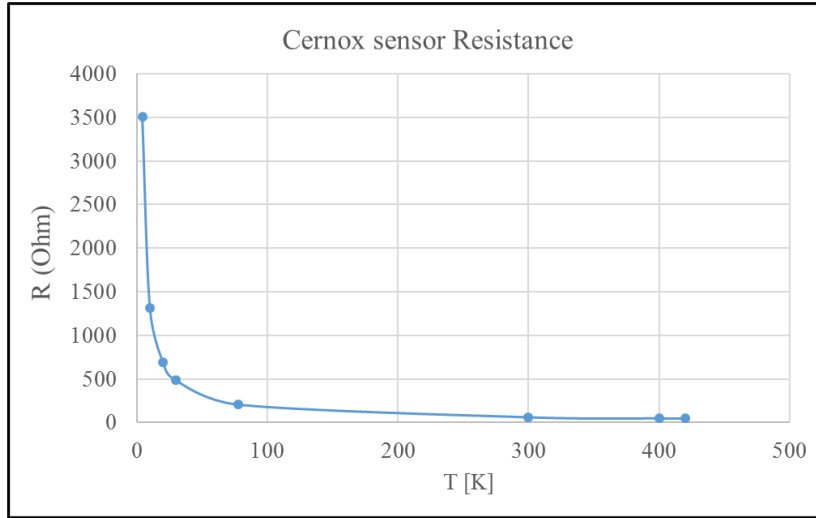


Figure 5.14: Plot of the resistance (and resistivity with it) of a Cernox sensor, as a function of temperature. Precise data are shown in Table A.III.4 in Appendix III.

Resistance only continues to get higher as the temperature gets lower ( $1/T$  shape). It arrives at 11000  $\Omega$  at 1.9 K, with the derivative value up to 4000  $\Omega/\text{K}$ . A rough calculation gives

$$\Delta V = \Delta R * I \approx \frac{dR}{dT} * \Delta T * I , \quad (5.26)$$

$$\Delta V \approx 4000 \frac{\Omega}{K} * (0.1 * 10^{-3} K) * (3 * 10^{-6} A) \approx 1.2 \mu V , \quad (5.27)$$

which means that, powering the sensor with a 3  $\mu\text{A}$  current, one can distinguish a temperature variation of 0.1 mK, if able to measure voltages in the micro-volt range. At 4.2 K the value becomes 1 mK.

It is clear that the resolution of the measurement is very high, but there are other quantities to be taken into account. A measurement, or a set of measurements are characterized by precision and accuracy. Precision takes into account the difference between each measurement, so that a set is precise if the values are close to each other. Accuracy, on the other hand, is the mean value of the set of measurements, and a set is said to be accurate if this mean value is close to the *real* value.

Measurements can be accurate but not precise, precise but not accurate, neither or both. These are, of course, only general concepts, and it is not the aim of this work to go deeper inside the subject, but it is however useful to get a sense of them, in order to look at the experimental values in a critical way [41]. Precision and accuracy both contribute to the evaluation of error bars. Unfortunately, we are not aware of such experimental error bars in the present case, which is something that could have helped us in trying to explain the differences between experiments and simulations.

Other approaches will be undertaken, in order to see if it is possible to get closer to the experiments, but, as a matter of fact, they will all act only on the simulation side, with no chance to make further analyses on the experimental data.

### 5.12 A first consideration.

The geometry of the 1-D radial line and its material composition have been implemented in the model, as they are from the design project of the 11 T dipole magnet. One of the most decisive contributions to the temperature distribution inside the geometry is given by mica, which is an electrical insulator and has also a very low thermal conductivity. Table 5.6 reports the values of this physical quantity for mica and for the other two insulation materials of the coil, namely epoxy-resin and glass-epoxy (G10), at 1.9 K.

Material	Thermal conductivity (at 1.9 K)
Epoxy resin	$3.32 \cdot 10^{-2}$ W/m K
Glass-epoxy	$2.04 \cdot 10^{-2}$ W/m K
Mica	$6 \cdot 10^{-3}$ W/m K

Table 5.6: Comparison of thermal conductivity for the insulation materials

Thermal conductivity values are almost the same for glass-epoxy and epoxy-resin, while for mica the value is 5.5 and 3.4 times lower, respectively. Acting as a very high thermal barrier, mica forces the temperature to rise significantly in the outer and inner layer, referring to a same heat flux and at steady state. This can be easily verified with some analytical check. At the same time, it explains why the *Temperature vs Input power* plot (Fig.5.10) gives such high discrepancies.

A couple of considerations can now be made. Mica is used as an electrical insulator, being wrapped around the unreacted superconducting cable, in a way that it does not close perfectly around it. This is done mainly for two reasons: 1) ensure an opening to let the resin to get in during the impregnation process, and 2) avoid the risk of over-thicknesses, which would induce high mechanical stresses on the cable itself. During the manufacturing process, an impregnation stage occurs in which epoxy-resin fills all the small interstices in the cable, and it penetrates wherever it is possible. Cables are also subjected to heat treatments, which have shown to induce cracks in the mica layer [41]. All these factors could enable epoxy-resin to pass through the thin spaces left from the open and broken mica, so that heat would flow directly along the paths of higher thermal conductivity, provided by the epoxy, thus avoiding mica.

For these reasons, simulations were run in which mica was replaced by epoxy resin, and the result, for the outer layer, is shown in Fig.5.15.

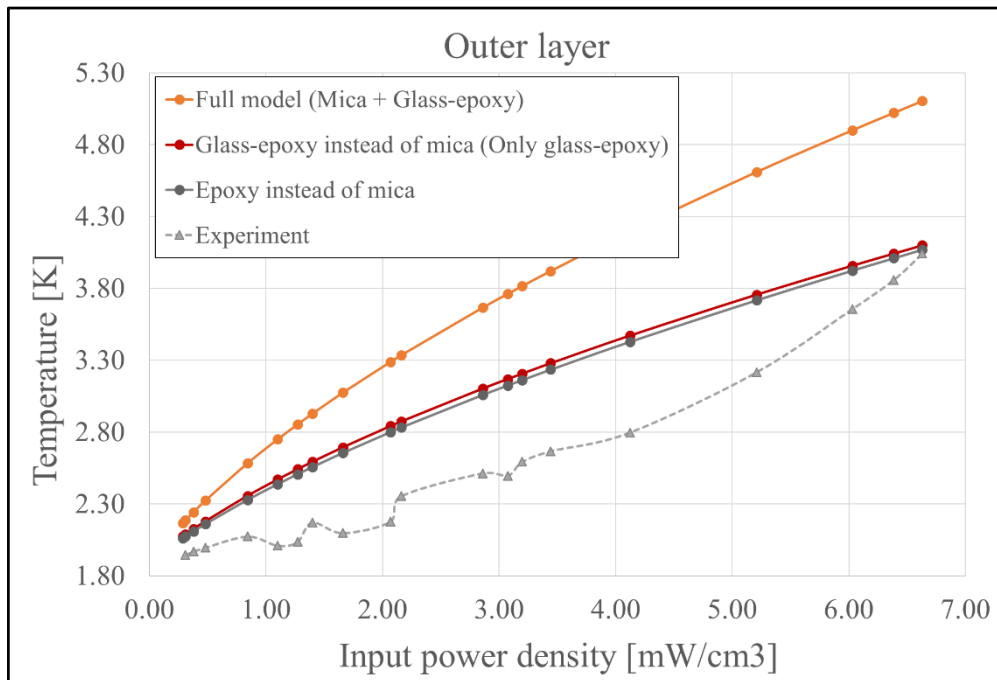


Fig.5.15: Simulation results for the outer layer, with the two added cases of epoxy-resin and glass-epoxy instead of mica.

Results are very promising. As before, the orange curve represents the *full model*, where the insulation is made of mica and glass-epoxy and the dashed grey line is for the experimental points. The two new curves are for the substitution of mica with epoxy-resin (in black) and with glass-epoxy (in dark red), respectively; this last case was made just as a comparison. Simulation results are now much closer to the experimental, with a very good agreement at low (7%) and high input powers (1%). Bigger differences are observed in the central region, where they are still up to 28%, but only because of the “anomalous” data, that are points which do not lay exactly on the smooth curve. If those “dips” were removed, the maximum difference would be 20%, which is something near to the acceptability criterion of 10-15%.

With this change in the insulation materials, temperature profiles are different, see Fig.5.16.

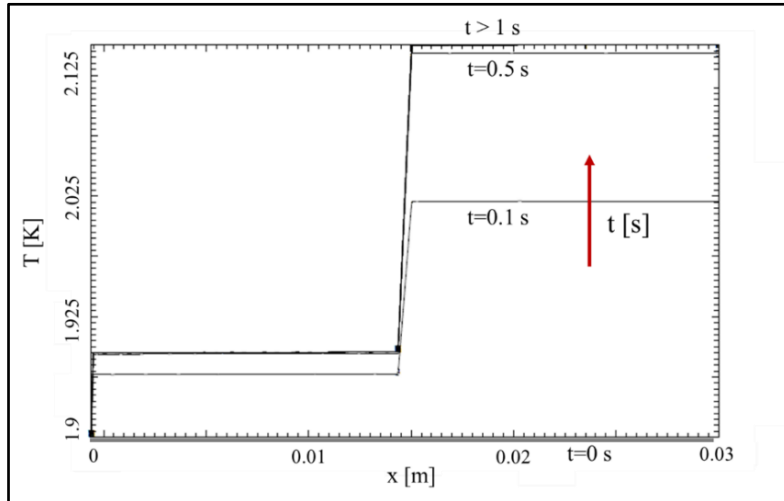


Figure 5.18: Temperature evolution in Point 4 and 14.

Time constants are much shorter with respect to the full model, being displayed in Fig.5.18.

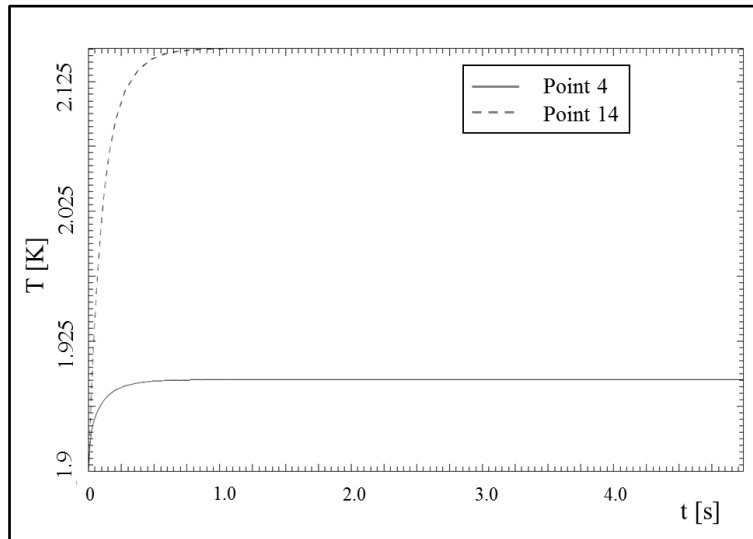


Figure 5.16: Temperature distribution over the domain in the new geometry. The sharp profile given by mica is not present anymore.

Values were previously around 2-3 seconds, while now are down to 0.1 s, an entire order of magnitude smaller. Unfortunately, this result is in contrast with the temperature profile enhancement already cited, and it is a reason of concern. A possible explanation will be proposed in the following sections, also related to the next point.

It is very interesting to notice that, if the concavity of the curve was the opposite, the simulation would have been able to reproduce the experimental results with a high degree of precision.

It is of major importance to understand why such a behavior takes place, also thinking about what would happen at higher regimes, whether the discrepancy would return to increase or, in the case the experimental curve changed, would remain tight.

As a final note, it is nice to notice how glass-epoxy lays just above the curve of the epoxy-resin. As Table 5.13 showed, glass-epoxy has a lower thermal conductivity, so that it gives slightly higher thermal resistances, which in turn induces higher temperatures in the conductor layers. This is an evidence of how, with sample calculations it is possible to give sense again to the computational results.

### 5.13 The fall of the adiabatic condition

It is very important to use the correct set of boundary conditions in order to obtain the correct solution of the heat conduction equation. For the 1-D radial line under current investigation, one of the two conditions was, perhaps short-sighted, namely the adiabatic condition on the right wall.

The sample was inserted in the insulator box, which was made of G10 and had a 5 mm thickness. Indeed, it acts as a high thermal barrier, but some heat still flows inside it, being then exchanged with the external helium bath. This means that the wall is not perfectly adiabatic, and that the boundary condition should be replaced with another convective condition.

New nodes, elements and points have been implemented in the geometry. The length of the domain is now 35.6 mm, and there is a 500  $\mu\text{m}$  spacing between each node in the G10 insulator on the right (which represents the box). Such a mesh has just the purpose to verify if the effect of the convective condition was important or not.

This effect is depicted in Fig.5.18.

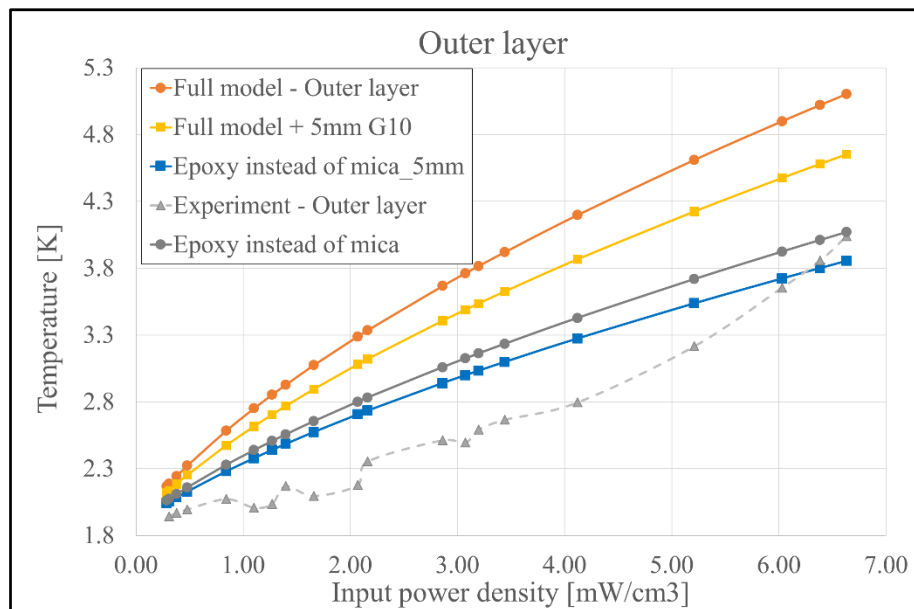


Fig.5.18: Results of the addition of the 5 mm of G10 on the right wall, with a convective condition which takes the place of the adiabatic one.

Two additional curves are presented: the yellow and the blue one (depicted with squares). The former shows the results for the full model with the addition of 5 millimeters of G10 and the convective condition on the right wall. The enhancement in the results is remarkable, registering 500 mK less than in the previous case at the highest input powers. The latter shows a similar behavior, but for the substitution of mica with epoxy-resin,

with a decrease of 200 mK. Another point of major interest is that the simulation curve finally comes up to cross the experimental, in correspondence to the point second to the last.

Similar trends can be recognized in the inner layer. The benefit given by the introduction of helium on the right boundary is still observable, even if weakened by the greater distance from this new boundary condition. The experimental curve was already well approximated thanks to mica substitution with epoxy, both at low and middle power regimes. This even enhances when the 5 mm of insulation are added.

What really differs from the previous case is that the experimental curve this time is enclosed in the middle of the two different types of simulations, as can be seen from Fig.5.19.

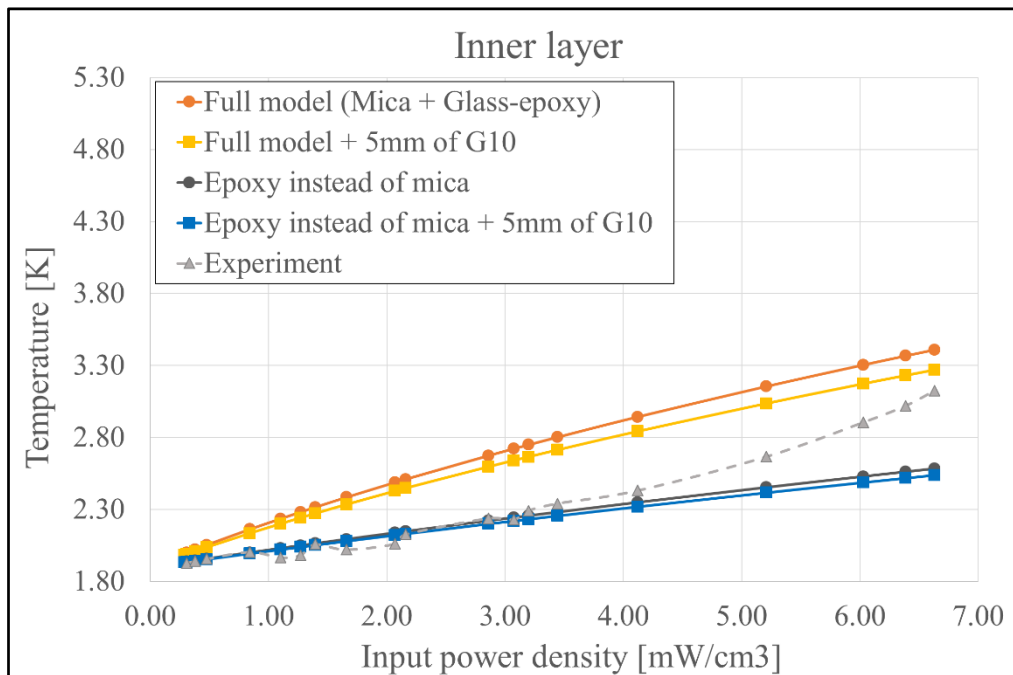


Figure 5.19: Simulation results for the inner layer, with the same considerations made for Fig.5.18. The experimental curve lays in the middle of the two types of simulation curves.

This is rather surprising, since the simulation is supposed to give similar trends of the temperature increase as a function of the input power, both for the inner and the outer layer. We would have expected, then, the same type of discrepancies for the two layers, which is something that does not happen. The fact that the experimental curve remains lower than the two main models in the outer layer, and between them in the inner layer, could be the hint of something that is missing from the experimental or the simulation side.

#### 5.14 Other comparisons: the error bands.

To obtain an additional point of view on the current subject, various options can be surveyed, one of which consists in “mixing” the available information about the experiment and the simulation. Unfortunately, temperature data are characterized by five significant digits, which is rather difficult to reproduce with a small error. At the same time, data have not been provided with the error bands, so that we can only try to modify the model in order to get closer to them.

Despite all of this, data points are not the only quantities which come to the attention when considering the experiment. The heating power provided to the sample by induction, applying a  $dB/dt$  with the external solenoid, was estimated through a calibration procedure, which was affected by uncertainties. These were higher at lower powers, where they were equal to 37%, and went down to a stable 5% from 120 mW up to the highest regime.

What was tried was to run simulations at energy levels defined by the uncertainty bands of the calibration procedure. To make an example, if one considers the lowest value of input powers, 17 mW, an uncertainty of

$\pm 37\%$  gives a lower bound of 11 and an upper bound of 23 mW, respectively. Running the simulations for these values of input power, and presenting graphs as *Temperature vs x-coordinate*, similarly to Fig.5.12, one obtains Fig.5.20.

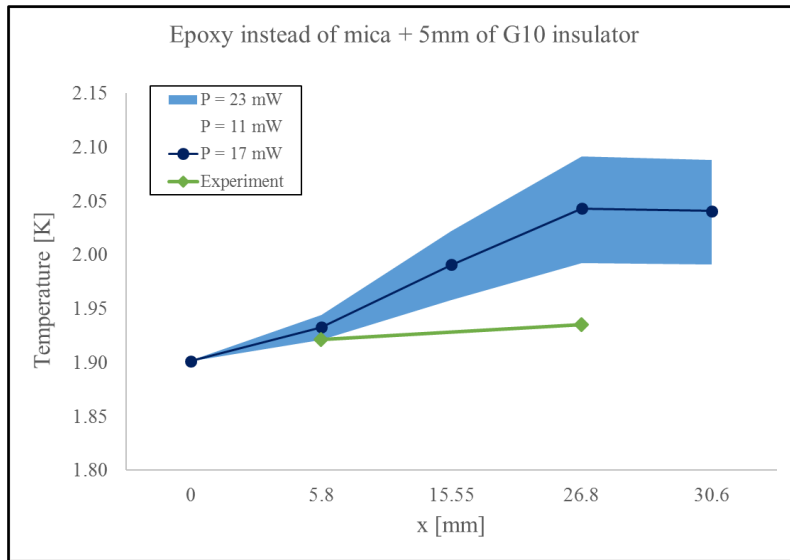


Figure 5.20: Graph representing the variability on the temperature values, as a result of the uncertainties on the input power. The experimental data for the inner layer just "touches" the blue error band.

The plot shows the variability band of the temperature, as a result of the uncertainty on the input power. The blue central line represents the temperature values for the nominal power, namely 17 mW, in 5 points along the domain, and it is confined inside the light blue band. Points are located at the beginning and end of the geometry, in the two conductor layers, and in the middle of the interlayer (Points 1, 4, 9, 14, 17 represented in Fig.5.6). The yellow crosses represent the experimental recordings. The left yellow cross falls inside the band, which means that the simulation, taking the power uncertainty into account, is good enough to get close to the experimental result for the inner layer. What has been described does not happen also in the case of the outer layer, where there is still a 50 mK discrepancy between the experimental point and the lower temperature bound. Let us remind that, nevertheless, we are not getting the "help" of the error bars from the measurements, which we do not know.

It is worth to point out that a 37% of uncertainty on the input power translates to a barely 2.5% variation on the temperature values, even on the adiabatic wall. Fig.5.21 shows the variation both for Point 1 and 17.

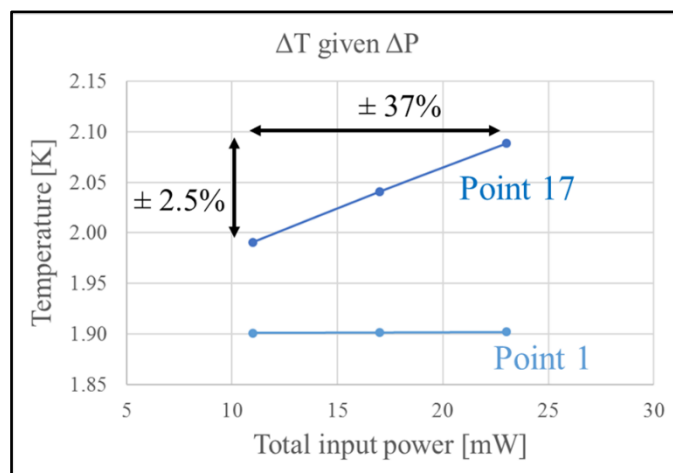


Figure 5.21:  $\Delta T$  variation in response to a  $\Delta P$  uncertainty

The variation is computed using the absolute temperature value at the denominator instead that the temperature variation, which would have been

$$\frac{\Delta T_{upper} - \Delta T_{lower}}{\Delta T_{lower}}, \quad (5.28)$$

and that would have changed completely the result, as it can be seen in the last two columns in Table A.III.5 in Appendix III. Point 1 experiences less variation since it is closer to helium. Let's have also a look at Fig.5.22, to see what happens at the highest input power. Here, 392 mW is the nominal power, while 376 and 408 mW are the lower and upper bounds, defined by the uncertainty at this power regime (5%).

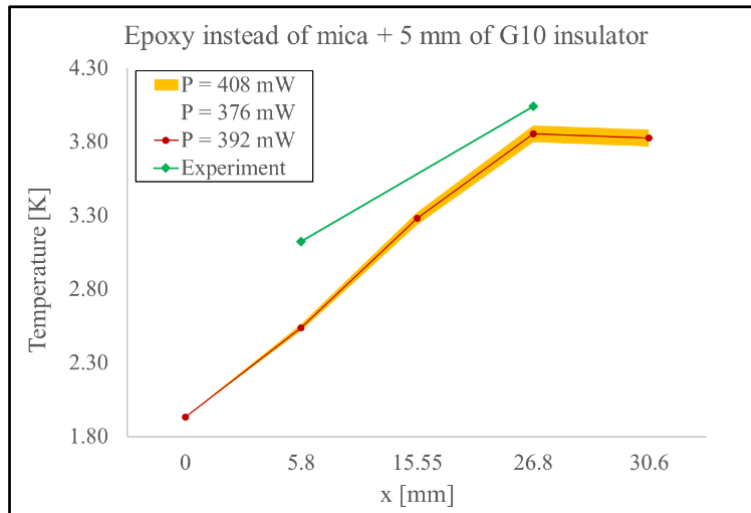


Figure 5.22: Temperature variability for a nominal input power of 392 mW. Both experimental points fall outside the band.

The situation is different from the previous one for two reasons: first, the band is much narrower because the uncertainty is smaller at higher regimes. Second, experimental data lay above the band, rather than below it. In fact, the best case was considered here, which is the model with epoxy instead of mica and with the 5 mm of insulation layer instead of the adiabatic condition. This corresponds to the blue line in Fig.5.19, which crossed the dashed grey line before the last two data points.

It is to be specified that the lines connecting nodes in Figs.5.21 and 5.22 have no physical meaning, since the real profile is different from that, as we know from Figs.5.8 and 5.16.

As a final note, if experimental error bands of temperature measurements were available, it would have been possible to make more careful considerations about the agreement between simulations and the experiment. Being aware of the *resolution*, which is 0.1 mK, does not help to proceed with further discussions.

### 5.15 Heating distribution

Acting on two of the initial assumptions has brought to much better results, and has enabled to get closer to the experimental measurements. The heating distribution was, so far, considered as perfectly uniform across the conductor layers, which is not the most suitable approximation of reality. Some attempts have been made to modify the heating in order to see if it could induce a change both in the temperature distribution along the line and in the general  $T$  vs  $P$  plot.

As a beginning, a single conductor layer was divided in 6 equally spaced sections where each was assigned a different value of input power. Fig.5.23 shows the idea.

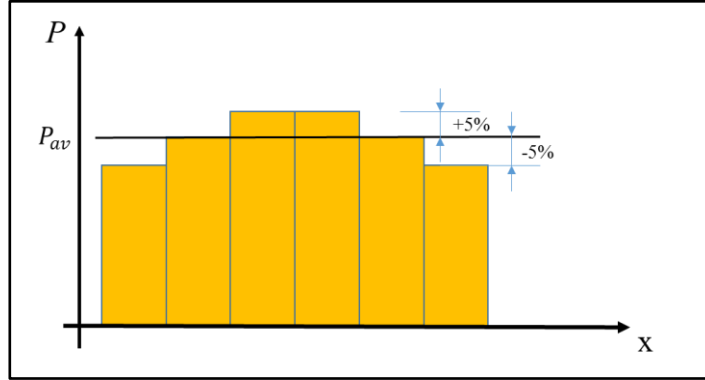


Figure 5.23: Change in the heating power distribution. We name this kind of profile as "A" shaped.

The black line in Fig.5.23 represents the average value, namely the total input power divided by the volume of metallic parts, previously attributed to an entire layer. Assuring the same overall heating, a value 5% less on the borders and 5% higher in the middle was assigned. The same shape was used to assign power steps of  $\pm 10\%$  and  $\pm 20\%$ . Heating distribution was then modified such that heating was higher on the edges and lower in the middle of the conductor, again with a  $\pm 5, 10$ , and  $20\%$  steps, in the so-called "V" shaped profile. This is showed in Fig.5.24.

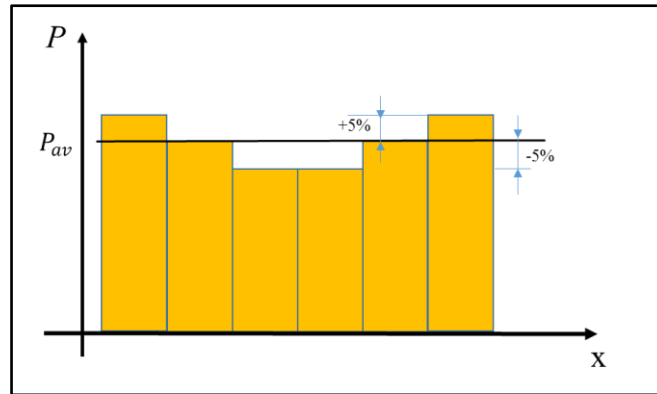
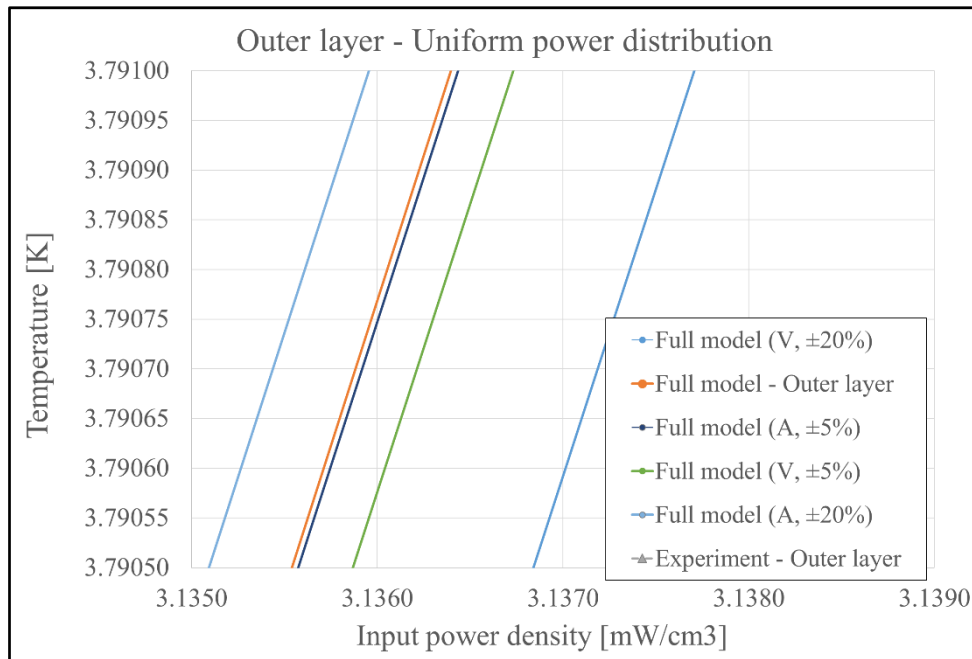


Figure 5.24: "V" shaped profile. Simulations were run again with steps of  $\pm 5, \pm 10$ , and  $\pm 20\%$  with respect to the average input power.

Unfortunately, almost no change in the  $T$  vs  $P$  profile was observed. Fig.5.25 shows what happens in the case of the full model geometry. As always, the orange curve represents the full model, with the initial assumptions.



*Fig.5.25: Results of the implementation of the different heating distributions in the conductor layers. No change, with respect to the uniform case, is observed.*

Fig.5.25 presents a close up in a very narrow region of powers. Very small changes are induced in the profiles, in the order of  $10^{-4}$ , as it can be noticed from the five temperature profiles. A similar behavior was observed also for the epoxy instead of mica case with the addition of 5 mm of G10.

Despite the fact that almost no modification is induced in the heating distribution, this result still tells us something relevant. The model is almost transparent to the shape of the heating distribution inside the conductor layers, since the thermal conductivity of a layer is so high that heat, once deposited, is immediately removed and led to the cable insulation.

An enhancement of the result was obtained when the heat source was kept uniform along a single layer, but a 30% more heat was assigned to the inner one, with the same overall heating in the geometry. The choice of the number is arbitrary and suggested from [49]. However, it helps to reduce the temperature in the outer layer, while it slightly increases it in the inner, without modifying its general trend.

What is shown in Fig.5.26 seems an improvement, but we are still not able to say if such type of heat deposition reflects reality. To be more specific, it does not even change the concavity of the curve. This last point is so important that next section is dedicated to its discussion.

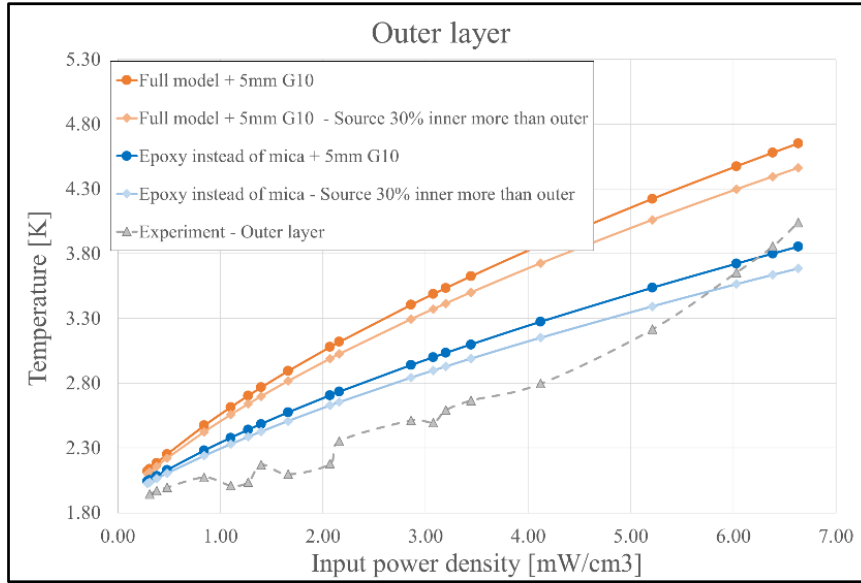


Figure 5.26: Results for the introduction of 30% more heat in the inner conductor layer. Two comparisons were made, using the full model and epoxy instead of mica.

#### 5.16 The sign of the second derivative.

In the very first approach to the 1-D model of the radial line, there was clearly some deviation from the real physical situation, in that the results were too far from the experimental ones. A couple of initial assumptions were modified, acting on the materials in the geometry, and on the boundary conditions. The approach was step-by-step, since it also required time to acquire a clear picture of the physical problem.

Both changes have shown how it is possible to get closer to the experimental points, so that it would be feasible to get even further improvements, for example modifying the heating distribution.

Despite a certain number of factors were taken into account, there is still something that has not been fully understood yet, and which is missing in order to properly reproduce the Cryolab results. This should be related to the difference between the general behavior of the simulation results, from one side, and of the experimental ones, on the other.

The substantial difference is due to the opposite concavity of the curves in a *Temperature vs Input power* plot (Fig.5.10, Fig.5.15) and which is another way to express the sign of the second derivative. As a matter of fact

$$\begin{cases} \frac{d^2T}{dP^2} > 0, & \text{for (all) experiments} \\ \frac{d^2T}{dP^2} < 0, & \text{for (all) simulations} . \end{cases} \quad (5.29)$$

In order to understand this difference, one can start thinking about the materials in the geometry. Those are: epoxy resin, impregnated glass-fiber (G10), Nb<sub>3</sub>Sn and copper. The first three are basically thermal insulators, their thermal conductivity being in the order of magnitude of 10<sup>-2</sup> W/m/K in the 1.9 - 5.0 K range, as Fig.5.27 shows.

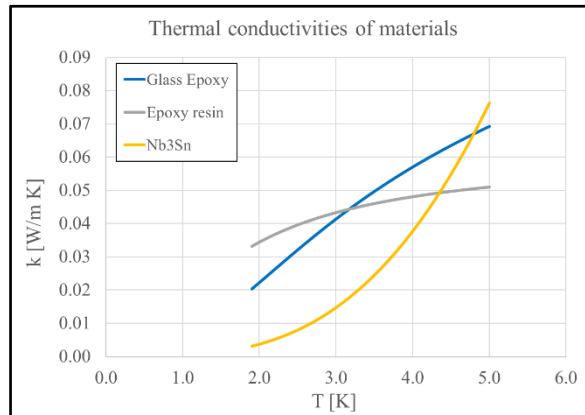


Figure 5.27: Comparison of thermal conductivity of the three types of thermal insulating materials in the 11 T dipole magnets.

Copper, on the other hand, being a thermal (and electrical) conductor, has values of the thermal conductivity which are between 3 and 4 orders of magnitude higher, as Fig.5.28 depicts. Values are extracted in the same range of temperatures considered in Fig.5.27.

Copper shows a linear dependency of thermal conductivity with increasing temperature. It is also interesting to notice that glass-epoxy (G10) and epoxy resin start from much higher values of  $k$  with respect to Nb<sub>3</sub>Sn at 2 K, but then it overtakes the others above 5 K, due to its more rapid increase. This is mainly due to the concavity of  $k$  for Nb<sub>3</sub>Sn, which faces upwards, its second derivative being positive, and which is in contrast with the other two epoxy-made materials. In fact, all materials which are insulating both thermally and electrically, have a similar behavior of  $k$  with  $T$ . Nb<sub>3</sub>Sn, on the other hand is only a thermal insulator, while electrically is a superconductor.

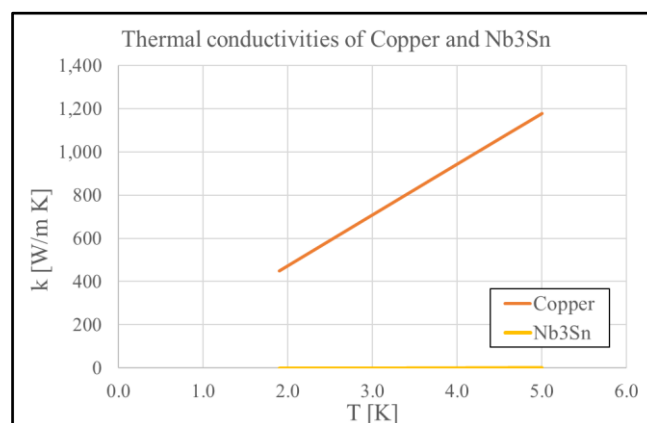


Figure 5.28: Thermal conductivity of copper compared to that of Nb<sub>3</sub>Sn. The difference is 4 orders of magnitude at 2.0 K

This last observation recalls the problem we were trying to face and leaves also an open question. The “Concavity problem” could be the hint of a physical mechanism of heat exchange which was not considered yet.

### 5.17 A possible explanation

Section 4.5 has pointed out that the measurements of the inner center sensor were excluded from the analysis, due to a possible leak of helium inside the sample. Now that a certain number of analyses have been made, it comes out that helium itself could be the cause of the opposite concavity of the experimental and simulation curves. This opinion is supported by micrographs of the coil cross-section, carried out together with the TEMME-MM Section at CERN [45].



Figure 5.29: Delamination in the outer layer quench heater, observed by optical microscopy.

Fig.5.29 shows a close-up of the 11 T dipole cross-section, where delamination occurs between the quench heaters and the outer layer insulation. Defects inside the coil itself are also observed. Let us remind that superfluid helium is characterized by zero viscosity and by an extremely high thermal conductivity, orders of magnitude higher than the best conductor materials. Then, helium would be able to filter inside the coil wherever possible, removing significant amounts of heat.

A possible explanation for this to happen is related to the different heat contraction coefficients between epoxy and the coil, which could originate cracks. These features, even if extremely small, could let helium to seep into them. Further images of the coil cross-section are shown in Fig.A.III.1 in Appendix III.

### 5.18 A resume of the approach.

It is interesting to resume the various approaches undertaken in the present chapter. This would give a proper picture of what has been done and could be the starting point of further considerations. It could be also a useful tool to go back to a specific section with a clearer idea of the procedure in mind. Fig.5.30 depicts the approaches, that could be skimmed from the top, going clockwise.

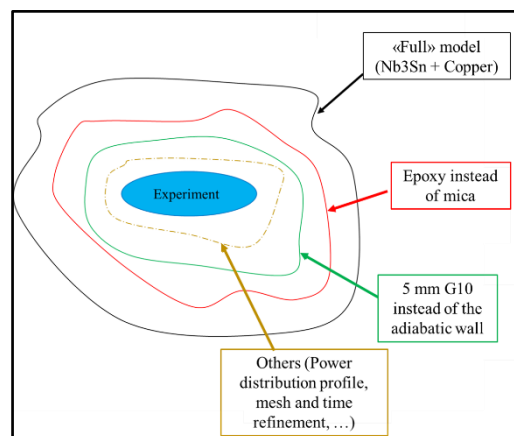


Figure 5.30: The various options tried to get closer to the experimental results.

It shows how, through the modifications made on material elements, boundary conditions and heating distribution in the conductor layer, we got closer to the experimental data.

There are still aspects that need to be checked, like material properties (especially for what concerns mica), and convergence studies both for mesh and time refining.

#### 5.19 AC losses computation.

It is worth to discuss one last point. The ROXIE software [42] was employed to cross-check the AC losses values derived from the calibration procedure, in order to see if they could be reproduced with a simulation. This work was carried out by Eelis Tapani Takala of the MSC Group.

Let us remind that AC losses are made up by three contributions: Inter-strand coupling losses, Inter-filament coupling losses and Persistent losses. This means that currents flow among the strands in a cable, among the filaments in a strand, and even inside filaments. A better description can be found in section 4.3.

Fig.5.32 shows how the total input power resulting from the computations is at least one order of magnitude higher than the experimental values.

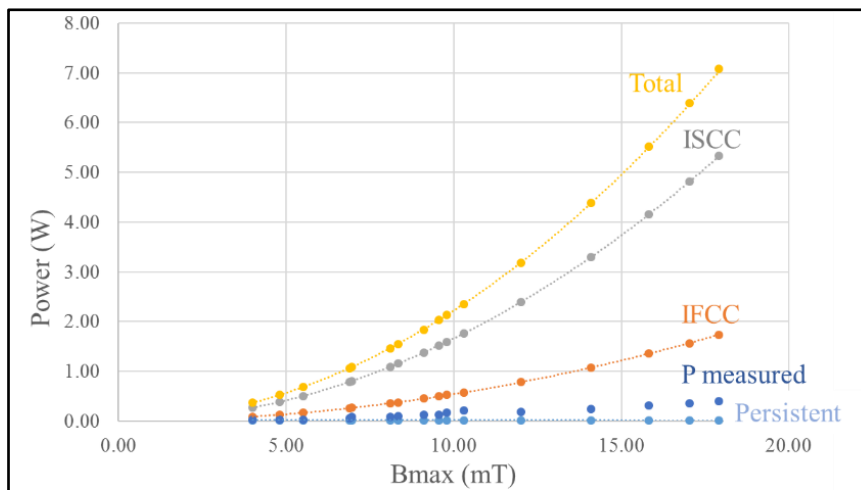


Figure 5.32: AC losses from ROXIE simulation (yellow dots), compared to the experimental values (dark blue dots)

To be more specific, it is the sum of the three contributions already cited, where only persistent currents have a smaller weight than the measured power.

This is a major reason of concern, since these simulations seem to disagree from the experiment also on this point. Further studies were proposed, and it is vital that they shed light on this topic.

## 6. Tests at the SM-18 facility

### 6.1 Introduction

Tests have been carried out at the SM-18 facility to study the behavior of 11 T short dipole samples (length around 2 meters) when subject to heat depositions from quench heaters. These are basically made of strips of stainless-steel, used to induce a uniform heating when a quench is detected in the machine. This is realized in order to avoid high localized temperatures in the magnets, which could be the source of a major damage to the machine. Quench heaters are usually placed on the outer layer of the coil, but some tests were conducted building heaters also in the interlayer.

The present chapter is dedicated to the description of these tests and to their simulation using the 1-D model described in Chapter 5.

### 6.2 Geometry of a quench heater

Quench heaters are instrumented on the outer side of a coil, during the impregnation stage of magnet production. Their geometry, together with the dimension of each material element, is given in Table 6.1.

Material	Dimension
Kapton	50 $\mu\text{m}$
SS strip	25 $\mu\text{m}$
G10	100 $\mu\text{m}$
Kapton	5 x 125 $\mu\text{m}$

Table 6.1: Material layers making up a quench heater.

Fig.6.1 reports another close-up of the outer layer of the cross-section, where one can locate a thin, bright layer immersed in a darker material. That layer is the stainless-steel strip of the quench heater.

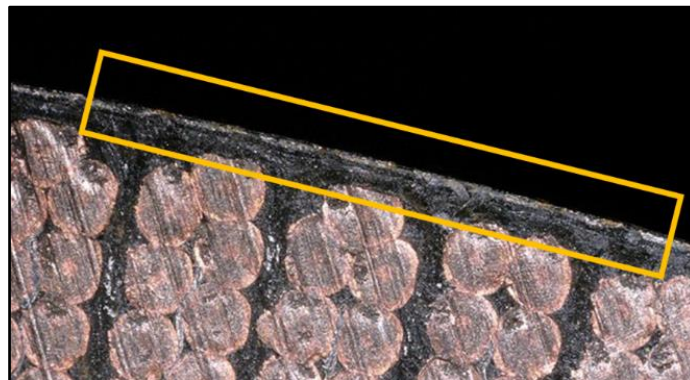


Figure 6.1: Close up of the outer layer, where the SS strip can be distinguished for its brighter colour.

The geometry can be visualized in Fig.6.2, where the first layer of Kapton is directly attached to the last layer of glass-epoxy of the conductor insulation of the outer layer. The only element used to apply heat was the stainless-steel strip, which was 25  $\mu\text{m}$  in thickness. Finally, quench heaters were energized through an RC circuit, experiencing maximum current and heating at the firing moment. The heating time constant was around 27 ms. Further details can be found in Fig.A.III.2 in Appendix III.

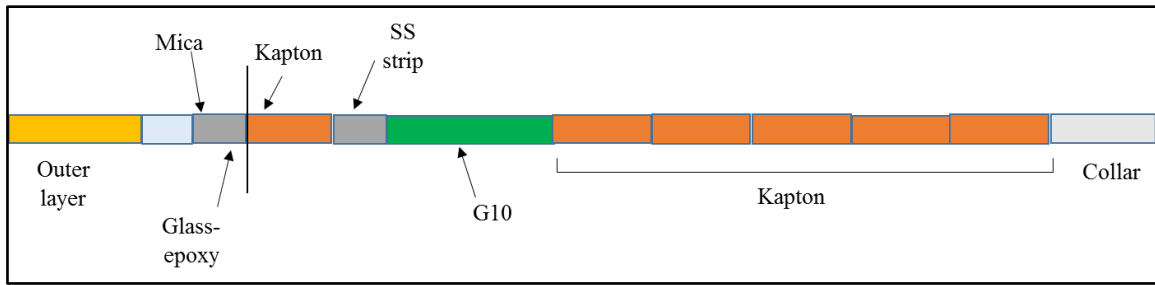


Figure 6.2: Geometry of the outer layer quench heater.

### 6.3 Boundary conditions

Boundary conditions are always extremely important, since they determine both the temperature evolution and the temperature profile in the geometry. The convective condition on the left boundary was kept the same as before, since tests were performed as in real operation. The external Kapton, on the other side of the geometry, is in contact with the non-magnetic collar, which it touches only in a few points. Furthermore, the geometry of the quench heater itself is made in such a way that heat flows only towards the coil, and not to the external collar. This is the reason why an adiabatic condition was assumed, which lets heat to flow towards the inner side of the heater.

### 6.4 Outer layer quench heater tests

Tests with quench heaters were performed to derive the  $T_{CS}$  at given current and magnetic field regimes (see Table A.III.6 in Appendix III). It is worth spending a couple of words about this procedure. Working operation in short coils was made at a certain current and field, as already said. This is indicated as the blue dot in Fig.6.3.

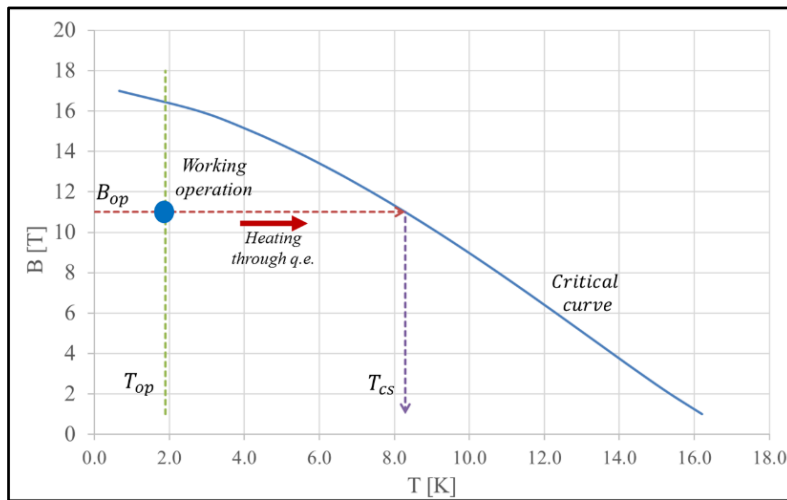


Figure 6.3: Indirect derivation of the  $T_{CS}$

Heating was applied by means of the quench heaters, which were essentially RC circuits. Fig.6.4 shows the top view of the heaters and its electric circuit.

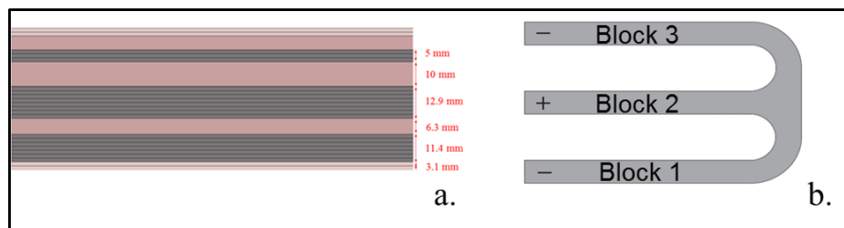


Figure 6.4: Top view (a) and electrical circuit (b) of the interlayer quench heaters.

To be more specific, Block 2 was connected in series with the parallel of Block 1 and 3. Because of the RC circuit, the current and joule heating power had a negative exponential evolution, with time constants being around 50 and 25 ms, respectively (the latter is the half since there is a quadratic exponent of the current in the power formula). Normalized current and power are shown in Fig.6.5.

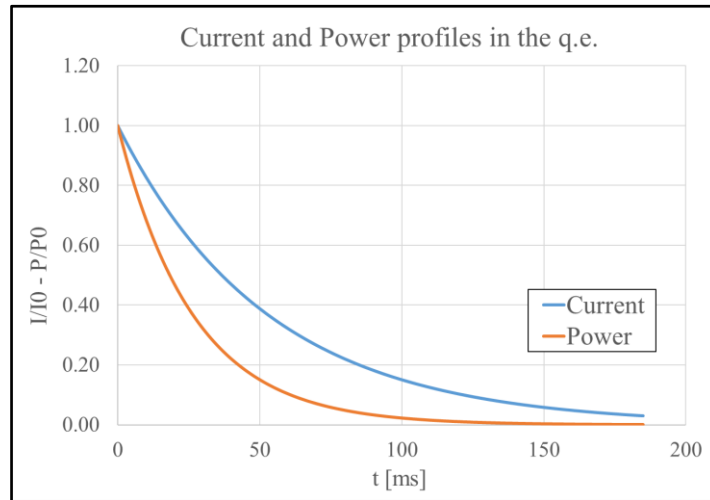


Figure 6.5: Normalized current and power as a function of time.

The heating let the temperature to increase inside the magnet, until quench was initiated. Looking back at Fig.6.3, starting from the “working condition” point, when heat is injected in the system, it follows the red arrow until the critical curve is reached, which means that quench is initiated. Quench was detected using voltage sensors, which are very fast and reliable.

The current sharing temperature was indirectly derived knowing the parametrization for Nb<sub>3</sub>Sn [38], which is represented as the blue curve in Fig.6.3. In such a way, the coil can be used as a *temperature sensor*, since there exists a direct relationship between the critical field and the temperature.

In particular, the  $T_{CS}$  was derived for a point in the coil inside the outer layer and just below the quench heaters. The 1-D model already developed for the Cryolab experiment was properly modified, adding the geometry shown in Fig.6.2, and running simulations in order to compare the data. What was found is quite interesting, and it is shown in Fig.6.6.

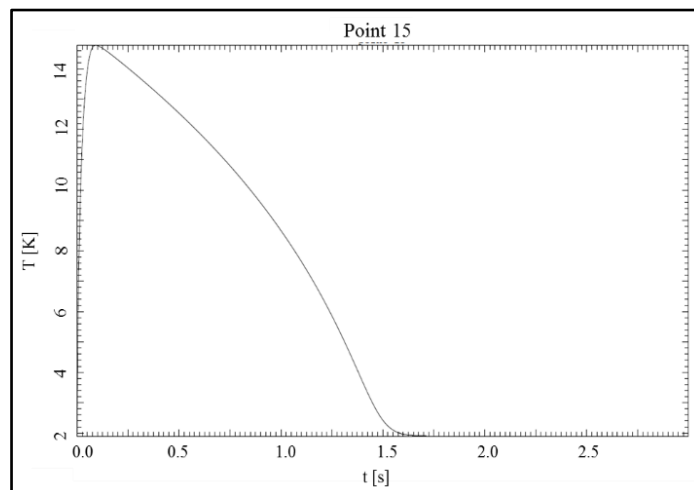


Figure 6.6: Temperature evolution in Point 15 (just below the quench heaters). The maximum temperature reached during the transient was around 14 K.

Fig.6.6 shows the temperature evolution in the point just below the quench heaters. The maximum value was reached just few moments after heat injection and was around 14 K. This was rather different from the Cryolab

experiment, where we were considering temperatures still close the bath itself. We reach much higher temperatures now, and the stainless-steel strip even hit 80 K.

Five tests were carried out, with currents spanning from 1000 to 12000 A and fields from 0.5 to 5.6 T. The HEATER model allows to compute the temperature evolution in the geometry, in response to heat loads.

The heating density was inserted as in the experiment, and was in the order of  $30 \text{ mW/cm}^3$ , so that the maximum temperature reached below the heaters was used to make comparison with the  $T_{CS}$  values (previously determined). Showing results as  $T$  vs  $I$  one obtains Fig.6.7.

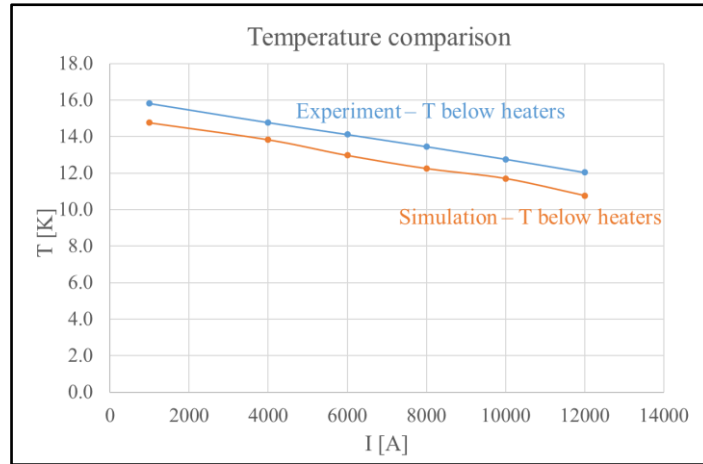


Figure 6.7: Comparison between experiment and simulation for the outer layer quench heater tests.

Differences are around 1 K, but the two curves show a similar trend. The agreement shown in Fig.6.4 encouraged us to use the 1-D model for a last comparison. Further details about this type of tests can be found in Tables A.III.6&7 in Appendix III.

### 6.5 Interlayer quench heater tests.

In real coils for accelerator magnets, quench heaters are usually placed on the outer layer, as it is the case of previous tests. Some specific tests were also made, in which quench heaters were implemented in the interlayer. The interlayer, which is normally made of 500  $\mu\text{m}$  of G10, was replaced by the layers in Table 6.2.

Layer	Dimension
Gl- epoxy	200 $\mu\text{m}$
Mica	40 $\mu\text{m}$
SS strip	20 $\mu\text{m}$
Mica	40 $\mu\text{m}$
Gl.epoxy	200 $\mu\text{m}$

Table 6.2: Layers making up the interlayer quench heater.

They were also instrumented along the whole length of the coil, which was 1.7 m. They covered block 1 (except from the first two cables), 2 and 3. Their configuration is the same as in Fig.6.4.

The three branches were connected in a way that block 2 was in series with the parallel of block 1 and 3. As a result, the heating power densities were distributed with the following proportions: 0.277 in block 1 and 3; 0.447 in block 2. It is easy to verify such values, taking resistances and currents which flowed in each branch, together with their proper dimensions.

Comparisons were made with tests no. 4, 5, and 6 [43], conducted in superfluid helium at 1.9 K. A very

significant difference needs to be pointed out between these tests and the outer quench heaters tests. In the previous case, heaters were energized through an RC circuit, while this time tests were conducted in steady-state conditions.

In cycle 5 only one quadrant was powered, starting from a current of 11.85 kA and a heating regime of 5.9 W/m. A stepwise increase of the heating was adopted, to finally apply 12 W/m. Keeping fixed this last heating value, current was increased to 12.27 kA, at which quench was detected in block no.3. Operation is reported in Fig.6.8.

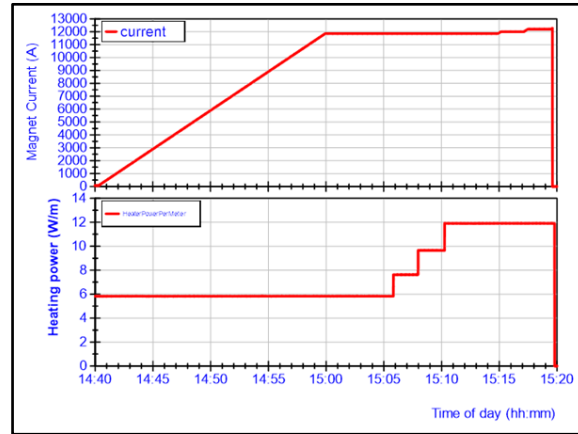


Figure 6.8: Cycle 5 operation

The 1-D model was used to reproduce the experimental results. The geometry was properly modified with layers listed in Table 6.2. Temperature profiles were extracted at steady-state since this corresponded to the operating conditions.

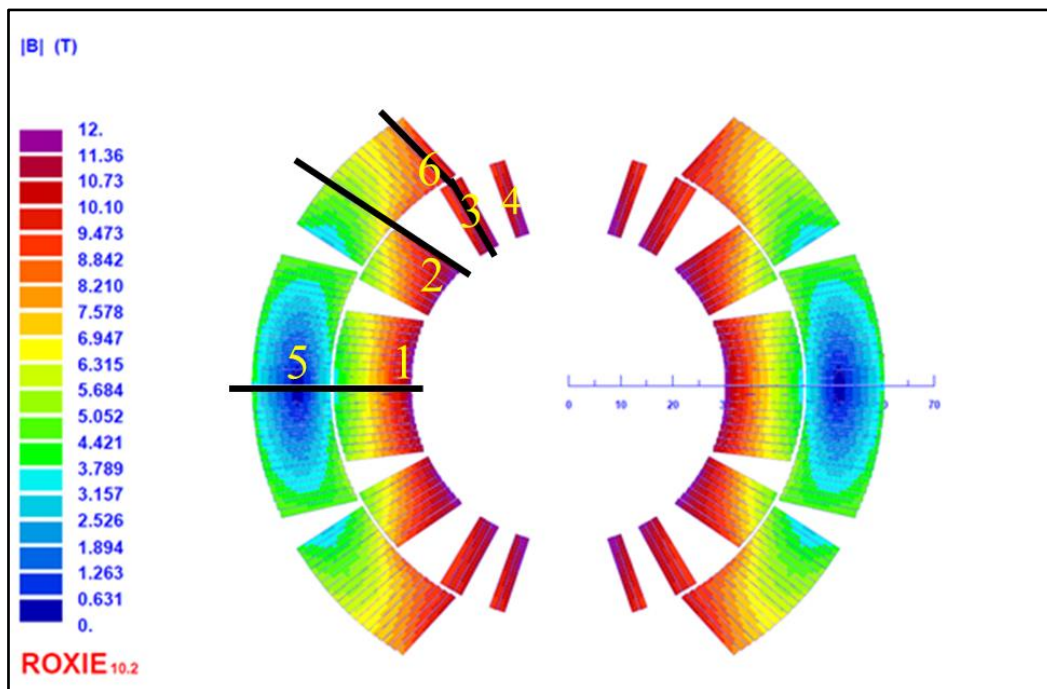


Figure 6.9: Magnetic field map for an 11.85 kA current.  
The black lines are chosen for comparison with simulation results.

Temperatures from the simulations were then compared with  $T_{CS}$  profiles. These were derived starting from the parametrization for  $Nb_3Sn$ , applied at the magnetic field maps computed using the ROXIE software. Something needs to be clarified. The 1-D model is not able to reproduce the major complexity of the 2-D geometry provided by ROXIE. Fig.6.9 shows the magnetic field map for an 11.85 kA current flowing in the conductors, with red and violet colors indicating the regions which experience the highest values of magnetic

fields (around 12 T). Having a closer look at Block 2, the field varies in a very non-uniform way, which means that the  $T_{CS}$  experience a similar behavior.

On the other hand, the 1-D model can return a different profile only among different blocks, due to the heating distribution which is not the same across them. Nevertheless, it is not able to give a profile for different radial lines inside a single block. Then, the most critical lines in the ROXIE model were isolated (the black lines in Fig.6.7), and comparison were made using them.

In cycle no.5 quench was detected in block 3 at 12.27 kA and 12 W/m. Block 3 is made up by three cables, and a line of strands was taken just in the middle of the block, continuing in block no.6. Fig. 6.10 shows the magnetic field across the line (yellow), the resulting  $T_{CS}$  profile (violet) and the temperature profile from the simulation (green). The origin of the axis,  $x = 0$ , is placed on the inner side of the coil.

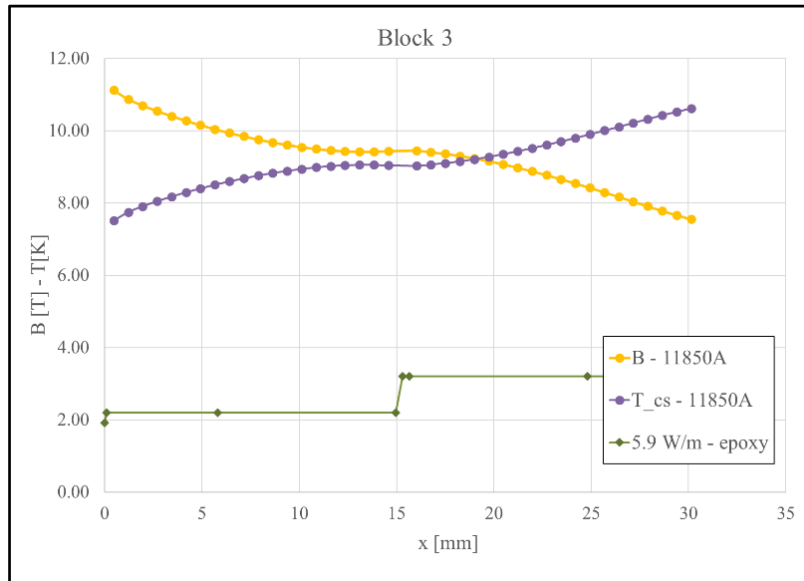


Figure 6.10: Field and Current sharing temperature profiles in a line in Block 3 and 6.

The magnetic field remains quite high all along the line, passing from a maximum of 12 T on the inner side of the magnet, to a minimum of 8 T on the outer layer. In fact, block 3 is very close to the coil axis, and thus sees all the highest magnetic fluxes, with lines oriented almost parallel to its cables. The resulting  $T_{CS}$  profile has

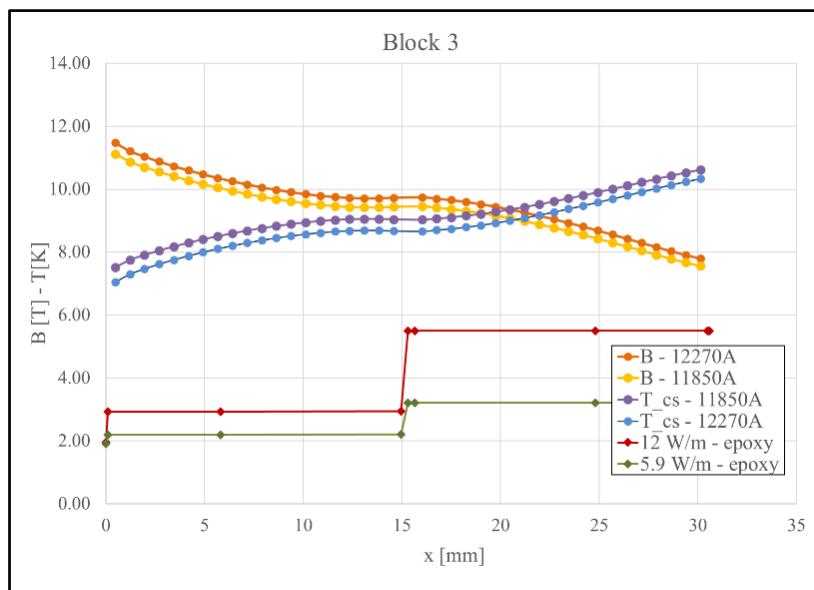


Figure 6.11: Temperature and Field profiles at quench values of heating and current. The dark red curve stands for the simulation at 12 W/m, no degradation.

an opposite behavior, going up as  $B$  goes down. The third curve is the temperature profile from the HEATER simulation, which is much lower than the  $T_{cs}$ . This means that no quench is predicted at this regime, which is in agreement with the simulations, being just the starting point of the test. Going up to the quench values of current and heating, one gets other curves, added in Fig.6.11.

Fig.6.11 depicts the temperature profile for a heating of 12 W/m, which is substantially higher than the previous one, 5.9 W/m. The new curve for the magnetic field is the orange, and its corresponding  $T_{cs}$  is the light blue curve. Apparently, it is not possible to explain the quench initiation, since the temperature curves are quite distant from each other. The only way to make the curve to cross, thus obtaining a quench, is to act on the degradation value. This factor is better explained below.

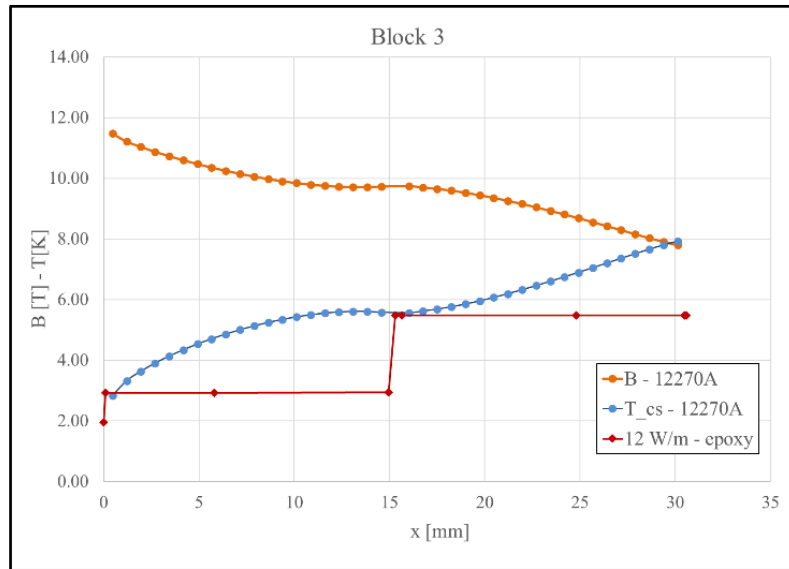


Figure 6.12: Current sharing temperature profile for 12.27 kA when degradation is set to 0.49. It crosses the temperature profile given in the simulation.

Fig.6.12 shows only the plot of the magnetic field and of the current sharing temperature correspondent to a 12.27 kA current and a degradation factor of 0.49. In fact, the degradation was repeatedly changed until the contact of  $T$  and  $T_{cs}$  profile was realized, so that 0.49 was the first value to mark the transition. The red curve shows the temperature profile in the geometry for a heating of 12 W/m, as in Fig.6.11. It is very interesting to note that the two profiles cross in correspondence with the inner layer, which precisely where it was detected in the measurements.

Similar results can be derived analyzing cycles 4 and 6. Cycle 4 was characterized by an initial input power of 5.9 W/m, with a ramp-up of 10 A/s to reach 12.85 kA. A step to 7.7 W/m induced quench within a few seconds. Cycle 6 was operated at 11.85 kA and with a heating of 10.8 W/m, stable for one minute; a step to 11.9 W/m caused quench initiation. Quench was detected in block 1 in both cases, particularly on the middle plane turn. Let's have a look at Fig.6.13.

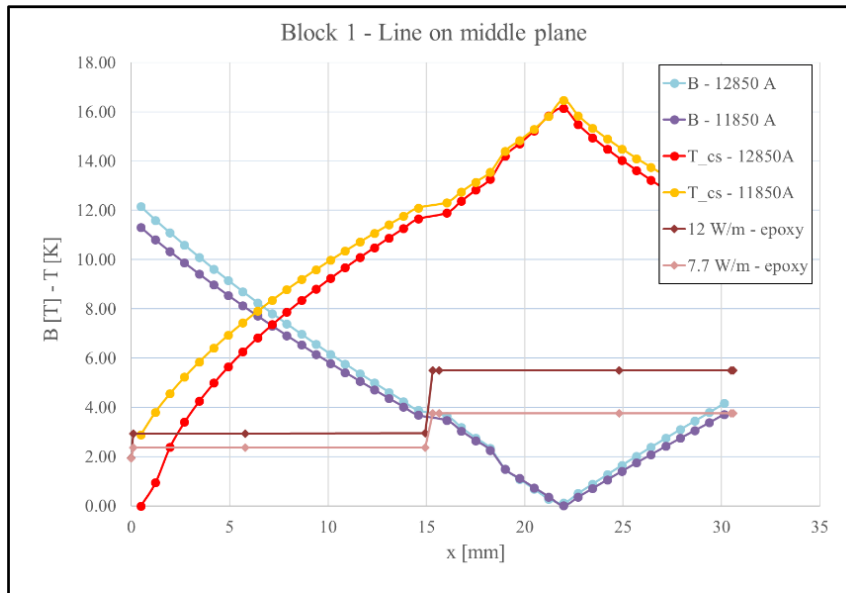


Figure 6.13: Field, Current sharing temperature and Temperature profiles for Block 1.

Where one can see the much bigger difference in the profile of the magnetic field, relatively to the previous case. In fact, the field has a starting value of 12 T on the inner side of the coil, then goes down very quickly and finally touches the zero on the outer layer. The behavior of the  $T_{CS}$  is its exact reflection, with no chance that quench could happen in the outer layer. At a first glance, since the outer layer is the warmer part of the geometry, one can think that the outer layer itself should be the one to quench more easily. Nevertheless, it is the inner layer which is in the most critical situation. In fact, it experiences the higher fields, which together with the high current densities, cause the  $T$  cross the  $T_{CS}$  profile.

Fig.6.13 shows the conditions both for cycles 4 and 6. To be more specific, the red curve, which belongs to the current sharing temperature at 12.85 kA, is to be compared with the pink one, correspondent to the temperature profile at 7.7 W/m (cycle 4). The yellow curve, of the  $T_{CS}$  at 11.85 kA, is “coupled” with the dark red curve of the  $T$  profile at 12 W/m. In order to obtain the contact between the two profiles in the most “difficult” situation, which was at 11.85 kA, the degradation factor had to be set to 0.49, as it happened for Block 3.

It is also interesting to have a look at Block 2, where the heating density was slightly higher than Block 1 and 3.

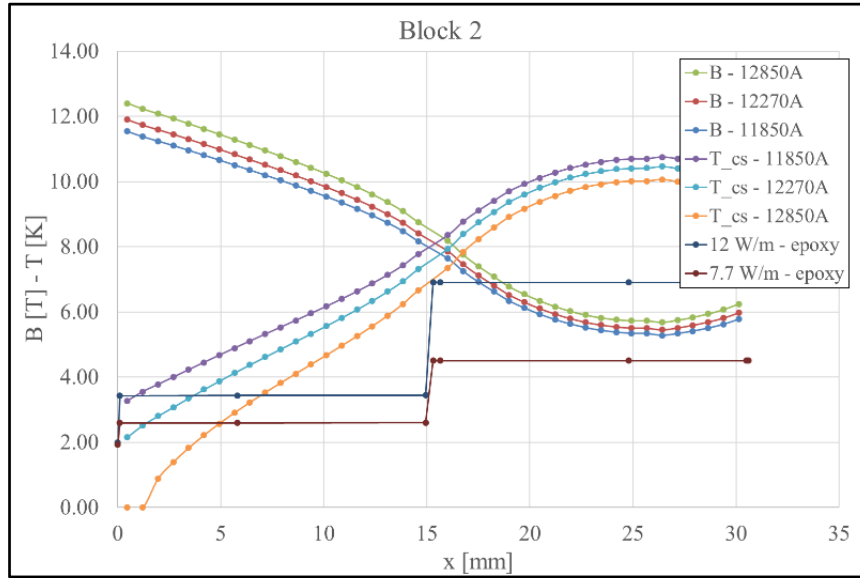


Figure 6.14: Field and Current sharing temperature for all the three current regimes. Temperature profiles are at 7.7 and 12 W/m. Quench is predicted only on the inner layer.

Fig.6.14 shows the field and current sharing temperature profiles for all the three current regimes of interest, 11.85, 12.27, and 12.85 kA. The field had an intermediate behavior with respect to Block 1 and 3, going from a maximum of 12 to a minimum of 5-6 T. Two temperature profiles are presented, both for 7.7 and 12 W/m, which are slightly higher than before, due to the higher heating in this specific block (0.447 against 0.277 of the other two). To let the two profiles cross in the most critical situation, which was again at 11.85 kA, a value equal to 0.50 of the degradation was set, which is very close to those already expressed. Quench was predicted to happen only in the inner layer, even at the highest current and heating regime, namely 12.85 kA and 12 W/m.

Two common points can be noticed in the comparison of the three blocks. The first, quench location, is rather encouraging, since results show that the 1-D model can predict where quench actually happens. The second, being the degradation factor, on the other hand, needs further analysis. Degradation is the fraction of filaments which still carry current. It plays an important role both in the computation of the critical current density,  $J_c$ , and of the current sharing temperature,  $T_{cs}$ . The results show that this factor should be around 0.5 in order to explain the quench heater tests. This means, by definition, that just 50% percent of the filaments carry current, which is something rather surprising, indeed.

Let's try now with another approach. One can define an equivalent value of the strain, let's call it  $\epsilon_{eq}$ , at which the  $T_{cs}$  has the same behavior as in Figs. from 6.11 to 6.13. In fact, setting the degradation to 1 (no broken filaments), the drop in the  $T_{cs}$  can also be explained just using the strain.

Some trials, where the strain value was changed in order to get the same  $T_{cs}$  curves as for the previous case (with a degradation of 0.49) have shown that this value is around -0.75%. To be more specific, the value is the composition of the normal strain in Rutherford cables, which is -0.2%, and of the degradation given by the transverse pressure, which in these cables is up to 150 MPa.

In [39], the impact of the transverse pressure on the reduction of the critical current,  $I_c$ , and of the upper critical field,  $B_{c2}$ , in Nb<sub>3</sub>Sn sub-cables for the Fresca2 facility is studied. Fig.6.15 shows some measurements of the  $B_{c2}$  reduction, at 4.3 K, as a function of different values of the transverse pressure, from 80 to 160 MPa [39].

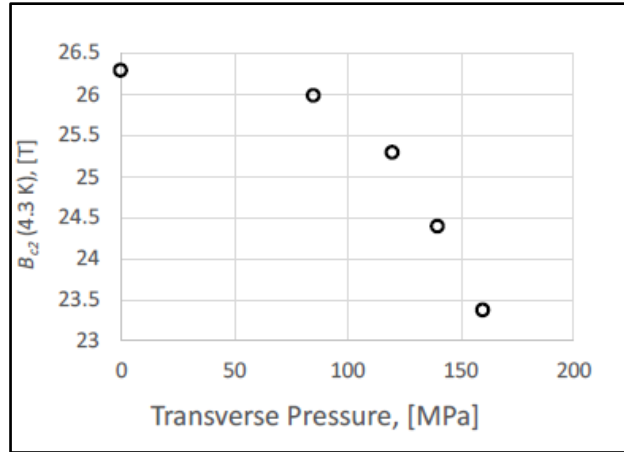


Figure 6.13:  $B_{c2}$  reduction for Rutherford cables subject to transverse pressure.

At a transverse load of 150 MPa,  $B_{c2}$  decreases from 26.3 to 23.7 T, with a 36% reduction of the critical current in the cable (at 4.3 K and 12.84 T). Using the parametrization for  $Nb_3Sn$  [38] one can easily find that the strain that would give the same reduction of the upper critical field would be equal to -0.55%.

The value of the  $\varepsilon_{eq}$  that derives from the comparison of  $T_{cs}$  and  $T$  profiles and that allows to make them cross in the inner layer was, on the other hand, -0.75%. These two values are far from each other, and no other contribution to the total strain seems to be able to cover the spread between them.

The results presented in this Chapter have shown that the 1-D approximation is able to explain the interlayer quench heater tests only assuming a value of degradation, or of equivalent strain, which is higher than expected. In fact, the strain required to match the experimental data is still a 0.2% higher than the one derived using data in [39] for tests carried out on  $Nb_3Sn$  cable at CERN. Nevertheless, it is worth saying that these are still preliminary results, and that further investigations could bring to match the results from experiments and simulations.

## 7. Conclusion

The object of the present study has been the analysis of the thermal behavior of the dipole magnet for the High-Luminosity project of the LHC, carried out at the European Council for Nuclear Research (CERN). The aim of the project is to increase the luminosity of the accelerator of a factor ten by the year 2025. A key element to this achievement is the employment of magnetic fields up to 12 T, a considerable enhancement compared to the 8 T of the present machine. This will be realized through a new generation of superconducting magnets, which employ Nb<sub>3</sub>Sn, a material which was never used before for the construction of accelerator magnets.

The different properties of this material with respect to Nb-Ti, which was used to build all the magnets for the present LHC, requires careful studies before installing new components inside the accelerator. One of the most delicate features of superconducting magnets regards the thermal part, that is the behavior of coils in response to heat depositions. In fact, these can trigger a quench, which is a highly undesirable phenomenon during magnet operation. From here derives the importance of a detailed description of the magnet response to heat loads. The 11 T dipole was modeled by means of a 1-D simulation, considering a radial line laying on the middle plane of an aperture of the magnet. The model characteristics, as the dimensions of its various parts, material properties and boundary conditions, have been presented in detail.

An experiment carried out at the cryogenic laboratory was aimed to define the temperature response of a dipole sample subject to AC losses. The first application of the 1-D model was to reproduce the experimental results, for all the power regimes used in the experiment. The comparison has shown, in the first place, a certain discrepancy between the experiment and the simulation and forced to undertake an important process of revision. This brought to a reconsideration of the role played by Mica, an electrical insulator of the cables which, due to the impregnation with epoxy resin, does not seem to be relevant from a thermal perspective.

Other assumptions, as a potential ununiform distribution of power between the two layers of conductors have been explored, but they require more detailed studies to understand if they represent the actual situation.

Despite a significant enhancement was achieved with respect to the first comparison, an unclear aspect also remains, about the opposite concavity of the experimental and simulation curves in the temperature versus power diagram. This suggests the presence of a possible leak of helium in the sample, which is something that would certainly deserve further analyses.

The 1-D simulation was then applied to reproduce quench tests carried out on a short model of the 11 T dipole at CERN magnet test facility, SM-18. In this case, magnets were subject to heat depositions from quench heaters, placed both on the outer radius of the magnet, as in the final configuration, and in the space between the two conductor layers. The purpose of such tests was to use magnets as temperature probes, knowing the initial operating conditions of temperature and magnetic field, together with the critical curves of the superconducting material. The model was conveniently adapted to take the geometry and operating conditions of quench heaters into account. Even though results are still preliminary to some extent, various analyses have shown that the model is able to reproduce the initiation of the quench phenomenon in the same locations identified in the measurements, when a degradation of about half of the filaments in the cables is considered.

## Acknowledgement

There are several persons that I would like to thank for the writing of this text. My first thought goes to Professor Marco Breschi who, about one year ago, welcomed me in the applied superconductivity group of the Engineering school in Bologna. The experience at CERN, from which comes all the work I explained in these pages, is because he trusted me, and I am extremely grateful to him for that.

A sincere sense of gratitude goes to Marco Bianchi, who followed me during my first internship on superconductivity, and who has always given me so much help and kindness.

It is my desire to thank my supervisors at CERN, Arnaud Devred and Luca Bottura. They are outstanding scientists, and I have been truly inspired by them and by their way of doing science.

I shared plenty of discussions with Enrico Felcini, who always found time for my questions and doubts, and supported me throughout the whole period of my stage. He has also been a very good friend of mine, and I am extremely happy for that.

A special mention needs to be pronounced for the colleagues, and most of all, friends I met, who get interested in my work and gave me precious advices and encouragement: Alexandre Mehdi Louzguiti, Vera Korchevnyuk, Maxime Romain Matras, Alessandro Cattabiani, Nora Grada, Algirdas Baskys, Gianluca De Marzi, Andrea García Alonso, Christopher Brian Segal, Konstantina Konstatopoulou, Iole Falorio, and Christian Barth. I consider myself very lucky to have shared time with these wonderful people. Each and every one of them has made this experience unforgettable and unique.

Un grazie di cuore va anche ai miei amici in Italia, con cui sono cresciuto assieme: Federico Ravagli, Cesare Ceccarelli, Alessia Teresa Accoto, Caterina Pezzi, Niccolò Cotta Ramusino, Riccardo Strada, Alessandra Zecchini, Federico Faccini e Riccardo Bevoni. Non può certo mancare Mattia Venturini, con cui ho condiviso una vera esperienza di crescita nel “nostro” appartamento di Bologna.

Vorrei citare i miei compagni di facoltà, con cui ho condiviso tante lezioni sui banchi, ma anche tanti bei momenti al di fuori di essi: Davide Baraldi, Francesco Montecchi, Luca Boselli, Giulia Laghi, Michela Fabbri, Davide Laghi, Francesco Marastoni, Nicola Chiarotti, Paolo Benati e Virginia Amato.

Una citazione particolare va alla persona che mi ha convinto a studiare Ingegneria Energetica e che è sempre stata una vera fonte di ispirazione in questi anni: Stella Spazzoli.

Tutto ciò non sarebbe stato possibile senza le persone che mi hanno visto crescere e che mi hanno dato supporto durante tutta la mia vita: un grazie dal più profondo del cuore a Roberto e a mia mamma.

E, anche se non hanno potuto vedere questa tesi compiuta, la mia dedica va alla dottoressa Graziella Sarti, che ha tanto creduto in me, e a mia nonna Maria, che mi ha donato tutta la sua dolcezza.

La presenza di tutte queste persone nella mia vita mi ha sempre dato motivazione e coraggio nel raggiungere gli obiettivi che mi sono posto davanti, e continuerà a farlo anche in futuro. Grazie di esserci.

## Appendix I.

### Effective thermal conductivity of $Nb_3Sn$ impregnated Rutherford cables

#### A.I.1 Rutherford cables

A Rutherford cable is a flat cable where superconducting strands are twisted in order to form a rectangular shape made up of two layers of overlapped strands (see Fig.A.I.1). In Nb-Ti cables, like the ones used in the LHC, strands are just wound together, without involving any other material. Helium, the superfluid liquid coolant, thanks to its extremely low viscosity, is then able to fill the small interstices between the various strands and to remove heat with very fast time scales.

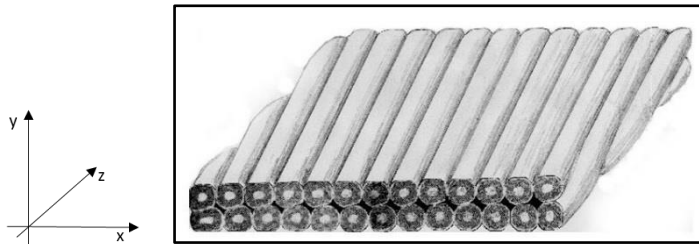


Fig. A.I.1: Twisted strands in a Rutherford cable.  
Cortesy: Professor M. Wilson

In  $Nb_3Sn$  cables, on the other hand, which will be used for the High-luminosity project of the LHC, a stainless-steel core layer is interposed between the two layers of strands to cut coupling currents and, due to the brittleness of the intermetallic compound, they are also immersed in an epoxy-resin matrix to prevent strands from moving. Thermal properties will then be much different from cables made of Nb-Ti, and it is worth studying it. An evaluation of effective thermal conductivity of an impregnated Rutherford cable in the three directions is computed here which takes twisting into account. Comparison with experimental data will be also presented.

Table A.I.1 reports the dimensions of a  $Nb_3Sn$  epoxy-impregnated cable for the 11 T dipole.

11 T Dipole cable parameters	
Number of strands	40
Strand diameter (after reaction)	0.714 mm
SS core thickness	14.65 mm
SS core width	25 $\mu\text{m}$
Bare cable thickness, $t$	14.85 mm
Bare cable width, $w$	1.307 mm
Insulation width	100 $\mu\text{m}$
Total cable thickness, $t_{\text{tot}}$	15.05 mm
Total cable width, $w_{\text{tot}}$	1.507 mm

Table A.I.3: Cable parameters for the 11 T Dipole.

The shape of a strand is a circle but becomes an ellipse in the cross-section normal to the cable. In fact, strands are tilted relatively to the cable main direction, as seen in Fig.A.I.1. It is also important to notice that during the manufacturing process, the cable is pressed on its normal directions, so the resulting shape of a strand can be considered an octagon, as can be seen from photographs (Fig.A.I.2).

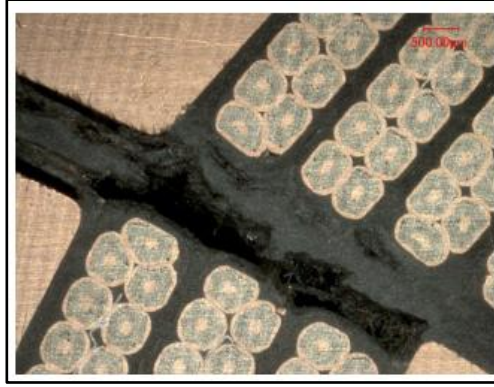


Figure A.I.2: Close-up of the magnet cross section, in the region between the inner and outer layer.

To start our consideration about the effective thermal conductivity of the cable, some assumptions will now be made, and for that it will be helpful to look at Fig.A.I.3.

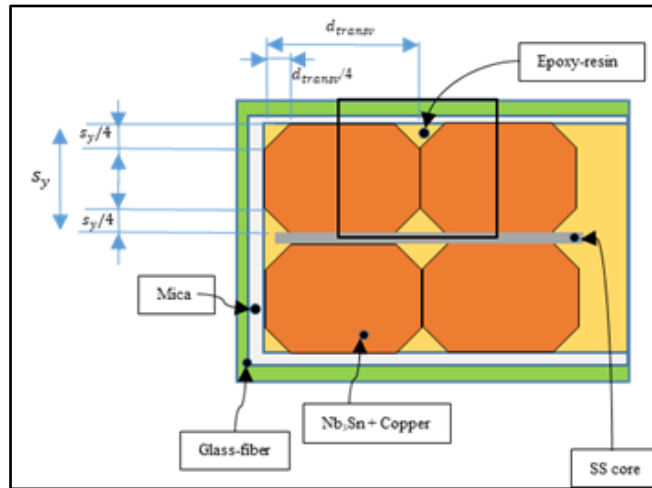


Fig. A.I.3: Part of a cable cross section. Only 2 of the 22 couples of strands in the cross section are shown. The black rectangle represents the unit cell for the x-axis, which will be discussed later.

#### A.I.2 Assumptions of the study and definitions

The assumptions are: 1) The strands are of octagonal shape, as already mentioned. 2) A strand is made up by a homogeneous material, with properties that are averaged between that of copper and the superconductor, taken with their relative area proportions. In case of the 11 T Dipole, the ratio Cu/non-Cu is 1.15. 3) The external part of a strand is made of copper, so that the contact between two strands is Cu/Cu, while between strands and insulation is Cu/Epoxy, due to impregnation. 4) The insulation is made of glass-fiber and mica, as in the real cable.

The computation of the thermal conductivity starts along the y-axis, taking a line that crosses the cable thickness. The approach is to compute the total cable resistance over the line, and then convert it into an effective thermal conductivity. The thermal resistance is defined, in analogy to the electrical case as

$$R_{th} = \frac{\Delta T}{\dot{Q}} \quad \left[ \frac{K}{W} \right], \quad (\text{A.I.1})$$

where  $\Delta T$  plays the same role as the  $\Delta V$ , and  $\dot{Q}$  as the current  $I$ .

The thermal conductivity is expressed as:

$$k = \frac{\dot{Q} * L}{A * \Delta T} \quad \left[ \frac{W}{m K} \right], \quad (\text{A.I.2})$$

or, in turn

$$k = \frac{L}{A * R_{th}}. \quad (\text{A.I.3})$$

Without taking the area into account, the thermal resistance can also be written as

$$R'_{th} = \frac{\Delta T}{q} \quad \left[ \frac{K m^2}{W} \right], \quad (\text{A.I.4})$$

so that  $R_{th}$  is  $R'_{th}$  per unit area

$$R_{th} = \frac{R'_{th}}{A}. \quad (\text{A.I.5})$$

This last definition enables to use a very practical formula for the computation of  $R'_{th}$

$$R'_{th} = \frac{s}{k}, \quad (\text{A.I.6})$$

where  $s$  is the thickness of the layer (the same as  $L$  in Fig.A.I.4).

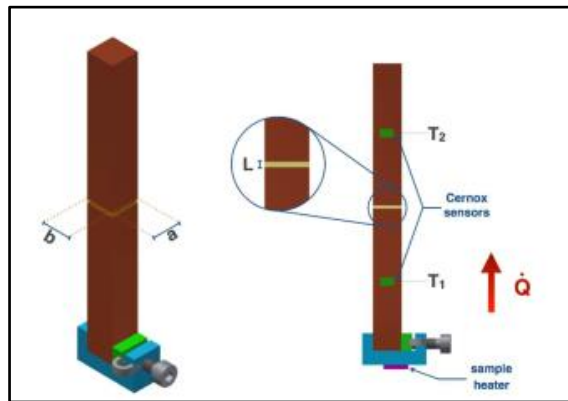


Figure A.I.4: Experimental set-up for thermal conductivity measurements.

Physical units are in agreement. The thermal resistances will be computed reversing expression (A.I.6)

$$k = \frac{s}{R'_{th}}. \quad (\text{A.I.7})$$

The reason why  $R'_{th}$  has been introduced is that the only quantities known are usually the layer thicknesses and their thermal conductivity. A short example could be useful to understand why  $R_{th}$  and  $R'_{th}$  can be either used. Let's suppose to have 2 thermal resistances, connected in series, so that

$$R_{th} = R_{th,1} + R_{th,2} , \quad (\text{A.I.8})$$

It can be written

$$R_{th} = \frac{\Delta T_1}{\dot{Q}} + \frac{\Delta T_2}{\dot{Q}} = \frac{\Delta T_1}{q * A} + \frac{\Delta T_2}{q * A} = \frac{1}{A} * \left( \frac{\Delta T_1}{q} + \frac{\Delta T_2}{q} \right) . \quad (\text{A.I.9})$$

Then,

$$R_{th} = \frac{1}{A} * (R'_{th,1} + R'_{th,2}) = \frac{1}{A} * R'_{th} . \quad (\text{A.I.10})$$

Except for the factor  $A$ , which is the area normal to the direction where thermal conductivity are computed, using  $R_{th}$  or  $R'_{th}$  makes no difference. If the area assumes the same value for both the resistances, as usually does for layers of insulator in series, it can be gathered in front of the expression, and then be neglected.

The formula of the electrical resistance:

$$R_{el} = \rho \frac{l}{A} \quad [\Omega] , \quad (\text{A.I.11})$$

also contains the area of the surface normal to the direction where the current flows.

### A.I.3 Local and global reference systems

It is of great importance to point out that the computations of the effective thermal conductivity will be made in the reference system of a strand, named "local" in Fig.A.I.5.

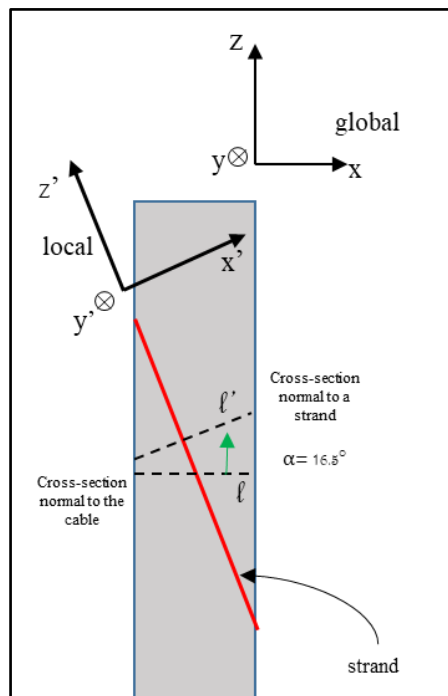


Figure A.I.5: Local and global reference systems, the first attached to a strand, the second to the cable main direction

This will enable to perform much easier calculations, and then “pass” to the global reference system by means of a tensor rotation.

When one considers a section normal to the cable, 40 strands can be counted, which are used to manufacture the cable itself. This section is indicated as  $l$  in Fig.A.I.5. Even if the cross-section of a strand is a circle, of diameter equal to 0.714 mm (after reaction), the shape along line  $l$  is an ellipse, with the major axis

$$d_{transv} = \frac{d}{\cos(\alpha)} = \frac{0.714 \text{ mm}}{\cos(16.5^\circ)} = 0.745 \text{ mm} , \quad (\text{A.I.12})$$

Multiplying this dimension by the number of strands on a single line

$$d_{transv} * 20 = 14.90 \cong 14.85 \text{ mm} = t \quad (\text{A.I.13})$$

one gets approximately the bare cable thickness (after action). This confirms also with computations that there are 20 strands in the normal cross-section. In the reference system of a strand, on the contrary, the diameter is 0.714 mm, so that the number of strands needs to be a little bit higher to fit the dimensions, being equal to 44. In fact, multiplying by 22, number of strands on a single row

$$d * 22 = 15.71 \text{ mm} \quad (\text{A.I.14})$$

A length similar to the line in the tilted cross-section,  $l'$ , is obtained

$$l' = \frac{14.85 \text{ mm}}{\cos(16.5^\circ)} = 15.49 \text{ mm} , \quad (\text{A.I.15})$$

This means that on line  $l$ , there are 20 strands, while one can enumerate 22 on  $l'$ , since 22 strands have to be taken into account to match the cable dimensions on that line. Table A.I.2. resumes the two sections.

Type of section - Normal to	Name
Strands	$l'$
Cable	$l$

Table A.I.2: Sections orthogonal to strands and the cable, respectively.

The dimension of a strand along the  $y=y'$  axis is, again, different from the simple strand diameter. In fact, the bare cable width is 1.307 mm; subtracting the core thickness and dividing by two (the number of strand layers), one obtains

$$s_y = \frac{1.307 - 0.025}{2} = 0.641 \text{ mm} , \quad (\text{A.I.16})$$

which will be used in the proceeding. Table A.I.3 resumes the strand dimensions in the two reference systems.

Strand dimensions	
Along x	0.745 mm
Along x'	0.714 mm
Along y=y'	0.641 mm

Table A.I.3: Strand dimensions in the two reference systems.

#### A.I.4. Computations

##### A.I.4.1. Thermal conductivity along the $y'$ axis

Starting from the  $y'$  axis, it is possible to identify 9 thermal resistances, showed in a horizontal projection, starting to the left (upside) and going to the right (downside), as FigA.I.6 depicts.

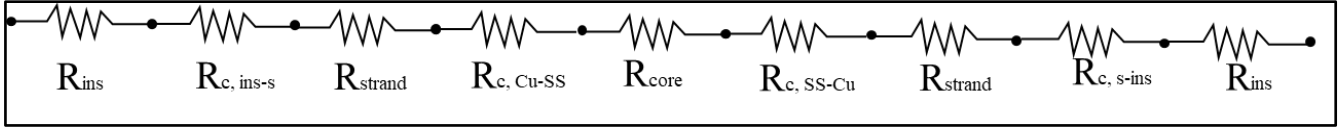


Figure A.I.6: Projection of the thermal resistances along the  $y$ -axis

which is

$$R'_{tot} = R'_{ins} + R'_{c,Ins-Cu} + R'_{strand} + R'_{c,Cu-SS} + R'_{core} + R'_{c,SS-Cu} + R'_{strand} + R'_{c,Cu-Ins} + R'_{ins} \quad (A.I.17)$$

rewritten

$$R'_{tot} = 2R'_{ins} + 2R'_{c,Ins-Cu} + 2R'_{c,Cu-SS} + 2R'_{strand} + R'_{core} \quad (A.I.18)$$

where

$$R'_{ins} = R'_{glass-fiber} + R'_{mica} \quad (A.I.19)$$

To compute the thermal resistances of layers, the definition itself (A.I.6) is used, where dimensions of strands and of insulation are referred to the tilted section.

Dimension	Value
$d_s$	0.714 mm
$s_{glass-epoxy,y}$	50 $\mu\text{m}$
$s_{mica,y}$	50 $\mu\text{m}$
$s_{epoxy,y}$ (equivalent) = $d/4$	180 $\mu\text{m}$
$s_{core,y}$	25 $\mu\text{m}$
$s_{strand,y} = (w - s_{core,y})/2$	0.641 mm

Table A.I.4: Dimensions to be used in the computation.

While

Material	Thermal conductivity (at 1.9 K)
Glass-epoxy	$2.04 \cdot 10^{-2}$ W/m K
Mica	$6 \cdot 10^{-3}$ W/m K
Epoxy resin	$3.32 \cdot 10^{-2}$ W/m K
Stainless steel	$9.64 \cdot 10^{-2}$ W/m K

Table A.I.5: Thermal conductivity of the 4 materials involved in the calculations.

Values of the thermal conductivity are extracted at 1.9 K and for a magnetic field of 11 T, as in working conditions. Then,  $k_{strand}$  is evaluated using a proper mixture of Nb<sub>3</sub>Sn and copper. Since the thermal conductivity of the former is three orders of magnitude bigger than the latter, it can be just written

$$k_{strand} = k_{Cu} \frac{A_{Cu}}{A_{strand}} = 8.29 * 10^1 * \frac{1}{1.87} = 4.43 * 10^1 \frac{W}{m K} , \quad (A.I.20)$$

which is the thermal conductivity of the material multiplied by the relative fraction of copper inside a strand.

#### A.I.4.1.1. Copper fraction in a strand

The ratio Cu/non-Cu in a strand is 1.15. Then

$$A_{Cu} + A_{sc} = A_{strand} , \quad (A.I.21)$$

$$\frac{A_{Cu}}{A_{sc}} = 1.15 , \quad (A.I.22)$$

$$A_{Cu} + \frac{A_{Cu}}{1.15} = A_{strand} , \quad (A.I.23)$$

$$A_{Cu} \left( 1 + \frac{1}{1.15} \right) = 1.87 A_{Cu} = A_{strand} , \quad (A.I.24)$$

$$A_{Cu} = \frac{A_{strand}}{1.87} . \quad (A.I.25)$$

The contact thermal resistances between Copper/SS and Copper/Epoxy have also to be considered. These resistances are originated by a non-ideal contact between surfaces, which takes place only in three or four points, forcing the heat to flow only through very small portions of material. The acoustic mismatch in the phonon vibrations, between the crystalline structures of the two materials, gives its additional contribution in limiting the heat transfer between the layers.

Since it could be very difficult to compute these values by hand, experimental values in [29,34] have been used, where contacts between copper and stainless steel are reported, both at different pressures and in a temperature range between less than 20 and 300 K. From Fig.5 in [33], it is possible to extrapolate that

$$R'_{c,Cu-SS} \cong 2.2 * 10^{-3} m^2 \frac{K}{W} \quad (\text{at } 2 \text{ K}). \quad (A.I.26)$$

Fig. 11 in [28] is then used to derive the contact resistance between copper and the insulation

$$2R'_{c,Cu-ins} = 7 * 10^{-3} \frac{m^2 K}{W} \quad (A.I.27)$$

namely a function of temperature, with the value extracted around 4 K. Overall, the thermal resistance on the  $y'$ -axis gives

$$R'_{tot,y'} = 2 \frac{s_{gl-ep}}{k_{gl-ep}} + 2 \frac{s_{mica}}{k_{mica}} + 2 \frac{s_{strand,y}}{k_{strand}} + \frac{s_{core}}{k_{core}} + 2R'_{c,Cu-ins} + 2R'_{c,Cu-SS} = 3.3 * 10^{-2} \frac{m^2 K}{W} , \quad (A.I.28)$$

The main contributions to the total thermal resistance are given by the two layers of insulation and by the contact between the strands and the stainless-steel core. The definition of thermal resistance can be now inverted to derive the equivalent thermal conductivity on the  $y'$ -axis:

$$k_{tot,y'} = \tilde{k}_{y'} = \frac{s_{tot,y'}}{R_{tot,y'}} = \frac{(1.307 + 2 * 0.1) * 10^{-3}}{0.033} = 0.046 \frac{W}{m K} \quad (A.I.29)$$

#### A.I.4.2. Thermal conductivity along the $x'$ axis

A similar approach will be followed for the computation of the equivalent thermal conductivity along the  $x'$ -axis. Thermal resistances are still used but, due to the much larger dimension along the  $x'$ -axis, the calculations are based on a unit cell, shown in Fig.A.I.6. Such entity repeats identically in space, so that it will enable us to compute the total resistance on the cable width.

It is possible to identify 5 layers of materials, pointed out in the picture:

- 1) Glass-epoxy, with a thermal conductivity along the warp direction being 40% higher than along the normal direction, due to the anisotropy of the material.
- 2) Mica, with the same consideration on the thermal conductivity just made for glass-epoxy.
- 3) Two half strands, with a contact between them made of an interposed layer of epoxy resin.
- 4) Direct contact between strands, for  $\frac{1}{2}$  of the transversal dimension,  $s_{strand,y}$ .
- 5) The same as the 3<sup>rd</sup> layer, the reason why it will be multiplied by two, and in the figure is indicated again with no.3.

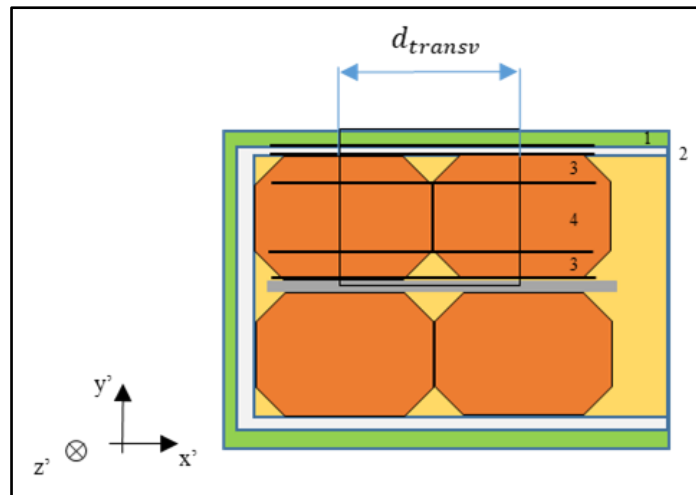


Figure A.I.6: Basic unit cell

In particular, for what concerns layer no. 3, the octagonal shape needs to be “averaged” in the sloped region (Fig.A.I.7), in order to define a thickness of the interposed layer of epoxy resin.

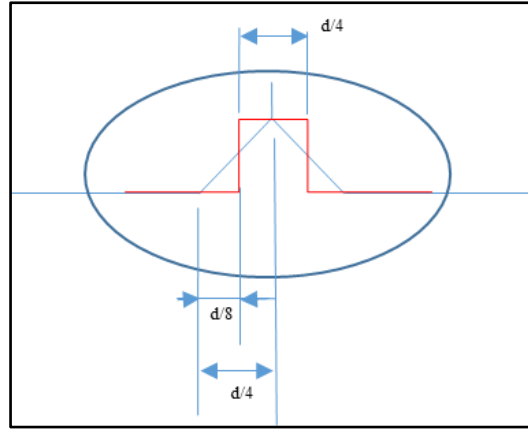


Figure A.I.7: Contact region between the strand and the epoxy resin. The average is made so that the areas of the triangle and the rectangle are the same.

Which is useful to compute both the thermal and the contact resistances. It corresponds to employ a rectangular shape rather than triangular in the contact region.

The thermal resistance in the 4 branches is then shown in Fig.A.I.8.

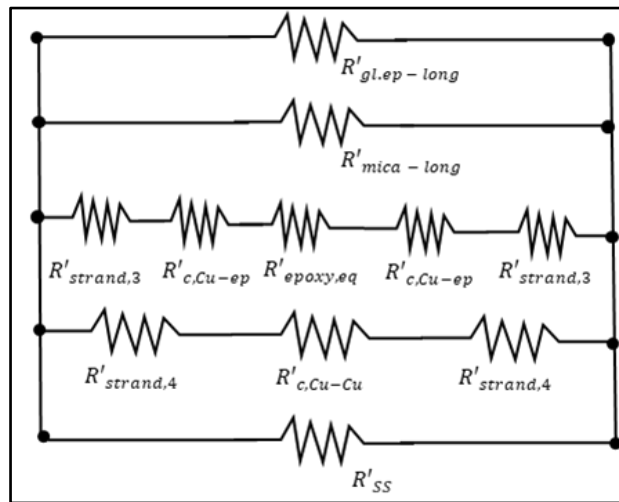


Figure A.I.8 Thermal model of the basic unit cell

Starting from the first branch

$$R'_1 = R'_{gl-ep,long} = \frac{d_{transv}}{k_{gl,ep,long}} = \frac{0.714 * 10^{-3}}{1.4 * 2.04 * 10^{-2}} = 0.025 \frac{m^2 K}{W} . \quad (A.I.30)$$

The unit cell takes half of the left strand and half of the right one, the reason why it has been considered of length equal to  $d_{transv}$ . The thermal conductivity is considered in the longitudinal direction, since in this case heat would propagate along it, which is something that, in general, is a 40% higher than in the normal direction.

In the case of mica, which makes the second branch, the way of thinking is the same

$$R'_2 = R'_{mica,long} = \frac{d_{transv}}{k_{mica,long}} = \frac{0.714 * 10^{-3}}{1.4 * 6 * 10^{-3}} = 0.085 \frac{m^2K}{W}. \quad (A.I.31)$$

Third and fourth branches give

$$R'_{strand,3} = \frac{\frac{d_t}{2} - \frac{d_t}{8}}{k_s} = \frac{\frac{3}{8} * 0.714 * 10^{-3}}{4.43 * 10^1} = 6.04 * 10^{-6} \frac{m^2K}{W}, \quad (A.I.32)$$

$$2R'_{c,Cu-ep} = 7.0 * 10^{-3} \frac{m^2K}{W}, \quad (A.I.33)$$

$$R'_{epoxy} = \frac{d_t/4}{k_{epoxy}} = \frac{\frac{1}{4} * 0.714 * 10^{-3}}{3.32 * 10^{-2}} = 5.38 * 10^{-3} \frac{m^2K}{W}. \quad (A.I.34)$$

$d_t/4$  is taken because, looking back at Fig.A.I.7, the total thickness of the epoxy resin is given by two equivalent rectangular regions, both of which are  $d_t/8$  in length. So

$$R'_3 = R'_{s,w/o,ep} = 2R'_{strand,3} + 2R'_{c,Cu-ep} + R'_{epoxy} = 1.24 * 10^{-2} \frac{m^2K}{W}, \quad (A.I.35)$$

where  $R'_{strand,3}$  and  $R'_{strand,4}$  refer to the strand thermal resistance in the third and fourth layer, respectively.  $R'_{s,w/o,ep}$  stands for contact between strands without interposed epoxy, while  $R'_{s,w,ep}$  will now be used for contact with epoxy.

$$R'_{strand,4} = \frac{d_t}{k_s} = \frac{\frac{1}{2} * 0.714 * 10^{-3}}{4.43 * 10^1} = 8.06 * 10^{-6} \frac{m^2K}{W}, \quad (A.I.36)$$

$$R'_{c,Cu-Cu} = 2.5 * 10^{-2} \frac{m^2K}{W}, \quad (A.I.37)$$

$$R'_4 = R'_{s,w,ep} = 2R'_{strand,4} + R'_{c,Cu-Cu} = 2.5 * 10^{-2} \frac{m^2K}{W}. \quad (A.I.38)$$

The parallel between the lower and upper branches is computed, balancing them with their relative weight on a line normal to the  $y'$ -axis. As previously remarked for the example of electrical resistances (eq.A.I.11), the area normal to the direction in respect to which the resistance is computed, is considered. The present case is quite similar to that, where rather than taking the area, only the linear relative proportions are taken into account

$$R'_{cell} = \left( \sum_i \frac{w_i}{R'_i} \right)^{-1}, \quad (A.I.39)$$

where the factors  $w_i$  are adimensional

$$w_i = \frac{s_i}{\sum_{j=1}^N s_j}. \quad (A.I.40)$$

For example

$$w_{mica} = \frac{s_{mica}}{s_{mica} + s_{ge} + s_{strand,y}} = \frac{0.05}{0.741} = 0.067 , \quad (\text{A.I.41})$$

Then,

$$R'_{cell} = \left( \frac{w_{ge}}{R'_{ge}} + \frac{w_{mica}}{R'_{mica}} + \frac{w_{s,w/o,c}}{R'_{s,w/o,c}} + \frac{w_{s,c}}{R'_{s,w,c}} \right)^{-1} = 1.35 * 10^{-2} \frac{m^2 K}{W} . \quad (\text{A.I.42})$$

There are 21 unit-cells along the  $x'$ -axis like the one already presented, connected in series. Then, on the left and on the right boundaries there are other two half-unit cells (Fig.A.I.9), which are quite different from the one described above. In total, and as already mentioned, there are 22 strands on a single line, and that is because the system is tilted relatively to the cable main direction.

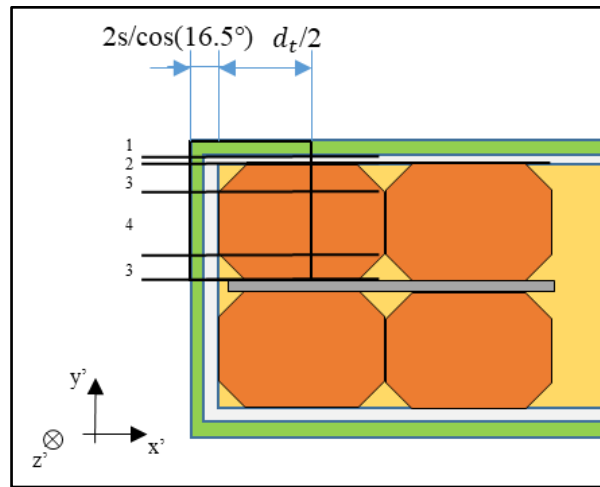


Figure A.I.9: Border unit cell

It is worthwhile to remind that there are 20 pairs of strands in the cross-section  $l$  (cfr. Fig.A.I.5), while in the tilted section, namely  $l'$ , the pairs become 22.

The thermal model of the border unit-cell is the same as before, with the exception that the two lower branches are different, as Fig.A.I.10 shows.

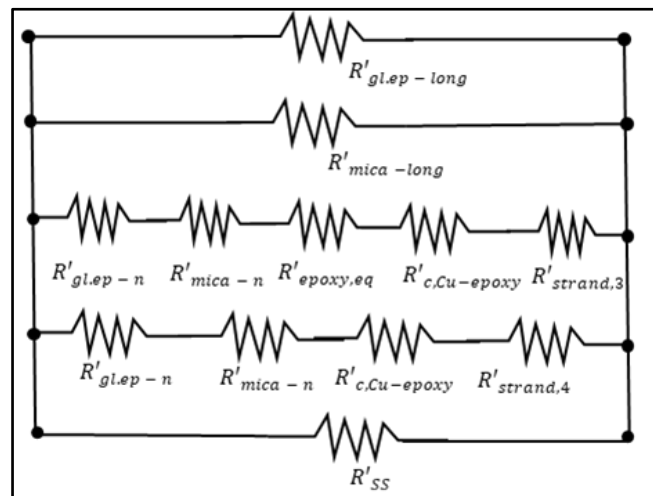


Figure A.I.10. Thermal model for the border unit cell.

Both in the third and fourth layer, the first two resistances are substituted by  $R'_{gl.ep-n}$  and  $R'_{mica-n}$ , where the “n” stands the normal direction of the fibers. Calculations are

$$\begin{aligned} R'_1 = R'_{gl.ep-long} &= \frac{\frac{d_t}{2} + 2 * \frac{S_{gl.ep}}{\cos(16.5^\circ)}}{k_{gl.ep-long}} = \frac{\left(\frac{0.714}{2} + 2 * \frac{0.05}{\cos(16.5^\circ)}\right) * 10^{-3}}{1.4 * 2.04 * 10^{-2}} \\ &= 1.62 * 10^{-2} \frac{m^2K}{W}, \end{aligned} \quad (A.I.43)$$

$$\begin{aligned} R'_2 = R'_{mica-long} &= \frac{\frac{d}{2} + 2 * \frac{S_{mica}}{\cos(16.5^\circ)}}{k_{mica-long}} = \frac{\left(\frac{0.714}{2} + 2 * \frac{0.05}{\cos(16.5^\circ)}\right) * 10^{-3}}{1.4 * 6 * 10^{-3}} \\ &= 5.49 * 10^{-2} \frac{m^2K}{W}. \end{aligned} \quad (A.I.44)$$

Then

$$R'_{gl.ep-n} = \frac{\frac{S_{gl.ep}}{\cos(16.5^\circ)}}{k_{gl.ep-n}} = \frac{0.05}{\cos(16.5^\circ)} * 10^{-3}}{2.04 * 10^{-2}} = 2.56 * 10^{-3} \frac{m^2K}{W}, \quad (A.I.45)$$

$$R'_{mica-n} = \frac{\frac{S_{mica}}{\cos(16.5^\circ)}}{k_{mica-n}} = \frac{0.05}{\cos(16.5^\circ)} * 10^{-3}}{6 * 10^{-3}} = 8.69 * 10^{-3} \frac{m^2K}{W}, \quad (A.I.46)$$

$$R'_{epoxy,eq} = \frac{S_{ep,eq}}{k_{epoxy}} = \frac{d_t/8}{k_{epoxy}} = \frac{\frac{1}{8} * 0.714 * 10^{-3}}{3.32 * 10^{-2}} = 2.69 * 10^{-3} \frac{m^2K}{W}, \quad (A.I.47)$$

$$R'_{c,Cu-ep} = \frac{7 * 10^{-3}}{2} = 3.25 * 10^{-3} \frac{m^2K}{W} \quad (A.I.48)$$

$R'_{strand,3}$ ,  $R'_{strand,4}$  are the same as before. So

$$R'_3 = R'_{gl.ep-n} + R'_{mica-n} + R'_{epoxy,eq} + R'_{c,Cu-ep} + R'_{strand,3} = 1.72 * 10^{-2} \frac{m^2K}{W}, \quad (A.I.49)$$

$$R'_4 = R'_{gl.ep-n} + R'_{mica,n} + R'_{c,Cu-ep} + R'_{strand,4} = 1.45 * 10^{-2} \frac{m^2K}{W}, \quad (A.I.50)$$

$$R'_{border} = \left( \sum_i \frac{w_i}{R'_i} \right)^{-1} = \left( \frac{0.067}{1.62 * 10^{-2}} + \frac{0.067}{5.49 * 10^{-2}} + \frac{0.433}{1.72 * 10^{-2}} + \frac{0.433}{1.45 * 10^{-2}} \right)^{-1} \quad (\text{A.I.51})$$

$$= 1.66 * 10^{-2} \frac{m^2 K}{W} ,$$

which is similar to the value of a basic unit cell.

The border unit cell is slightly more than half of the dimension of a basic unit cell. This means that the main contribution comes from the insulation. The resistance of the upper half of the cable cross-section is

$$R'_{half,x} = 21 * R'_{cell} + 2 * R'_{border} = 3.17 * 10^{-1} \frac{m^2 K}{W} . \quad (\text{A.I.52})$$

It should be noted that, until now, only half of the cable cross-section has been considered, correspondent to the upper line of strands. The lower line is exactly equal to the upper. Then, a further core layer made of stainless-steel is also present. It is very thin, and mica and glass-fiber are present at its ends, as Fig.A.I.11 shows.

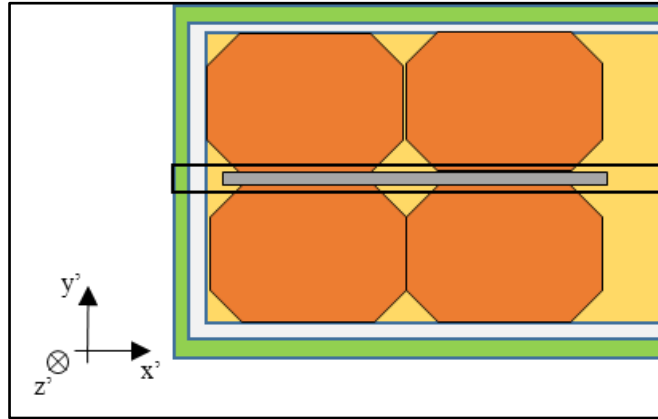


Fig.A.I.11: Core unit cell

The thermal resistance of this core unit cell is

$$R'_{core\ cell} = \frac{t}{k_{SS} \cos(16.5^\circ)} + \frac{2 * \frac{S_{gl.ep}}{\cos(16.5^\circ)}}{k_{gl.ep-n}} + \frac{2 * \frac{S_{mica}}{\cos(16.5^\circ)}}{k_{mica-n}} = 1.83 * 10^{-1} \frac{m^2 K}{W} . \quad (\text{A.I.53})$$

Finally, the upper and lower halves, together with the middle core layer, are put together in parallel, balancing them with their relative length proportion on the y'-axis, as it was also done before for a single half in eq.(A.I.41)

$$R'_{tot,x'} = \left( \sum_i \frac{w_i}{R'_i} \right)^{-1} = \left( \frac{w_{upper}}{R'_{upper}} + \frac{w_{core}}{R'_{core}} + \frac{w_{lower}}{R'_{lower}} \right)^{-1} = \left( \frac{0.490}{0.317} + \frac{0.490}{0.317} + \frac{0.02}{0.183} \right)^{-1} \quad (\text{A.I.54})$$

$$= 0.312 \frac{m^2 K}{W} .$$

The equivalent thermal conductivity along  $x'$  is

$$k_{tot,x'} = \hat{k}_{x'} = \frac{\frac{w + 2s_{ins}}{\cos(\alpha)}}{R_{tot,x'}} = \frac{(14.85 + 2 * 0.1) * 10^{-3}}{\cos(16.5^\circ)} = 0.050 \frac{W}{m K} . \quad (A.I.55)$$

All the thicknesses of the insulation layers are divided by the cosine of the twisting angle. In fact, these quantities are given in a cross-section normal to the cable main direction, namely the  $l$  line, while in the calculations the reference system is attached to a strand,  $l'$ .

This is the reason why the thicknesses are increased by the same amount,  $\cos(16.5^\circ) \cong 1.043$ . On the other hand, no correction is applied on the strand dimension, since its proper dimension is already been considered on  $l'$ .

#### A.I.4.3. Thermal conductivity along the $z'$ axis

Let's move forward. The thermal resistance along the  $z'$ - direction can be derived through a simple computation that, in the first place, considers strands as straight lines. This is done by averaging the properties of the materials on the unit-cell

$$k_{tot,z'} = \tilde{k}_{z'} = \sum_i k_i \frac{A_i}{A_{tot}} , \quad (A.I.56)$$

There are four kinds of materials in a unit cell: Nb<sub>3</sub>Sn, copper, impregnation and insulation. Since the thermal conductivity of copper is much larger than the other materials, the overall thermal conductivity could just be written as  $k_{Cu}$  times its area fraction in the cable

$$\tilde{k}_{z'} = \frac{A_{Cu}}{A_{tot}} * k_{Cu} = 0.398 * 8.290 * 10^1 = 3.299 * 10^1 \frac{W}{m K} , \quad (A.I.57)$$

where the thermal conductivity of copper is at a field of 11 T and at 1.9 K.

#### A.I.4.4. Tensor rotation and effective thermal conductivity

In the local coordinate system of a strand, the thermal conductivity tensor is a diagonal matrix 3x3

$$\tilde{k}_{local} = \begin{bmatrix} \tilde{k}_{x'} & 0 & 0 \\ 0 & \tilde{k}_{y'} & 0 \\ 0 & 0 & \tilde{k}_{z'} \end{bmatrix} . \quad (A.I.58)$$

The values inside the matrix have already been derived. Having a diagonal matrix implies that, considering the Fourier's law of heat transfer

$$\vec{q} = -\tilde{k} \vec{\nabla} T , \quad (A.I.59)$$

if a temperature gradient is applied along a certain direction, let's say  $y$ , heat will flow in the same direction of the gradient, but in the opposite sense. This is no longer true when the matrix has non-zero elements outside the diagonal, as it is the case for a Rutherford cable, a system where strands are tilted of an  $\alpha$  angle. To give an example, applying a thermal gradient along  $z$  would mean a heat flow both along  $z$  and  $x$ . The matrix, even if still symmetric, will not be diagonal anymore, and the terms in the diagonal itself will change.

In order to pass from the local to global system, namely from section  $l'$  to  $l$ , a tensor rotation must be applied. This could be done using the method described in [29] and [30], as

$$\tilde{k}_{global} = T^{-1} \tilde{k}_{local} T , \quad (\text{A.I.60})$$

where  $T$  is the rotation matrix, formed by of the direction cosines

$$T = \begin{bmatrix} \cos \alpha & 0 & \sin \alpha \\ 0 & 1 & 0 \\ -\sin \alpha & 0 & \cos \alpha \end{bmatrix} , \quad (\text{A.I.61})$$

and

$$T^{-1} = \begin{bmatrix} \cos \alpha & 0 & -\sin \alpha \\ 0 & 1 & 0 \\ \sin \alpha & 0 & \cos \alpha \end{bmatrix} . \quad (\text{A.I.62})$$

The matrix product gives

$$\tilde{k}_{global} = \begin{bmatrix} \tilde{k}_x \cos^2 \alpha + \tilde{k}_z \sin^2 \alpha & 0 & \tilde{k}_z \sin \alpha \cos \alpha + \tilde{k}_x \sin \alpha \cos \alpha \\ 0 & \tilde{k}_y & 0 \\ \tilde{k}_z \sin \alpha \cos \alpha + \tilde{k}_x \sin \alpha \cos \alpha & 0 & \tilde{k}_z \cos^2 \alpha + \tilde{k}_x \sin^2 \alpha \end{bmatrix} , \quad (\text{A.I.63})$$

which can be written as

$$\tilde{k}_{global} = \begin{bmatrix} \bar{k}_x & 0 & \bar{k}_{xz} \\ 0 & \bar{k}_y & 0 \\ \bar{k}_{zx} & 0 & \bar{k}_z \end{bmatrix} . \quad (\text{A.I.64})$$

It is interesting to compare the elements inside the two matrices, in order to see how much their values change. The  $\alpha$  angle, formed by a strand with the cable  $z$ -direction is approximately  $16.5^\circ$ . Consequently

$$\bar{k}_x = \tilde{k}_{x'} \cos^2 \alpha + \tilde{k}_{z'} \sin^2 \alpha = 2.71 \frac{W}{m K} , \quad (\text{A.I.65})$$

$$\bar{k}_y = \tilde{k}_{y'} = 0.046 \frac{W}{m K} , \quad (\text{A.I.66})$$

$$\bar{k}_z = \tilde{k}_{z'} \cos^2 \alpha + \tilde{k}_{x'} \sin^2 \alpha = 30.33 \frac{W}{m K} , \quad (\text{A.I.67})$$

$$\bar{k}_{xz} = \bar{k}_{zx} = \tilde{k}_z \sin \alpha \cos \alpha + \tilde{k}_x \sin \alpha \cos \alpha = 9.00 \frac{W}{m K} . \quad (\text{A.I.68})$$

A certain degree of variability can be observed in the values inside the  $\tilde{k}_{local}$  matrix, up to three orders of magnitude between  $\tilde{k}_{y'}$  and  $\tilde{k}_{z'}$ . On the  $y'$ -direction two layers of insulator plus a high thermal resistance between strands and the SS core are present. Along the  $x'$ -direction two layers of insulation add themselves to thin layers of epoxy between strands. On the other hand, along the  $z'$ -direction there are no thermal barriers, with copper that enables heat conduction. For these reasons, the  $\tilde{k}_{x'}$  value is very similar to  $\tilde{k}_{y'}$ , but they are both two orders of magnitude below  $\tilde{k}_{z'}$ .

Due to the intervention of twisting, which imply the use of sine and cosine functions, and under the influence of thermal conductivity along the cable main direction, the  $k_{xx}$  value in the global matrix increases almost by two orders of magnitude, passing from 0.050 to 2.71 W/m K.

A remarkable change in the form of the conductivity matrix is that it becomes non-diagonal, which means that a thermal gradient applied along a certain direction, causes heat to flow also on other directions. The value of conductivity in the “mixed” direction,  $xz$ , is rather high, being a third of the effective conductivity on the  $z$ -axis. The value in position (1,3),  $k_{xz}$  is the same as in (3,1),  $k_{zx}$ , so that the matrix is symmetric, as one would have expected, and as it is deeply discussed in [33, 34].

#### A.I.4.5. Thermal conductivity on a multiple twist-pitch scale

This last result is quite important, but it is valid only when the attention is focused on a small portion of the cable, let’s say half of a twist pitch. When one considers a multiple twist pitch scale, heat propagates, nevertheless, only along the  $z$ -direction. The matrix would then become symmetric again, which is something that it is worthwhile to prove. Let’s consider the point where a generic strand turns, from Fig.A.I.12.

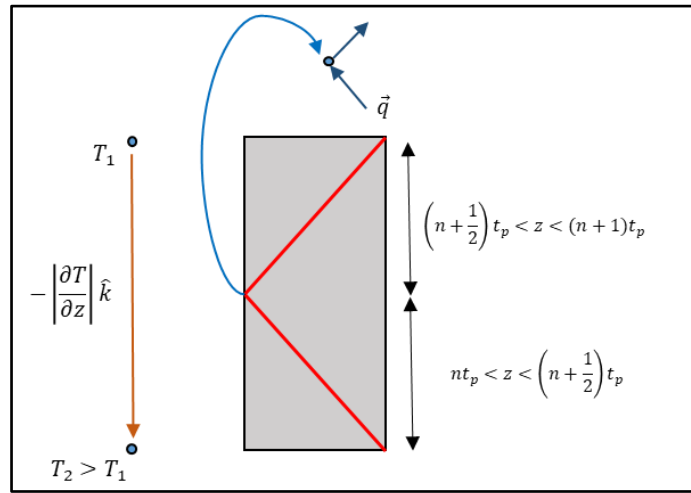


Figure A.I.12: Representation of a single strand, and of the heat vector in the turning point.

In that point heat follows the strand, which behaves as a sort of “tube” for heat propagation. In general, for

$$nt_p < z < \left(n + \frac{1}{2}\right)t_p ,$$

where  $t_p$  is the twist-pitch length and  $n$  is integer, the matrix is

$$\tilde{k}_{global} = \begin{bmatrix} \bar{k}_x & 0 & -\bar{k}_{xz} \\ 0 & \bar{k}_y & 0 \\ -\bar{k}_{zx} & 0 & \bar{k}_z \end{bmatrix} . \quad (A.I.69)$$

While for

$$\left(n + \frac{1}{2}\right)t_p < z < (n + 1)t_p ,$$

The elements outside the diagonal change sign

$$\tilde{k}_{global} = \begin{bmatrix} \bar{k}_x & 0 & \bar{k}_{xz} \\ 0 & \bar{k}_y & 0 \\ \bar{k}_{zx} & 0 & \bar{k}_z \end{bmatrix}. \quad (\text{A.I.70})$$

If a thermal gradient, which can be written as

$$\vec{\nabla}T = - \left| \frac{\partial T}{\partial z} \right| \hat{k}, \quad (\text{A.I.71})$$

is applied at the extremities of the twist pitch, each half of a strand is subjected to half of the thermal gradient, which means to half of the overall temperature drop, due to the equality in the two parts. The resulting heat vectors are

$$\begin{cases} \vec{q}_{0-\frac{1}{2}} = -\bar{k}_{xz} * \frac{1}{2} \left| \frac{\partial T}{\partial z} \right| \hat{i} + \bar{k}_z * \frac{1}{2} \left| \frac{\partial T}{\partial z} \right| \hat{k}, \\ \vec{q}_{\frac{1}{2}-1} = \bar{k}_{xz} * \frac{1}{2} \left| \frac{\partial T}{\partial z} \right| \hat{i} + \bar{k}_z * \frac{1}{2} \left| \frac{\partial T}{\partial z} \right| \hat{k}, \end{cases} \quad (\text{A.I.72})$$

where the subscripts  $0-1/2$  and  $1/2-1$  refer to the lower and upper halves of the twist pitch, respectively. Heat flows in the negative  $x$ -direction and positive  $z$ -direction in the lower half, while it changes sign along the  $x$ -direction in the upper half.

Summing the vectors

$$\vec{q}_{0-\frac{1}{2}} + \vec{q}_{\frac{1}{2}-1} = \bar{k}_z \left| \frac{\partial T}{\partial z} \right| \hat{k}. \quad (\text{A.I.73})$$

Then, the value of heat flow in the two halves of the cable cross-section is the same

$$\left| \vec{q}_{0-\frac{1}{2}} \right| = \left| \vec{q}_{\frac{1}{2}-1} \right| = |\vec{q}|, \quad (\text{A.I.74})$$

$$2|\vec{q}| = \bar{k}_z \left| \frac{\partial T}{\partial z} \right|, \quad (\text{A.I.75})$$

$$|\vec{q}| = \frac{1}{2} \bar{k}_z \left| \frac{\partial T}{\partial z} \right|, \quad (\text{A.I.76})$$

which is the module of the heat transported on one or a multiple twist-pitch scale which allows to say that the vector is directed only along  $\hat{k}$ . So

$$\vec{q} = \frac{1}{2} \bar{k}_z \left| \frac{\partial T}{\partial z} \right| \hat{k}. \quad (\text{A.I.77})$$

It seems from the last expression that the effective thermal conductivity is divided by two, but it has to be reminded that only half of the cross-section has been considered, which is the upper line of strands in the rectangular cross section. Similar considerations can be made for the other layer, which twists towards the right, bringing to a similar result. The heat actually conducted is then doubled and the final thermal conductivity along  $z$  returns to be equal to  $\bar{k}_z$ .

In the end, the matrix of the thermal conductivity becomes

$$\tilde{k}_{mult,tp} = \begin{bmatrix} \bar{k}_x & 0 & 0 \\ 0 & \bar{k}_y & 0 \\ 0 & 0 & \bar{k}_z \end{bmatrix}, \quad (\text{A.I.78})$$

which means that it is diagonal again, and that heat propagates as in a conventional material. A thermal gradient applied in a certain direction causes heat to flow only along that same direction. Nevertheless, the material is anisotropic, so conduction is facilitated along the  $z$ -direction, where the presence of copper plays a very important role. Due the effect of the twist pitch, it makes feel its presence also on the  $x$ , improving heat transport along this direction almost by an order of magnitude. No change is, instead, observable on the  $y$ -direction, since twisting is only with respect to the  $x$ .

#### A.I.4.6. Comparison with experimental measurements.

The aim of chapter 3 was to describe the heat exchange properties of helium with Nb-Ti superconducting coils as a function of temperature. Nb<sub>3</sub>Sn coils are much different from their predecessors, due to the impregnation with epoxy-resin which does not enable helium to filter in the very small interstices of the cables and to act on very short time scales to remove heat. This makes it relevant to assess coil behavior under heat depositions and thermal conductivity data are an essential component for this.

It is very interesting to see how the computations made in the present Appendix can be compared with experimental data, conducted on coils of the 11 T [34]. To be more specific, coil no. 104, which was discarded due to oversizing was used to perform the tests. The coil was produced using the standard manufacturing process and insulation layout of the 11 T dipole. Thermal conductivity measurements were made in two directions, as Fig.A.I.13 depicts.

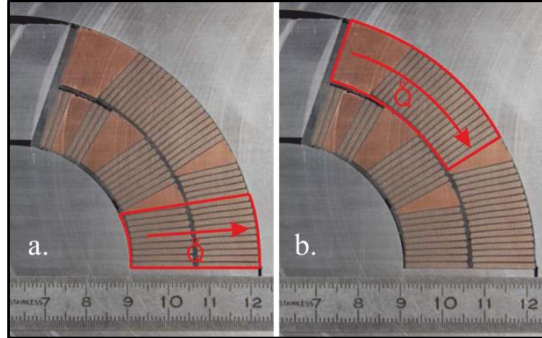


Fig.A.I.13: Samples derived from coil #104 were used to measure thermal conductivity in the radial (a) and azimuthal directions (b).

One was along the radial direction (a), the other on the azimuthal direction (b). The respective set-up configurations are shown in Fig.A.I.14 (a) and (b). Samples were inserted between copper blocks that enabled to inject a known heat flux in the system,  $\dot{Q}$ , and measure a temperature drop,  $\Delta T$ , across it. Then, expression (A.I.2), that we remind here

$$k = \frac{\dot{Q} L}{A \Delta T},$$

can be used to derive the value of the thermal conductivity at a given temperature (as the average of the temperatures that produce the  $\Delta T$ ).

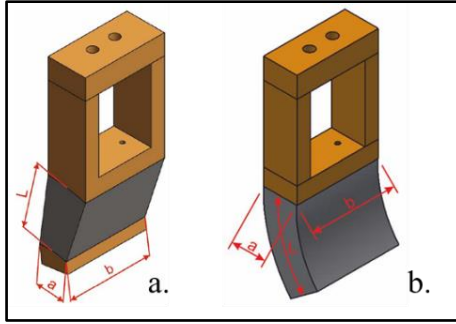


Fig.A.I.14: Samples derived from coil #104 were used to measure thermal conductivity in the radial (a) and azimuthal directions (b).

Measurements were conducted in the temperature range between 3 and 300 K and are reported here in Fig.A.I.15.

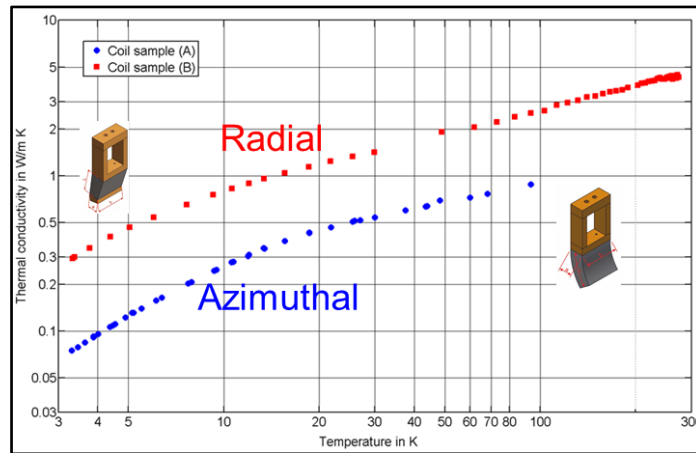


Fig. A.I.15: CERN measurements of radial and azimuthal thermal conductivity of 11 T coils. Credits: reference [34].

The radial axis is equivalent to the  $x$ , while the azimuthal to the  $y$  of our calculations. The final value of conductivity for the  $x$ , namely  $\bar{k}_x$  was equal to 2.71 W/m/K, and 0.046 for  $\bar{k}_y$ . Before making further considerations, some changes should be made in the values above, adapting them to the experimental geometry. The sample derived for the azimuthal direction was made of 18 cables plus the copper wedge. Each cable has the thermal resistance computed in eq.(A.I.26), which is 0.033 W/m/K, while the copper wedge can be assumed to not contribute to the overall resistance of the stack due to high thermal conductivity of copper. Nevertheless, its thickness (which is equivalent approximately to 5 cables) adds to that of the other 18 cables, thus reducing the thermal conductivity of the stack. The result is

$$k_{azim} = \frac{S_{azim}}{R'_{azim}} = \frac{18 * (1.307 + 2 * 0.1) * 10^{-3}}{(18 + 5) * 0.033} = 0.035 \frac{W}{m K} , \quad (A.I.79)$$

The value extracted from the experiment in the case of the longitudinal direction is 0.05 W/m/K at the lowest temperature, which is 3.3 K. Extrapolating the curve for the temperature of interest, 1.9 K, a value of 0.02 W/m/K is obtained. This is in the same order of magnitude of the value already computed in eq.(A.I.77), even if with a certain degree of uncertainty.

Let's now consider the radial direction. Again, changes must be made about the actual configuration of the sample, which comprehends two cable layers plus the interlayer insulation. The total resistance along the  $x$ -axis is given by

$$R'_{radial} = R'_{tot,x} + R'_{interlayer} + R'_{tot,x} , \quad (\text{A.I.80})$$

where

$$R'_{tot,x} = \frac{S_{cable,x}}{\bar{k}_x} = \frac{15.05 * 10^{-3}}{2.71} = 5.55 * 10^{-3} , \quad (\text{A.I.81})$$

and

$$R'_{interlayer} = \frac{S_{interlayer}}{k(G10)_{1.9K}} = \frac{5 * 10^{-4}}{2.04 * 10^{-2}} = 0.025 \frac{m^2K}{W} . \quad (\text{A.I.82})$$

The resistance along the radial coordinate is then

$$R'_{radial} = 2 * 0.0055 + 0.025 = 0.036 \frac{m^2K}{W} , \quad (\text{A.I.83})$$

and the effective thermal conductivity

$$k_{radial} = \frac{S_{tot,radial}}{R'_{radial}} = \frac{(15.05 + 0.5 + 15.05) * 10^{-3}}{0.036} = 0.85 \frac{W}{mK} , \quad (\text{A.I.84})$$

Having a look at the curve in Fig.A.I.15, the value of thermal conductivity at 3.3 K is 0.3 W/m/K, and its behavior suggests that it goes down to 0.2 W/m/K at 2 K, thus being quite far from the value already derived. The purpose of the following lines is to address the source of this discrepancy, giving two possible explanations.

A Rutherford cable is made of a certain number of strands, which are twisted together in order to have a rectangular shape. The twist-pitch length in a cable for the 11 T Dipole is 11.2 centimeters, which means that, looking at one single strand, it returns to the same value of the  $x$ -coordinate exactly after a complete period, which corresponds to a displacement along the  $z$  of 11.2 cm.

Now comes a very important point. Heat can propagate along the strands, which act as tubes for the flow of heat, only if they are able to complete an entire twist-pitch. If this does not happen, strands meet the insulation and heat is not able to find the way at lower heat resistance, which is the strand itself. Thus, it is forced to pass through the path at lower conductance, defined by the adjacent contact between strands, degrading the properties of heat exchange.

Taking exactly half twist-pitch, only one strand makes a turn, and for the efficient mechanism of heat conductance to take place, all strands should complete the turn, which would require another half twist-pitch, giving one twist-pitch in total. The value of the effective thermal conductivity then starts from 0.05 W/m/K, given in eq.(A.I.53), for a sample length of half twist-pitch, progressively increasing as more strands complete the turn. reaching  $\bar{k}_x = 2.71$  W/m/K in eq.(A.I.63).

For the reasons explained, the value for  $k_{radial}$  derived in eq.(A.I.82) was overestimated. In the case under examination, the sample is 100 mm in length, less than a twist pitch, so that not every strand has the linear space to complete the turn, and in turn decreases the value of the thermal conductivity.

A second explanation is provided by the dimensions of the interlayer insulation which, from measures directly performed on a coil sample, are bigger than the 0.5 mm of the design project. If a thickness of 1 mm is taken and the computations repeated, thermal conductivity drops to 0.51 W/m/K, much closer to the experimental value. Together with the first reasoning, they help to explain the discrepancy between computations and experiments. However, further studies should shed more light on this subject even reconsidering material properties, due to the relevance of properly knowing thermal behavior of impregnated superconducting coils

## Appendix II.

### Volume of metallic parts of the Cryolab sample

In the Cryolab experiment a sample of the 11 T dipole coil is tested. The sample is derived from a quarter of a magnet, and it comprehends 9 cables in the inner layer plus the copper wedge, and 16 cables in the outer layer. The aim is to compute the total volume of the sample, and the fraction of metal (copper and superconductor) inside it, without taking the copper wedge into account.

The cable dimensions are the standard for the 11 T dipole. The sample length will be considered to be 140 mm, while the length of the face exposed to helium is only 125 mm (due to the two extremities of the G10 box).

Let's start from the inner layer: the dimensions of the cable cross-section are: 14.85 mm x 1.307 mm. The thickness of the conductor insulation, which is equal to 0.1 mm, must be added from both sides. Then, the total volume for the inner layer is

$$V_{inner} = (0.1 + 14.85 + 0.1) * (0.1 + 1.307 + 0.1) * 140 * 9 = 28.58 \text{ cm}^3 . \quad (\text{A.II.1})$$

The thickness of the interlayer insulation is added to the outer layer, so that it is easier to take them into account. The volume of the outer layer plus the interlayer is then

$$V_{outer} = (0.1 + 14.85 + 0.1 + 0.5) * (0.1 + 1.307 + 0.1) * 140 * 16 = 52.49 \text{ cm}^3 . \quad (\text{A.II.2})$$

The sum of (1) and (2) gives the sample volume

$$V_{sample} = 81.07 \text{ cm}^3 , \quad (\text{A.II.3})$$

which does not take the copper wedge into account. Now we want to compute just the volume of metallic parts. The area of a bare cable is

$$A_{bare} = 14.85 * 1.307 = 19.41 \text{ mm}^2 . \quad (\text{A.II.4})$$

Then, the area of the strands is

$$A_{strands} = 44 * \pi \left( \frac{0.714}{2} \right)^2 = 17.62 \text{ mm}^2 . \quad (\text{A.II.5})$$

In fact, there are 44 strands in the tilted section, more than the 40 on the cable normal direction. Reporting this last area on a section normal to the cable main direction we obtain

$$A_{projected} = A_{strands} * \cos(16.5^\circ) = 16.89 \text{ mm}^2 , \quad (\text{A.II.6})$$

so that the ratio of metallic material in a cable is:  $16.89/19.41 = 0.87$ , and the volume of metallic parts in the sample is

$$V_{metal} = (14.85 * 1.307 * 0.87) * 140 * 25 = 59.10 \text{ cm}^3 . \quad (\text{A.II.7})$$

This last number is used to average the total input power in *mW* (provided by the Cryolab team) in order to run the simulations.

### Appendix III.

*Detailed data about the experiments*

T [K]	P [mW]	Inner center	Inner off-center	Outer center	Outer off-center
He bath	Total input power	T rise (mK)	T rise (mK)	T rise (mK)	T rise (mK)
1.9	17	5.7	21.5	41.4	35.3
	17	5.5	21.3	41.0	35.0
	18	7.7	27.1	52.2	45.0
	22	13.6	41.1	79.1	69.4
	22	13.9	41.4	79.4	69.5
	28	21.8	56.7	109.2	96.0
	50	52.0	104.6	193.9	173.9
	50	51.9	104.6	194.2	174.0
	65	29.3	66.2	127.6	110.2
	75	40.3	82.6	157.5	137.0
	83	93.1	157.8	289.1	271.2
	98	68.9	121.3	220.2	198.0
	122	102.2	161.4	300.1	278.1
	128	150.0	227.2	447.9	454.0
	128	149.9	227.2	448.4	454.5
	169	208.1	338.4	613.4	613.7
	182	206.6	329.6	602.1	596.5
	189	237.4	392.1	688.5	693.0
	203	267.2	441.6	760.9	767.1
	203	260.6	435.0	751.8	758.6
	244	368.4	531.8	899.5	897.3
	308	672.4	766.6	1326.0	1316.6
	356	908.8	1005.2	1759.2	1755.2
	377	1021.7	1119.9	1969.9	1958.1
	392	1125.6	1224.6	2143.3	2141.1

*Table A.III.1: Temperature measurements for the 4 sensors and for all the heating regimes of the Cryolab experiment. This table is related to Fig.4.15.*

Total input power [mW]	Inner center	Inner off-center	Outer center	Outer off-center	Sim - Point 4 [s]	Sim - Point 14 [s]
17	1.5	1.3	1.4	1.4	3.41	2.39
18	1.2	1.4	1.4	1.5	3.38	2.38
22	1.6	1.5	1.5	1.6	3.30	2.35
28	1.9	1.5	1.6	1.7	3.19	2.31
50	1.8	1.5	1.6	1.8	2.89	2.16
65	1.7	1.5	1.5	1.6	2.73	2.07
75	1.8	1.5	1.5	1.7	2.64	2.02
83	2.0	1.6	1.7	2.0	2.58	1.98
98	1.9	1.5	1.5	1.8	2.48	1.91
122	1.9	1.6	1.8	2.2	2.34	1.82
128	2.0	1.8	2.1	2.8	2.31	1.80
169	2.1	2.5	1.9	2.4	2.15	1.67
182	1.9	2.4	1.9	2.4	2.10	1.64
189	2.0	2.4	1.8	2.3	2.08	1.62
203	2.0	2.2	1.7	2.1	2.04	1.59
244	2.2	1.9	1.5	1.8	1.94	1.50
308	1.7	1.5	1.3	1.6	1.83	1.40
356	1.4	1.3	1.2	1.4	1.76	1.33
377	1.3	1.2	1.2	1.3	1.73	1.31
392	1.2	1.2	1.1	1.3	1.72	1.29

Table A.III.2: Time constants of the four sensors and for the simulations in Point 4 and 14 the two columns on the right), which reproduce the sensors position.

Total input power	Input power density
[mW]	[mW/cm <sup>3</sup> ]
17	0.288
18	0.310
22	0.379
28	0.479
50	0.843
65	1.101
75	1.270
83	1.397
98	1.659
122	2.068
128	2.160
169	2.860
182	3.074
189	3.198
203	3.442
244	4.122
308	5.209
356	6.029
377	6.385
392	6.631

Table A.III.3: Total input power and power density, this last one obtained by division of the first column by the metallic fraction in the sample.

**Temperature Response Data Table (typical)**

	CX-1010			CX-1030			CX-1050		
	$R^B(\Omega)$	$dR/dT$ ( $\Omega/K$ )	$(T/R) \cdot$ ( $dR/dT$ )	$R(\Omega)$	$dR/dT$ ( $\Omega/K$ )	$(T/R) \cdot$ ( $dR/dT$ )	$R(\Omega)$	$dR/dT$ ( $\Omega/K$ )	$(T/R) \cdot$ ( $dR/dT$ )
4.2	277.32	-32.209	-0.49	574.20	-97.344	-0.71	3507.2	-1120.8	-1.34
10	187.11	-8.063	-0.43	331.67	-19.042	-0.57	1313.5	-128.58	-0.98
20	138.79	-3.057	-0.44	225.19	-6.258	-0.56	692.81	-30.871	-0.89
30	115.38	-1.819	-0.47	179.12	-3.453	-0.58	482.88	-14.373	-0.89
77.35	70.837	-0.510	-0.56	101.16	-0.820	-0.63	205.67	-2.412	-0.91
300	30.392	-0.065	-0.65	41.420	-0.088	-0.64	59.467	-0.173	-0.87
400 (HT)	—	—	—	34.779	-0.050	-0.57	46.782	-0.093	-0.79
420 (HT)	—	—	—	33.839	-0.045	-0.55	45.030	-0.089	-0.77

Table A.III.4: Resistance values for three type of Cernox sensors. CX-1050, on the right, is used in the Cryolab experiment. Data in the column of the resistance of sensor CX-1050 are shown in Fig.5.15.

	Lower bound	Nominal value	Upper bound		Var - lower	Var - upper		Perc - lower	Perc - upper
	-37% in P	0%	+37% in P		$\Delta T(\text{var}) - \Delta T(\text{nom}) / \Delta T(\text{nom})$			$T(\text{var}) - T(\text{nom}) / T(\text{nom})$	
Point 1	1.9009	1.9014	1.9020		0.0%	0.0%		55.6%	42.9%
Point 4	1.9207	1.9327	1.9444		0.6%	0.6%		58.0%	35.8%
Point 9	1.9581	1.9907	2.0221		1.7%	1.6%		56.1%	34.6%
Point 14	1.9923	2.0429	2.0911		2.5%	2.4%		54.8%	33.7%
Point 17	1.9908	2.0407	2.0882		2.5%	2.3%		55.0%	33.8%

Table A.III.5: Analysis on the uncertainty on the input power for the lowest heating input, 17 mW. The three columns on the left report the temperature values for 11 (lower bound), 17 (nominal value) and 23 mW (upper bound) of total input power. The variation in the results is obtained dividing by the delta T (the two columns in the centre) and by the absolute value of temperature (last two columns on the right).

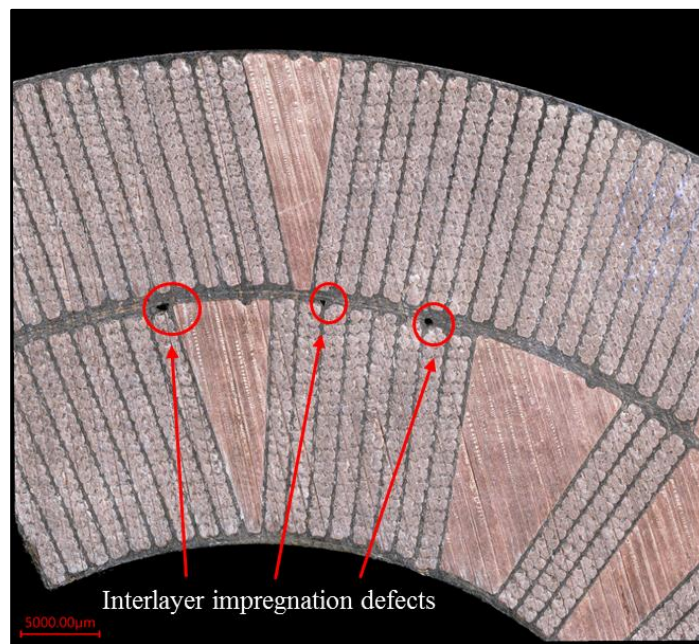


Fig.A.III.1: Micrographs of the coil cross-section. Several defects can be noted, most of them in the interlayer insulation. Credits: reference [45]

COMSOL Model, T = 1.9 K, S2 glass = 0.0 mm													
Imag (A)	I/Iss [%]	Bp [T]	Bp below heaters [T]	Tcs [K]	Tcs below heaters [K]	R_qh (Ohms)	I_qh (A)	Tau (ms)	HEATER				Location
									QH delay (ms)	Peak Pd (W/cm2)	Dep. Eng. Den. (J/cm2)		
1000	6.92	1.04	0.49	15.4	15.8	7.50	84	52.88	231.85	42.6	1.13	tum36	
4000	27.68	3.13	1.47	13.3	14.8	6.50	79	45.83	134.05	37.7	0.86	tum 36	
6000	41.52	6.23	2.93	11.8	14.1	6.50	70	45.83	145.61	29.6	0.68	tum 36	
8000	55.36	7.22	3.39	10.1	13.5	6.50	63	45.83	107.37	24.0	0.55	tum 36	
10000	69.20	9.13	4.29	8.2	12.8	6.50	58	45.8	96.0	20.3	0.47	tum 36	
12000	83.04	11.91	5.60	5.9	12.0	6.50	50	45.8	96.0	15.1	0.35	tum 36	

Table A.III.6: Operating conditions in the outer layer quench heater tests tests. Current and Field below heaters are highlighted.

Assuming all heater energy goes to the tum in direct thermal contact				HEATER Model (1-D)			
COIL				Volumetric - Source			
Peak Power (W/m)	Peak Power (W/cm3)	Energy (J/m)	Energy (mJ/cm3)	Peak P [W]	Peak P [W/m3]	Max. T (Point 15) Below	Time after heat injection [s]
618	29	16	756	5.29E+04	1.704E+10	14.8	0.09
546	25	13	580	4.06E+04	1.508E+10	13.8	0.08
429	20	10	455	3.19E+04	1.184E+10	13.0	0.07
348	16	8	369	2.58E+04	9.587E+09	12.3	0.07
295	14	7	312	2.19E+04	8.126E+09	11.7	0.07
219	10	5	232	1.63E+04	6.039E+09	10.8	0.06

Table A.III.7: Input power density in the quench heaters and results of the HEATER simulation, signed in the column "Max T (Point 15)".

## Bibliography

- [1] Convention for the Establishment of a European Organization for Nuclear Research, Paris, 1st July, 1953.
- [2] Synchro-cyclotron, [https://cds.cern.ch/record/1479590/files/1955\\_E\\_p27.pdf](https://cds.cern.ch/record/1479590/files/1955_E_p27.pdf)
- [3] Herr, W.; Muratori, B.: Concept of luminosity. In Brandt, D. CERN Accelerator School: Intermediate Course on Accelerator Physics, Zeuthen, Germany, 15-26 Sep 2003. CERN. pp. 361–378, 2006.
- [4] Heike Kamerlingh Onnes, Investigations into the properties of substances at low temperatures, which have led, amongst other things, to the preparation of liquid helium, Nobel lecture, December 11, 1913.
- [5] Prof. Marco Breschi and Prof. Antonio Morandi, Lessons of the course “Engineering of superconducting systems”, University of Bologna, Academic year 2017-2018.
- [6] Francesco Grilli, Karlsruhe Institute of Technology.
- [7] P.P. Granieri et al, Stability Analysis of the LHC cables for Transient Heat Depositions, IEEE Transactions on Applied Superconductivity, Vol. 18, No.2, June 2008.
- [8] J.G. Weisend, Handbook of cryogenic engineering, 1998.
- [9] S.W. Van Sciver, Helium Cryogenics, cap.5.3, 1996.
- [10] P.J. Giarratano, W.G. Steward, Transient Forced Convection Heat Transfer to Helium during a step in heat flux, Transactions of the ASME, Journal of Heat transfer, Vol.105, pp. 350-357, 1983.
- [11] W.B. Bloem, Transient heat transfer to a forced flow of supercritical helium at 4.2 K, Cryogenics, Vol.26, May 1986.
- [12] C. Schmidt, Review of steady state and transient heat transfer in pool boiling Helium I, Saclay, France: International Institute of Refrigeration: Commission A1/2-Saclay, pp. 17-31, 1981.
- [13] O. Tsukamoto, S. Kobayashi, Transient heat transfer characteristics of liquid helium, Journal of Applied physics, Vol.46, No.3, pp.1359-1364, March 1975.
- [14] M. Breschi et al, Minimum quench energy and early quench development in NbTi superconducting strands, IEEE transactions on applied superconductivity, vol. 17, no. 2, June 2007.
- [15] L. Dresner, Stability of superconductors, New York, Plenum Press, 1995.
- [16] P.J. Giarratano, V.D. Arp, R.V. Smith, Forced convection heat transfer to supercritical helium, Cryogenics, pp. 385-393, October 1971.
- [17] L. Bottura, M. Calvi, A. Siemko, Stability analysis of the LHC cables, Cryogenics, Vol.26, pp. 481-493, 2006.
- [18] J.G. Weisend, Handbook of cryogenic engineering, page 463, 1998.
- [19] C. Schmidt, Transient heat transfer into a closed small volume of liquid or supercritical helium, Cryogenics, Vol.28, September 1988.
- [20] C. Schmidt, Transient heat transfer to liquid helium and temperature measurement with a response time in the microsecond region, Applied Physics Letters, Vol.32(12), 1978.

- [21] V.D. Arp, Stability and thermal quenches in forced-cooled superconducting cables, Proceeding of 1980 superconducting MHD magnet design conference, Cambridge, MA, pp.142-145, MIT, 1998.
- [22] B. Baudouy et al., He II heat transfer through superconducting cables electrical insulation, Cryogenics, vol.40, pp. 127-136, 2000.
- [23] Jonas Lantz, Heat Transfer Correlations Between a Heated Surface and Liquid & Superfluid Helium, Ph.D. thesis, Linköpings Universitet, 2017.
- [24] Pierre Bauer, Stability of superconducting strands for accelerator magnets, Ph.D. thesis, 1998.
- [25] Breschi et al, Comparing the thermal stability of NbTi and Nb<sub>3</sub>Sn wires, Superconductor Science and Technology, IOP Publishing, 2009.
- [26] Xabier Sarasola, Stefanie Langeslag, David Smekens, Gijs de Rijk, Inspection of the 2-m long 11T coil #104 – Position of the conductors and quality of the impregnation, Test report, CERN., 2015.
- [27] E. Gmelin et al, Thermal boundary resistance of mechanical contacts between solids at sub-ambient temperatures, IOP Publishing, 1998.
- [28] B. de Sousa, T. Koetting, Measurement report: Thermal conductivity of impregnated Nb<sub>3</sub>Sn coil samples – 11 T Dipole samples, TE Department, CERN, 2017.
- [29] C.M. Pastore and Y.A. Gowayed, A self-consistent fabric geometry model: modification and application of a fabric geometry model to predict the elastic properties of textile composites, JCTRER, Vol.16, No.1, January 1994, pp.32-26.
- [30] Y. Gowayed and J-C. Hwang Thermal conductivity of composite materials made from plain weaves and 3-D weaves, Composites Engineering, Vol.5 No.9, pp.1177-1186, 1995.
- [31] Ali R. Hadesfandiari, On the symmetric character of the thermal conductivity tensor, University at Buffalo, 2013.
- [32] C.C. Wang, On the symmetry of the heat-conduction tensor.
- [33] Ling Shi and Huiling Wang, Investigation on thermal contact resistance by photothermal technique at low temperature, Heat Mass Transfer, 2007.
- [34] S.Izquierdo Bermudez, J.Rysti, S.Tavares, B.del Valle Grande, Cryolab, Thermal characterization of Nb<sub>3</sub>Sn coils, CERN, 16/11/2018.
- [35] COGEBI FIROX® P 63P24A Technical sheet.
- [36] SOLIDS manual, CryoSoft, March 2002.
- [37] Mário David Grosso Xavier et al, Transient heat transfer in superfluid helium cooled Nb<sub>3</sub>Sn superconducting coil samples, submitted for publication, 2018.
- [38] L.Bottura and B.Bordini,  $J_c(B, T, \epsilon)$  parametrization for the ITER Nb<sub>3</sub>Sn production, IEEE transactions on Applied Superconductivity, Vol.19, No.3, June 2009.
- [39] B.Bordini, Reversible  $I_c I_c$  reduction of Nb<sub>3</sub>Sn Rutherford cables subjected to transverse pressure: Impact on the performance of the HL-LHC 11 T dipole, 6/02/2019.
- [40] HEATER manual, CryoSoft, 2016.

- [41] A. Devred, Private Communication.
- [42] S. Russenschuck, ROXIE Software, CERN.
- [43] G. Willering et *al*, MBHSP106 DC-loss measurements, 20/03/2018.
- [44] Building 927 and SM-18 facility at CERN, private communications with technicians.
- [45] S. Sgobba, I. Aviles Santillana, E. Muskalsza, TE-MME-MM Section, CERN.
- [46] Synchro-cyclotron explanation video, guided tour, CERN.
- [47] M. D. Grosso Xavier, Private communication.
- [48] S. Izquierdo Bermudez, Private communication
- [49] A. Ballarino, Private communication